54
10-4-91 JS (2)

MANIFESTATIONS OF THE MHD AND KINETIC DYNAMO THROUGH SOFT X-RAYS

George Athanasios Chartas

DOE/ER/53198-181 August 1991

NOTICE

This report was prepared as an account of work sponsored by an agency of the United States Government. Neither the United States nor any agency thereof, nor any of their employees, makes any warranty, expressed or implied, or assumes any legal liability or responsibility for any third party's use or the results of such use of any information, apparatus, product or process disclosed in this report, or represents that its use by such third party would not infringe privately owned rights.

Printed in the United States of America
Available from
National Technical Information Service
U.S. Department of Commerce
5285 Port Royal Road
Springfield, VA 22161

NTIS Price codes
Printed copy: A07
Microfiche copy: A01

DOE/ER/53198--181

DE92 000162

MANIFESTATIONS OF THE MHD AND KINETIC DYNAMO THROUGH SOFT X-RAYS

by

GEORGE ATHANASIOS CHARTAS

A thesis submitted in partial fulfillment of the requirements for the degree of

Doctor of Philosophy
(Physics)

at the
UNIVERSITY OF WISCONSIN-MADISON
1991

MASTER

DISTRIBUTION OF THIS DOCUMENT IS UNLIMITED

MANIFESTATIONS OF THE MHD AND KINETIC DYNAMO THROUGH SOFT X-RAYS

George Athanasios Chartas
Under the supervision of Assistant Professor Samuel Hokin
at the University of Wisconsin-Madison

ABSTRACT

The underlying mechanisms that produce and sustain the reversed toroidal field in RFP's are investigated by analyzing 2D x-ray emissivity reconstructions and by correlating the evolution of the hot electron properties to the reversed toroidal magnetic field. Reconnection of emissivity surfaces as seen in soft x-ray (SXR) reconstructions occur near the predicted resonant surfaces of the m=1, n=-5,-6,-7 resistive tearing modes. Two distinct rates of reversed magnetic field generation are observed. First, in the MHD relaxation phase a sudden increase in $B_t(a)$ is detected. This event coincides with a large increase in the edge hot electron current density. The second mode of flux generation is observed to have a slower rate and occurs during the diffusion phase. A variation of the edge hot electron current density by a factor of four produced only a small change in the measured $B_t(a)$, implying that the contribution of the hot electrons to the dynamo during the diffusion phase is small. $\tilde{T}_{e,hot}/\langle T_{e,hot}\rangle$ was measured to be approximately 60%, which is much larger than the corresponding quantity for the bulk component which is about 30%. Scaling of the magnetic Reynolds number with the diffusion and MHD relaxation

time, τ_{MHD} indicated that the τ_{MHD} does not have a strong dependence on the Spitzer resistivity whereas the diffusion time does depend on the classical resistivity. SXR emission mode analysis during the transition from a rotating to a locked plasma shows a decrease in the m=1 Fourier Bessel component of the emissivity. This is due to the flattening of the emissivity profile as seen in the SXR reconstructions. Finally, mode analysis of reconstructed emissivity profiles reveals the radial location of a localized disturbance, propagating in the ion diamagnetic drift direction , located close to the m=1 rational surfaces.

Samuel C Hokin

Acknowledgements

It was about six years ago when I received a letter of acceptance to enter the Graduate School at the University of Wisconsin-Madison. At the time I was to be found on the isle Samos, one of Greece's historic islands, admiring the temples of Hera and the serenity of the blue sea. One of the first challenges that I came across upon arrival in the US was to accept and familiarize myself with the educational program of the U.W. I am very grateful to Prof. Bernice Durand and Prof. Blanchard for supporting me during those first days. I was very fortunate in joining the plasma physics group during the initialization of a new project; the construction of the MST reversed field pinch. I am very grateful to my graduate thesis advisor Prof. Samuel Hokin for providing me with the freedom of selecting a thesis topic of my choice. I am thankful for his willingness to discuss and provide insight into the controversial issues that I encountered during my research. I would like to thank Prof. Stewart Prager for providing the connections of many of the experimental results to existing theoretical models. Many of the features of the main diagnostics used in this thesis were materialized after lengthy discussions in the plasma physics hallways with Prof. R. Dexter. A fruitful year of learning about x-ray diagnostics occurred during Fancesco Venneri's stay at the MST group as a postdoc. Our plasma physics group is very fortunate in having Roch Kendrick, one of the most talented and creative mechanical engineers on campus. The x-ray calibration experiments (project-X) and the SXR target probe retracting mechanism (smooth operator) bear his signature. If everything else fails in ones circuit design then one could always consult the master mind and chief engineer Tom Lovell. Many fellow graduate students and scientists have provided useful input into this thesis; John Sarff and Bill Ho on the RFP dynamo theory, A. Almagri and S. Assadi on the magnetics, D. J. Denhartog and

Gordon Starr on the Thomson scattering system and Don Holly on the microwave and CO_2 interferometers.

I would also like to add a few words on events that although outside of the plasma physics arena have influenced me during my graduate years in Madison. Some great moments have been written in volleyball history with the "rise" of the Ikarus team organized by Dunkin Chaplin (Doughnuts). This and other athletic activities provided me with the "νους υγιης εν σωματι υγιη"(Socrates). Of course over the long six years there are a few Madisonian figures that have added some weirdness to the whole picture. Catfish (vicious slide guitar), Cosmo (lost in space), Gretchen (Siren in disguise), John Tupa (forgive me for that fish), and Kavoos (fellow comrade) are a few of them. Finally I am thankful to Liz Gaines for supplying those sweet cappuccinos during the long summer nights while I was preparing my thesis.

This work supported by U.S.D.O.E.

Table of Contents

Abstract....ii

Acknowledgements....iv

Table of Contents....vi

1. Introduction....1

References....7

2. The Madison Symmetric Torus Reversed Field Pinch and its Diagnostics....8

2.1 The Madison Symmetric Torus....8

2.2 MST Diagnostics....9

References....12

3. X-Ray Imaging on the MST Reversed Field Pinch....13

3.1 Surface Barrier Detectors....17

3.2 Collimation....18

3.3 Filters....21

3.4 Calibration of the SXR Tomography System....23

3.5 Spectral Emission of Plasmas in the Soft X-Ray Region....27

3.6 Plasma Emissivity....34

3.7 The Maximum Entropy Method....35

References....41

4. The Soft X-Ray Target Probe....43

4.1 Description of the SXR Target probe....44

4.2 Analysis of Soft X-Ray Target Data....45

References....51

5. A Review of RFP Dynamo Theory....53

5.1 Resistive Tearing Modes....53

5.2 The MHD Dynamo....54

5.3 Review of Results Obtained from Numerical Simulations of Magnetic Reconnection in RFP's....59

5.4 The Kinetic Dynamo....62

References....65

6. Manifestations of the MHD Dynamo through Soft X-Rays....67

6.1 Measurement of the Poloidal m and Toroidal n Numbers of Tearing Modes on MST....72

6.2 Mode Analysis of Soft X-Ray Emissivity....77

6.3 Generation of Reversed Magnetic Flux During the Diffusion and Relaxation Phase....83

6.4 Emissivity Mode Analysis of Locked Plasmas....89

6.5 Scaling of the Magnetic Reynolds Number with the MHD Relaxation and Diffusion Time of a Sawtooth Event....93

References....102

7. Manifestations of the Kinetic Dynamo through Soft X-rays....105

7.1 Properties of the Edge Electrons in MST....107

7.2 Manifestations of the Kinetic Dynamo through Soft X-Ray Measurements....115

7.3 Measuring Fluctuations of the Hot Electron Properties with a Soft X-Ray Target Probe....120

References....123

8. Conclusions and Discussion of the Experimental Results....124

References....130

Appendix I....132

Chapter 1

Introduction

The reversed field pinch (RFP) magnetic topology has given rise to a new set of physical phenomena. The main feature of the RFP that distinguishes it from the tokamak is the reduced externally imposed toroidal magnetic field. From the standpoint of considering the RFP as a future fusion device the low toroidal field leads to relatively high values of β (the ratio of the plasma thermal pressure to the magnetic pressure). The advantages of operating in a high β regime include a high fusion power to loss ratio, minimization of stresses on the magnetic coils and a decrease in the cyclotron radiation losses. In addition, the magnetic shear of the magnetic field provides stability against pressure-driven modes. From a purely physics viewpoint the RFP renders the opportunity of studying many new phenomena arising from the nonlinear interaction of various resistive magnetohydrodynamics (MHD) modes. The history of the pinch began with the experiments of Bennet[1] in 1934 when he observed the contraction of a current channel caused by its self-produced magnetic field.

Measurements of the plasma pressure and magnetic pressure in present day RFP's reveal a relatively high beta. This is attributed to the large gradients in the pitch of the magnetic field lines (shear). The condition for stability against pressure driven modes considering toroidal effects is given by the Mercier criterion[2-4],

$$\frac{dp}{dr}\left(1-q^2\right)+\frac{rB_\varphi^2}{32\pi}\left[\frac{1}{q}\frac{dq}{dr}\right]^2 \geq 0 \qquad (1.1)$$

where p is the plasma pressure and q is the safety factor defined as :

$$q = \frac{r\,B_\varphi}{R\,B_\theta}. \qquad (1.2)$$

Since the shear of the magnetic field lines is large in RFP's, eq. (1.1) is satisfied and pressure driven instabilities are not as severe as current driven modes in present-day RFP's. The ideal stability analysis as developed by Newcomb[5] and Robinson[6] show that RFP's are susceptible to current driven instabilities. The analysis involves the calculation of an energy integral $W(\xi)$. An instability arises whenever a trial function ξ (radial displacement) makes the energy integral negative. The radial locations r_s for which the radial displacement is large is given by the equation:

$$q\,(r_s) = \frac{m}{n}, \qquad (1.3)$$

where m and n are the poloidal and toroidal mode numbers respectively. The surfaces that correspond to these unstable modes are called resonant surfaces. A comparison of q profiles for a tokamak and an RFP is given in figure 1.1. The existence of several resonant surfaces in the RFP plays an important role in preventing various unstable modes from growing too large. The nonlinear interaction of these neighboring modes turns out to have a stabilizing effect.

An interesting phenomenon in RFP's first observed in ZETA[7] is the reduction of the magnetic fluctuation level during the reversed-field sustainment period. One explanation comes from Taylor's relaxation theory[8] in which the plasma seeks a minimum energy state. This is thought to be achieved through the nonlinear interaction of resistive tearing modes. In real laboratory plasmas the fully relaxed states are not maintained due to resistive diffusion. The magnetic profiles for the

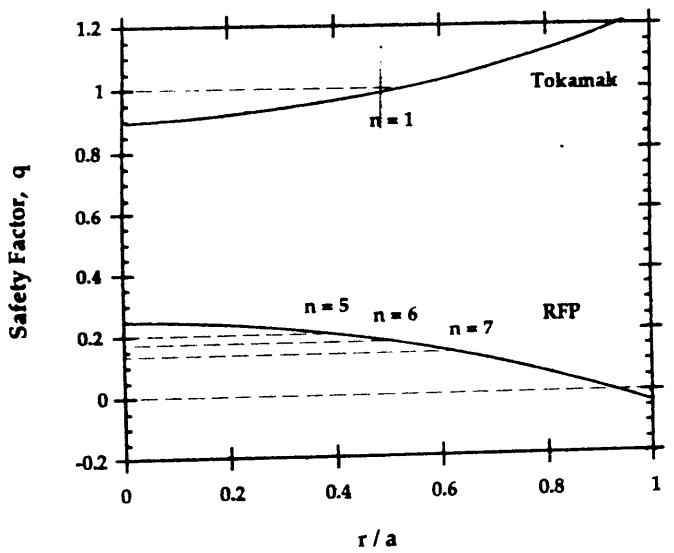

Figure 1.1. *Comparison of the q profiles between a tokamak and a RFP.*

minimum energy state are obtained by minimizing the magnetic energy, $W = \int \frac{B^2}{8\pi} dV$, with the constraint that the magnetic helicity $K = \int_{\text{over plasma volume}} \vec{A} \cdot \vec{B}\, dV$ is invariant. The resulting equation is,(for β=0) :

$$\vec{\nabla} \times \vec{B} = \mu \vec{B} \tag{2.4}$$

The solution of this equation in a cylinder is:

$$B_\varphi(r) = B_\varphi J_0(\mu r), \quad B_\theta(r) = B_\theta J_1(\mu r) \tag{2.5}$$

where $J_0(\mu r)$ and $J_1(\mu r)$ are the zero and first-order Bessel functions.

It is a common observation in all present day RFP's that the reversed toroidal field does not diffuse away at the rate given by $\frac{\partial \vec{B}}{\partial t} = \frac{\eta}{\mu_0} \nabla^2 \vec{B}$, but is sustained for a much longer period of time. Experimental results indicate that a dynamo process is necessary to maintain the reverse toroidal field. The objective of this thesis is to investigate the underlying mechanisms that produce the reversed field in RFP's and determine the contribution of each under various plasma conditions. Experimental and theoretical results have suggested the following RFP dynamo mechanisms.

a) Turbulent MHD dynamo.

A magnetofluid with a homogeneous, isotropic and non - mirror symmetric velocity field can generate a mean magnetic field. This process of creating a large scale structure from small scale turbulent motions is referred to as an inverse cascade. The direct measurement of the contribution of the turbulent MHD dynamo in generating the reversed field is very difficult since it requires a diagnostic of extremely good spatial and time resolution and of a non plasma perturbing nature. The present soft x-ray (SXR) imaging systems on RFP's do not have the necessary spatial resolution although they do satisfy the non intrusive condition.

b) A coherent MHD dynamo .

By coherent we imply that only a few modes are responsible for the observed magnetic flux generation. A variety of experimental and 3D MHD simulation results fall in this category. There is rigorous debate over which modes drive the dynamo. I will address this question by providing measurements of the mode amplitudes of the soft x-ray (SXR) emissivity and by scaling the magnetic Reynolds number with the diffusion and MHD relaxation time.

c) Kinetic dynamo model.

In this model the reversed toroidal field is produced by electrons that wander across stochastic field lines and eventually find themselves moving opposite to the externally applied electric field. The origin of the stochasticity is thought to be due to MHD microturbulence. Measurements of the current density of the hot electrons vs the amplitude of the reversed toroidal field at the wall and the variation of the ratio between hot electron temperature and the bulk temperature will be presented.

One of the difficulties in this research has been the diversity of results announced from various RFP laboratories. The cause of this diversity possibly lies in differences in aspect ratios, magnetic field errors and plasma wall interactions. MHD simulations predict that the dominant unstable modes in RFP's are current-driven and have a poloidal mode number of m = 1 and toroidal mode numbers approximately twice the aspect ratio. For RFP's with large aspect ratios, (ie. ZT-40M has an aspect ratio of 5.7), the helical modes are spaced close together. As these unstable modes begin to grow, they eventually overlap and saturate due to the stabilizing effect of their nonlinear interactions. Since the spacing of the resonant surfaces is small the modes saturate before they reach large amplitudes. In MST however, the unstable modes can reach larger amplitudes since it has an aspect ratio of 2.9. This has been observed experimentally through the presence of large oscillations of the SXR signals at a wide range of q values.

The measurement of the properties of the edge hot electrons in RFP's with the use of movable probes has been extremely difficult. Most of the insertable sensors have to be heavily shielded with high temperature and thermal shock resistant materials which unfortunately result in larger perturbations of the plasma. The use of non intrusive diagnostics such as SXR imaging systems provide useful information on magnetohydrodynamic motions in a variety of discharges. The spatial resolution of these tomographic systems in some RFP's is often poor due to limited access around the torus. ZT-40M[9] and HBTX1C[10] did not have enough surface barrier diodes (SBD) chords to implement tomography, while the Repute-1[11] RFP has only two chord arrays with a total of 18 SBD detectors. The SXR emissivity in Repute-1 is determined by applying a Cormack based algorithm. Comparison of a maximum entropy and the more conventional Cormack reconstruction method for snake discharges on JET[12] show that the Cormack method may produce artifacts (such as hollow profiles) for large off axis structures. Results from the high resolution x-ray tomography system on the Tokamak de Varennes[13] show that the use of low harmonic reconstructions may also lead to erroneous emissivity reconstructions. The MST's unique toroidal field system (the toroidal shell serves as the toroidal field windings) allows easy access for many diagnostics. The two main diagnostics, on which most of the measurements for this thesis were made, are the SXR imaging system (4 chord array of 32 SBD's) and an SXR target probe. The first was implemented to study the MHD dynamo process and the latter to measure the properties of the edge fast electrons.

This thesis has been organized in eight chapters. In chapter 2 a brief description is made of the MST and its diagnostics. The SXR imaging system and the SXR target probe are described in chapter 3 and 4 respectively. A review of the RFP dynamo theory is given in chapter 5. Experimental results related to the manifestation of the MHD dynamo through soft x-rays are presented in chapter 6. Data from measurements of the fast electron properties are presented in chapter 7. Finally chapter 8 is devoted to the conclusions and discussion of the experimental results.

References for chapter 1.

1. H. W. Bennet, Phys. Rev. 43 (1934) 890.

2. C. Mercier, Nucl. Fusion 1 (1960) 47.

3. A. D. Baker, W. L. Mann, , in Pulsed High Beta Plasmas (Proc. 2nd Top Conf. Garching, 1972) Rep. IPP 1/127 (1972) B7.

4. A. Haberstich, A. D. Baker, N. J. Di Marco, W. L. Mann, S. Ortolani, in Pulsed High Beta Plasmas (Proc. 3rd Top Conf. Abingdon, 1975) Pergamon Press, London (1976) 249.

5. A. W. Newcomb, Ann Phys. (N.Y) 10 (1960) 232.

6. C. D. Robinson, Plasma Phys. 13 (1971) 439.

7. P. E. Butt, R. Carruthers, D. T. J. Mitchell, R. S. Pease, C. P. Thonemann, et al. , in Peaceful Uses of Atomic Energy. (proc. 2nd Int Conf. UN. , Geneva, 1958) Vol 32 (1958) 42.

8. J. B. Taylor, Reviews of Modern Physics, Vol. 58 No. 3 July (1986).

9. G. A. Wurden," *Soft x-ray results on ZT-40M reversed-field pinch.*" Phys. Fluids 27 (3), March (1984).

10. M. Malacarne and I. H. Hutchinson " *Soft X-ray Imaging Diagnostic on HBTX-1A Reversed Field Pinch*" UKAEA Report, CLM-R 227 Culham Laboratory (1982).

11. N. Asakura, Y. Nacayama, S. Shinohara, H. Toyama, K. Miyamoto, Nuclear Fusion, Vol. 29, No 6 (198[illegible]).

12. L. M. Blush and G. A. Navratil, "*Maximum Entropy Tomographic Reconstruction of JET Soft X-Ray Emission* ", Presented at the APS meeting, Division of Plasma Physics, Anaheim, CA, Nov. (1989).

13. C. Janicki, R. Decoste, and C. Simm, Phys. Rev. Lett. 62, 3038 (1989).

Chapter 2

The Madison Symmetric Torus Reversed Field Pinch and its Diagnostics.

2.1 The Madison Symmetric Torus (MST).

MST is a toroidal magnetic confinement device that has been designed primarily as a reversed field pinch but will have in addition the capability of running in a tokamak mode. The MST incorporates many unique features that aim to minimize the magnetic field errors, allow efficient machine disassembly and facilitate good diagnostic access. A brief description of the unique engineering aspects of MST relevant to this thesis will be presented. This will later on give us some insight on why some of MST's plasma properties differ in some respects from those of other RFP's. A thorough description of the design features of the MST is given in ref. 1.

The MST aluminum vacuum vessel has a minor radius of .52 m and a major radius of 1.5 m, giving it an aspect ratio of about 2.9. In order to allow easy access and minimize the magnetic field ripple the toroidal field is produced by driving current through the aluminum shell. The magnetic fields enter the vessel through poloidal and toroidal gaps. The radial magnetic field is minimized at the poloidal gap with the use of the continuity windings and poloidal field windings, shown in figure 2.1 . The continuity windings allow the image current in the shell to flow around the transformer core from one side of the poloidal gap to the other. The poloidal field windings produce the toroidal voltage and are distributed in the poloidal flange in such a manner that they create a minimum gap field error. The

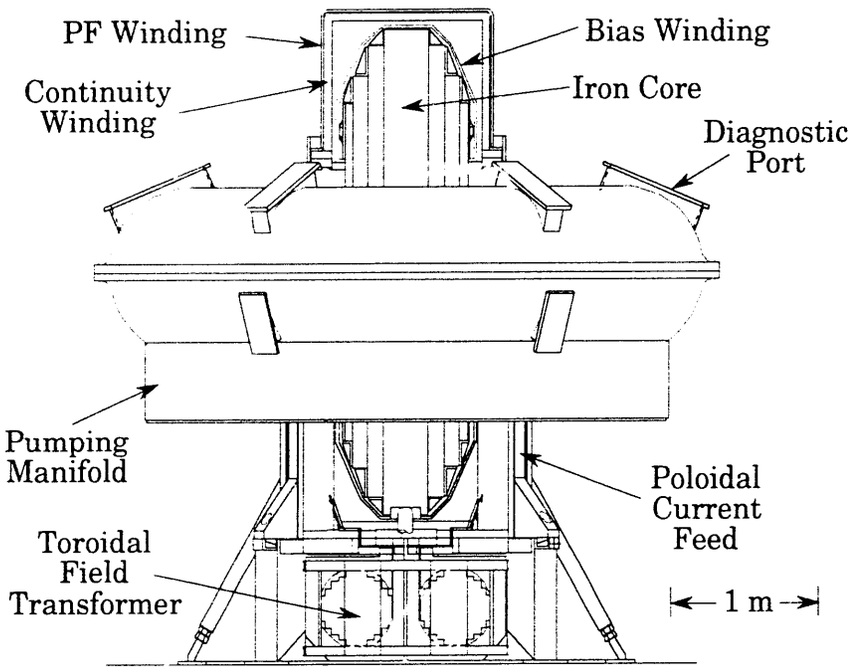

Figure 2.1 *The Madison Symmetric Torus.*

employment of further correction schemes[2] allows the field errors to be reduced considerably. This resulted in discharges of improved confinement, and longer duration. The up-to-date achieved plasma parameters in MST are listed in table I.

2.2 MST Diagnostics

The two main diagnostics used for obtaining most of the data presented in this thesis are the SXR imaging system and the SXR target probe, both described in detail in chapters 3 and 4 respectively. Comparison of data obtained from the SXR

Achieved Parameters for MST.	
PARAMETER	Achieved
Plasma Current (MA)	0.2 - 0.65
Loop Voltage (Volts)	~ 10 - 20
β_p	5 to 15 %
Line Averaged Density (cm^{-3})	$0.5 - 3. \times 10^{+13}$
Central Electron Temperature (eV)	~ 100 - 500
Ion Temperature (eV)	~ 100 - 500
Energy Confinement Time (msec)	≤ 1.5
Plasma Duration (msec)	30 - 80

Table I. *Plasma parameters achieved in MST.*

detectors with that of other diagnostics proved to be very useful. A set of 64 fixed magnetic pick-up coil triplets distributed toroidally and poloidally around the MST provided information on the magnetic field at the wall. Correlating in time the toroidal field at the wall with SXR emissivity reconstructions revealed useful information on the MHD dynamo. Movable magnetic probes provided the edge current density and magnetic field.

The SXR target data are also compared to those of the electrostatic energy analyzer (EEA) which is similar in design to the one used on ZT-40M[3] and was operated by Matt Stoneking. Temperature and density measurements were necessary for calculating the magnetic Reynolds number. The central electron temperature

was measured with a Thomson scattering system[4] which was operated at the time by Daniel Den Hartog and Gordon Starr . The main components of the system are a 10 Joule Q-switched ruby laser and a Cross-Czerny-Turner spectrometer coupled to a multichannel plate. The system also gave the central density for a single point in time. The chord-averaged density was measured with a two colour laser interferometer[5].The main laser is a CO_2 laser of wavelength 10.6 μm while a HeNe laser at 3.39 μm is used for vibration compensation. Impurity signals were monitored with a Jarrell-Ash monochrometer (visible wavelengths) and phototubes with interference filters. The SXR plasma spectra above 1 keV and the SXR source calibration unit spectrum were obtained from a Si(Li) detector system run by Samuel Hokin.

References for chapter 2.

1. R. N. Dexter, D. W. Kerst, T. W. Lovell, S. C. Prager and J. C. Sprott. " *The Madison Symmetric Torus* ." Fusion Technology Vol. 19 Jan. (1991).

2. A. F. Almagri , " *The Effects of Magnetic Field Errors on Reversed Field Pinch Plasma.*" Ph.d Thesis , University of Wisconsin-Madison (1990) .

3. J. C. Ingraham, R. F. Ellis, J. N. Downing, C. P. Munson, P. G. Weber and G. A. Wurden. " *Energetic Electron Measurements in the edge of a reversed field pinch* ." Phys. Fluids B2 (1) Jan. (1990).

4. D. J. Den Hartog *"An Energy Confinement Study of the MST Reversed Field Pinch using a Thomson Scattering Diagnostic.*", Ph.D Thesis, University of Wisconsin-Madison (1989).

5. P. Innocente and S. Martini, Rev. Sci. Instruments 59 (8) August (1988).

Chapter 3

X-Ray Imaging on the MST Reversed Field Pinch.

Introduction

The measurement of the evolution of the emissivity (power emitted per unit volume in the soft x-ray region) in an RFP plasma can provide valuable information on the new physics that arises in these devices. The emissivity surfaces can be regarded, to a good approximation, as flux surfaces. This can be seen from the following argument. The emissivity I_{sxr} can be expressed as a function of electron density n_e, ion density n_i, impurity density n_α, the charge state Z_α and the electron temperature T_e.

$$I_{sxr} = F\,(T_e\,,\,n_e\,,\,n_i\,,\,n_\alpha\,,Z_\alpha) \qquad (3.1)$$

In magnetically confined plasmas the parallel thermal and charge particle diffusivity is much greater than the perpendicular diffusivity. As a result we expect T_e, n_e, n_i, n_α, Z_α to be approximately constant on a magnetic flux surface and so the emissivity I_{sxr} is only a function of the flux coordinate Φ. An additional criterion for good correspondence of SXR and flux contours is that the target x-rays produced by superthermal and runaway electrons striking the walls do not contribute significantly to the SBD signals.

The changes of the shape and position of these surfaces with time can indicate the growth rates and poloidal and radial structure of instabilities that appear during a RFP discharge. Poloidal rotation of tearing modes can be observed during the diffusion phase. Large profile perturbations are also seen whenever the plasma

magnetic energy moves towards the minimum energy state (also known as the MHD relaxation phase). The phase locking of tearing modes of different helicities which produce a localized disturbance often referred to as a slinky can also be observed from x-ray imaging.

SXR TOMOGRAPHY ON MST.

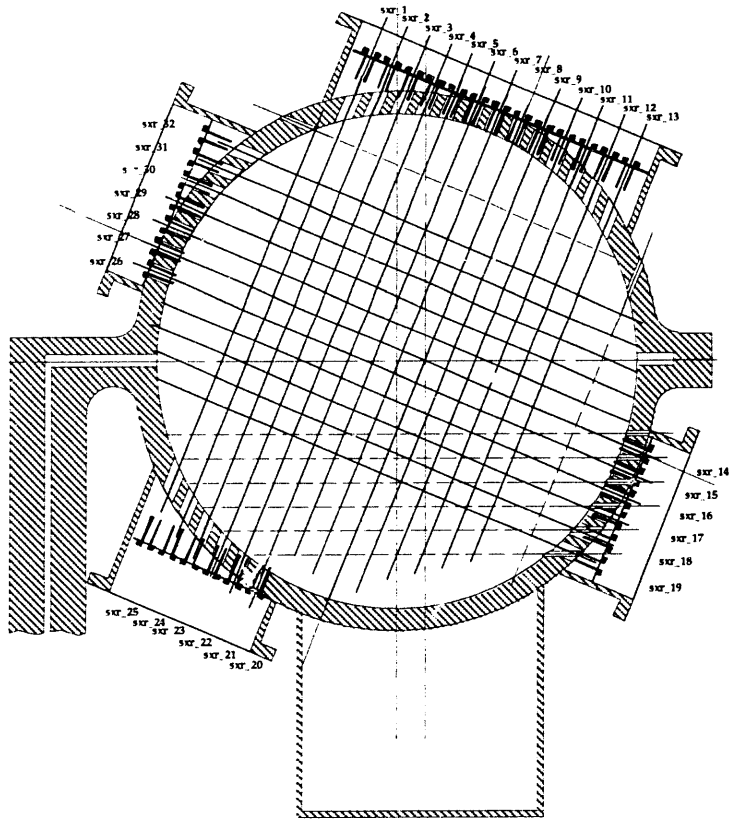

Figure 3.1. *The soft x-ray system on MST features a 40 SBD chord array, Be filters of thickness .3 mils and black anodized collimators.*

The imaging system developed on the MST includes a total of 40 SBD detectors,(see figure 3.1) . Each detector is filtered with a 7.6 μm Be filter and collimated in order to measure the radiation from highly ionized impurities which are located mostly near the center of the torus.

Various measurements of ratios of soft x-rays that were filtered with different thickness foils show that the SBD signals are dominated by photons with energies between 500 eV and 1 keV. If there were a large contribution from soft x-rays with energies above 1 keV we would expect the ratios in figure 3.2 to be much closer to unity.

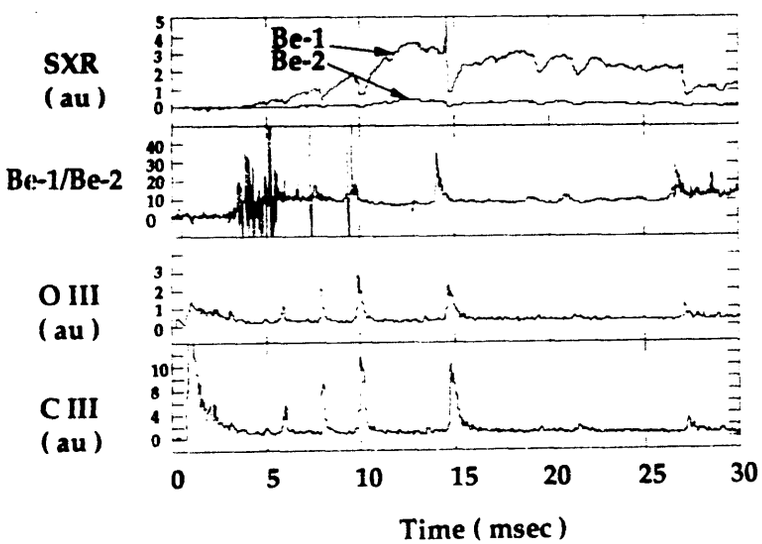

Figure 3.2. *The ratio of two SBD's with filters Be-1 = .3 mils and Be-2= .6mils respectively, is approximately 10 for this disharge. This implies that the impurity line that dominates the SBD signal lies between 500 eV and 1 keV (see fig. 3.3), making oxygen a probable candidate.*

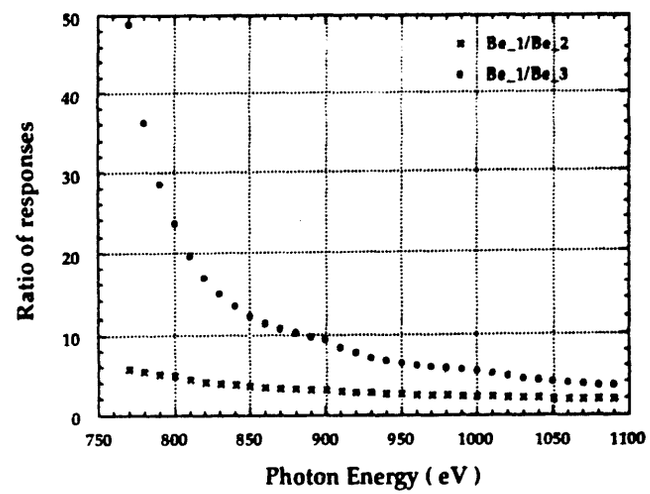

Figure 3.3. *Ratio of the responses for two SBD - filter systems. For signals dominated with impurity lines the ratio of two differently filtered SBD signals is approximately equal to the ratio of their responses at the energy of the line.*

In higher temperature devices with electron temperatures above 1 keV the continuum Bremsstrahlung radiation becomes more important and various filter techniques can be easily employed to measure the electron temperature. Unfortunately, in our case the line-dominated radiation makes it difficult to deduce temperatures from filter methods. The detectors are collimated mainly to improve the spatial resolution of the system. The maximum entropy[1] and Fourier-Bessel[2] methods are used to reconstruct the emissivity profiles. A description of these

methods and a test of their ability to unfold various phantom sources will provide us with an indication of their limitations and possible artifacts that they may produce under certain conditions.

3.1 Surface Barrier Detectors

Since the heart of the MST tomography system is the surface barrier detector array that samples portions of the emitted soft x-ray radiation ,we will begin with a brief description of its properties.

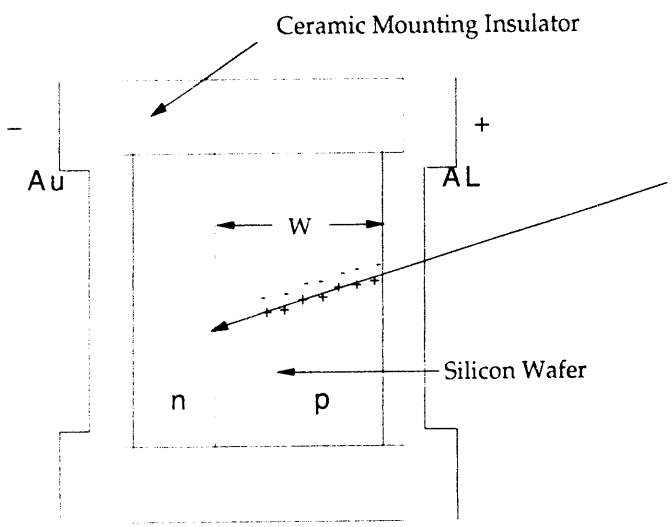

Figure 3.4. *The surface barrier detector. Every electron hole pair that is created in the depiction layer corresponds to a loss of 3.6 eV of energy from the particle that entered the semiconductor detector.*

SBD's are more commonly used for charged particle counting and spectroscopy. However they have become very popular in diagnosing soft x-rays emitted from plasma sources mainly because they are very compact and have a very fast time response. The electrons and holes that are created from an ionizing particle absorbed in the depletion layer of the SBD are collected in a relatively short time of a few nanoseconds. Every electron-hole pair that is created corresponds to a loss of 3.6 eV of energy from the photon that entered the semiconductor detector. This value will also determine the cutoff energy of the detector. Photons with energy less than 3.6 eV will not be detected. A knowledge of the various metallic and semiconductive layers and their thickness is important for calculating the response function of the detectors. The basic components of a typical surface barrier detector can be seen in figure 3.4. The SBD's used for soft x-ray tomography on MST are the cleanable electrode type manufactured by EG&G Ortec (model : BR_017_050_100) and Tennelec (model : CE_050_100_014_cm). For the cleanable electrode type the ring that supports the silicon wafer is reversed so that the Al non-rectifying contact is in front and the thin gold film in the back. The thickness of the various layers are:

- Al non-rectifying contact=1.8×10^{-5} cm
- Si p-type depletion layer : $W = 0.5\,(P_p\,V_b)^{1/2}\ \mu m = 2.2\times10^{-2}$ cm

where, P_p is the p-type resistivity in ohm-cm and V_b = 15 Volts is the applied bias voltage.

3.2 Collimation

Each SBD detects radiation emitted from a volume determined by the torus geometry and the collimation used. It is important to sample the plasma volume as uniformly as possible. The volume sampled by each detector must be small enough

so that localized fluctuations can be studied and large enough that the sum of the volumes "seen" by each detector covers the entire plasma volume under consideration. In employing a maximum entropy method to reconstruct emissivity profiles from a set of projection values the emitting volume is divided into a certain number of cells. The size of the cells should be taken to be roughly the spacing of the detectors. We introduce a function that characterizes the contribution of the cell i to detector j. This function W_{ij} is determined solely by the geometry of the cell and detector arrangement.

$$W_{ij} = \frac{1}{4\pi} \int_{V_{cell}} \omega_i(\vec{r})\, dV_{cell} \qquad (3.2)$$

where $\omega_i(r)$ is the solid angle subtended by the active area of the SBD viewed through the collimator at the location r. For a collimator, fig 3.5, of inner radius $\alpha_2/2$, length col and an active SBD area of $\pi\alpha_1^2/4$ the solid angle at point (r,x) is:

$$\omega_r(r,x) = \frac{[\text{area of overlap of circle } \alpha_2 \text{ projected on } \alpha_1]}{x^{-1} \times \left[x^2 + \left[r + \left(\frac{\alpha_1}{2} - L\right)\right]^2\right]^{\frac{3}{2}}}$$

$$\text{where } L = \left(\frac{col}{x - col}\right)\left[\left(\frac{x - col}{col}\right)\left(\frac{\alpha_1 + \alpha_2}{2}\right) + \frac{\alpha_2}{2} - r\right]$$

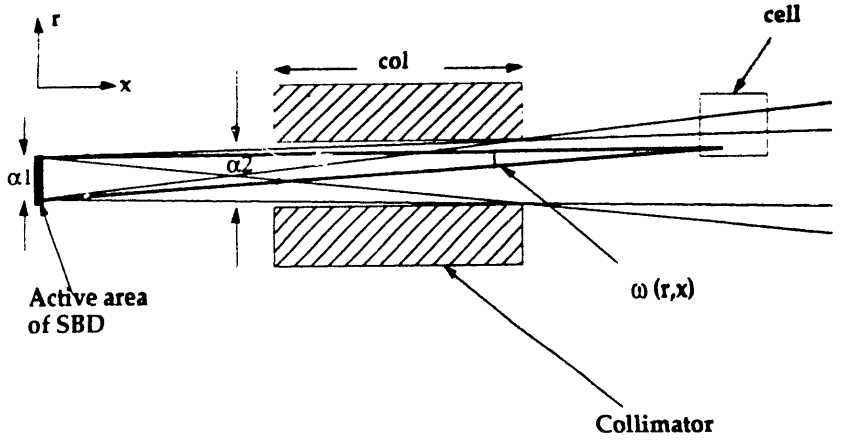

Figure 3.5. *Collimators were used to improve the spatial resolution of the imaging system.*

The area of overlap of two circles (figure 3.6) of radius R_1 and R_2 is:

$$Area(S,R_1,R_2) = \cos^{-1}\left(\frac{L_1}{R_1}\right)R_1^2 + \cos^{-1}\left(\frac{L_2}{R_2}\right)R_2^2 - \left(R_1^2 - L_1^2\right)^{1/2} L_2 - \left(R_2^2 - L_2^2\right)^{1/2} L_1$$

where:

$$L_1 = \frac{L}{2} + \frac{R_1^2 - R_2^2}{2L}$$

$$L_2 = \frac{L}{2} - \frac{R_1^2 - R_2^2}{2L}$$

$$L = R_1 + R_2 - S$$

$$L = L_1 + L_2$$

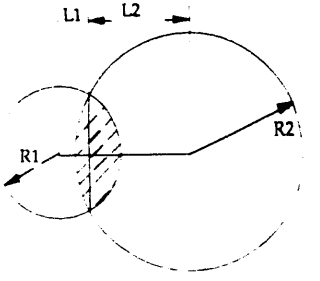

Figure 3.6. *For sources off axis only a portion (shaded area) of the SBD's active area is "illuminated".*

The response function corresponding to each detector can be integrated over each cell to provide the weighting functions. The integration is done using a 3D Gaussian quadratures numerical integration technique. These weighting functions have only to be determined once and may be stored in a file which is read in the initial phase of the maximum entropy method(MEM) reconstruction program (see figure 3.7).

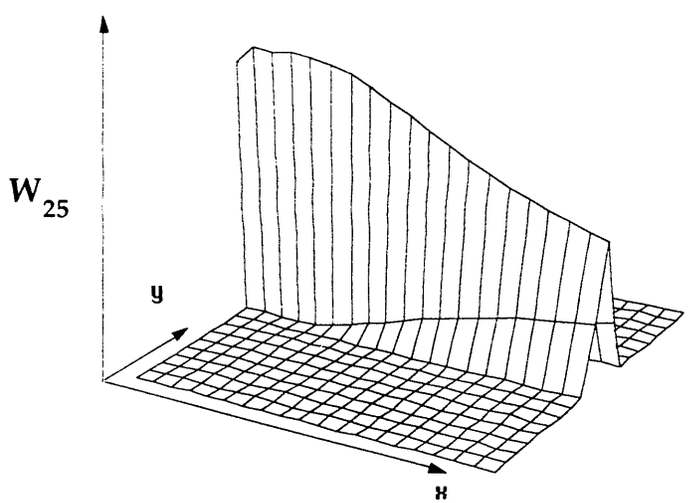

Figure 3.7. *Weighting function of detector number 25.*

3.3 Filters

Beryllium filters with a thickness of 7.6 μm are placed in front of the detectors in order to select a particular energy band of the emitted radiation. The intensity of a beam of monochromatic x-rays that passes through a thin layer of matter is :

$$I(z) = I(0)\, e^{-\mu(E) z} \qquad (3.3)$$

where μ(E) is the attenuation coefficient and z is usually given in grams per cm^2.

We can now write an expression for the response function for the system:

$$R = \frac{\text{Intensity absorbed in depletion layer}}{\text{Incident Intensity}} = \frac{I_3 - I_4}{I_0} \qquad (3.4)$$

$$R(E) = e^{-\mu_{Be} r_{Be} t_{Be}}\, e^{-\mu_{Al} r_{Al} t_{Al}}\, e^{-\mu_d r_d t_d} \left(1 - e^{-\mu_{Si} r_{Si} t_{Si}}\right) \qquad (3.5)$$

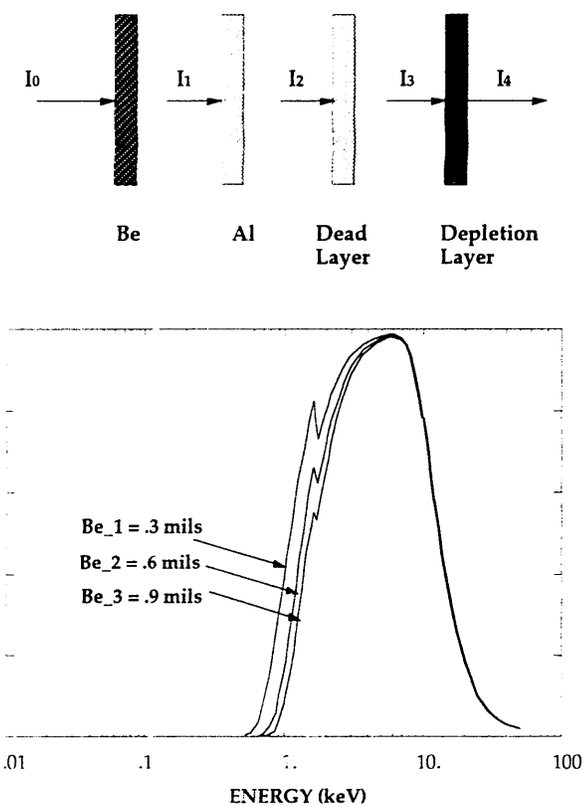

Figure 3.8. *The response curves of the SBD-filter system for various thicknesses of beryllium. The response for .3 mils Be is appoximately 2 % at 600 eV.*

The detected signal can be expressed as :

$$I = K\int_0^{\infty} dE\ S(E)\ R(E) \qquad (3.6)$$

where K depends on the geometry of the system , S(E) is the spectrum of the radiation emitted by the plasma and R(E) is the response function.

3.4 Calibration of the SXR Tomography System

A soft x-ray source was made for the calibration of the SBD's. The main features of the source are :

- Voltage range : 2 kV - 10 kV
- Tungsten anode
- Tungsten filament with Tantalum focusing cup

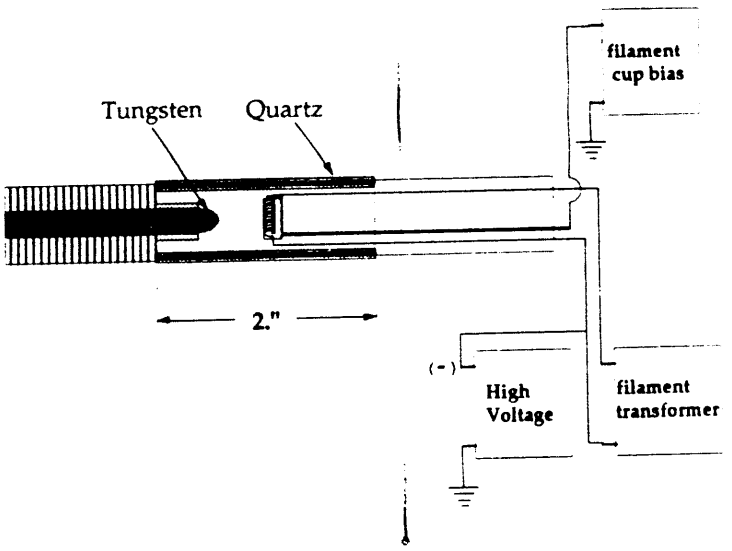

Figure 3.9. *The soft x-ray source used for calibrating the imaging system.*

A reference detector was used to monitor slow variations in the source intensity. We proceede now to obtain a formula for the expected output of a SBD. The spectral intensity produced by an electron of kinetic energy $mu^2/2$ incident on an element of atomic number Z is approximately [3] :

$$I(E) = k_1\, i\, Z\left(\frac{1}{2} m\ u^2 - E\right) + Line\ contributions\ from\ target \qquad (3.7)$$

where i is the emission current of the SXR tube , E is the photon energy and $k_1 = 100\ erg^{-1}\ sr^{-1}$. The voltage measured by the SBD after amplification is then :

$$V_{out} = k_2 G \int_0^{E_{acc}} R(E)\, i\, Z\,(E_{acc} - E)\, dE + Line\ contributions \qquad (3.8)$$

where : G is the gain of the linear amplifier, E_{acc} is the accelerating voltage=$mu^2/2$ and R(E) is the transmission function of the SBD plus filters. The line contribution from the tungsten target was measured to be significant due to the excitation of the 1.77 keV M line of tungsten. The soft x-ray source spectrum was measured using a Si(Li) detector. The measured spectrum is shown in fig. 3.10 .

One of the first properties of the system to be tested was its linearity. The system includes the beryllium filter, the SBD, and the amplification stage. We expect the output voltage to scale linearly with the emission current. The measurements indicate that the system is linear , (figure 3.11a) .

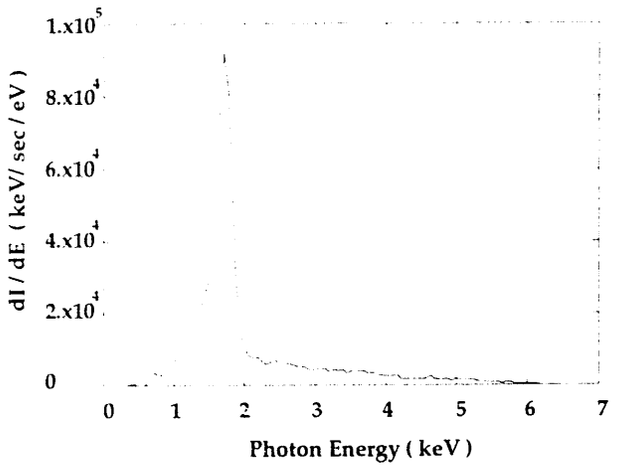

Figure 3.10. *The spectrum of the soft x-ray source used to calibrate the imaging system was measured with a Si(Li) detector. The acceleration voltage was set at 6 kVolts.*

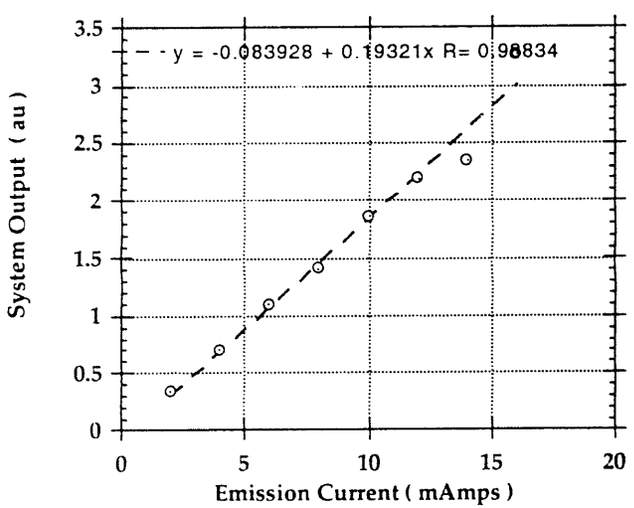

Figure 3.11a. *The linearity of the SBD, filter and amplifier system were examined by measuring the output voltage vs x-ray tube emission current.*

The SXR imaging system on MST w .s recalibrated by scanning the soft x-ray source along a path perpendicular to the SBD line of sight. Two scans were performed , one along the line of sight of detector sxr-7 and the other along the line of sight of detector sxr-14. The SXR source was swept across the entire SBD array in 15 sec in order to minimize any errors from a possible drift of the SXR intensity.The motion of the source was provided by a Slo-Syn stepper motor that was controlled through a programmable 430 PI indexer . The SBD signals were sampled at a rate of 1 kHz on 12 bit DSP 4012 digitizers. The SXR calibration factors are obtained from the relative height of the measured SBD signals (see fig 3.11b).

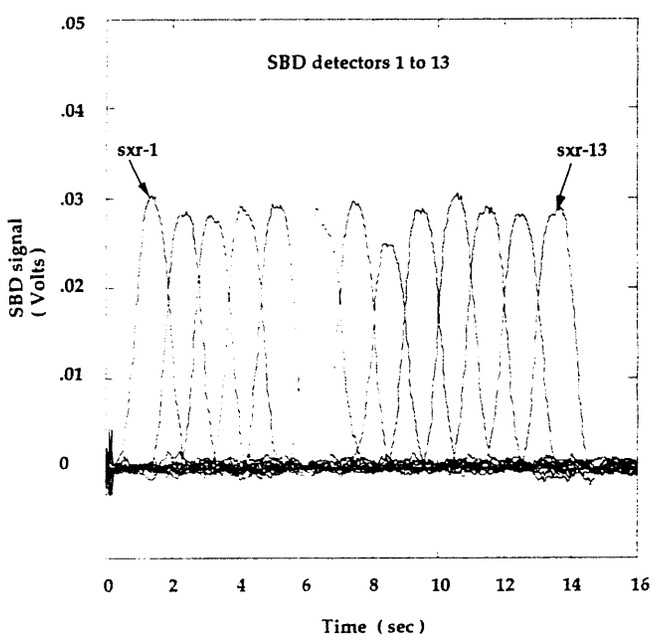

Figure 3.11b. *Measurements from an in* si tu *calibration of the SXR imaging system.*

3.5 Spectral emission of plasmas in the soft x-ray region

For the interpretation of SXR tomographic reconstructions one must first determine the radiative mechanisms that contribute to the measured signals. The spectral emission varies considerably for different magnetic confinement devices since it depends on plasma temperature, density, impurity abundance, superthermal electrons and runaway electrons. Having determined the spectrum, the next step is to derive the response of the measuring diagnostic vs energy. An overview of the spectral emission of plasmas in the soft x-ray regime will provide us with some insight on which radiative mechanisms we expect to dominate the soft x-ray signals measured with SBD 's.

The soft x-ray spectrum emitted by a hot tenuous plasma consists of continuous Bremsstrahlung radiation, recombination radiation and a set of impurity lines.

Continuum free-free radiation.

Free-free radiation, also referred to as Bremsstrahlung, is produced when free electrons are accelerated by Coulomb collisions with ions. Since the amplitude of the radiation is proportional to the charge and acceleration, the radiation from the ions is much smaller. The energy emitted per unit time, volume and frequency due to free-free Coulomb collisions is [4-5]:

$$\frac{dW_{ff}}{dh\nu} = h\nu \sum_s \sum_Z n_e\, n(s,Z) \int_0^\infty d\sigma_{ff}(E_c, h\nu, Z)\, v_e\, f(E_c)\, dE_c \qquad (3.9)$$

where: units (ergs $cm^{-3}\, s^{-1}\, Hz^{-1}$), s is the atomic species of the ion, Z is the charge state of the ion, n_e is the electron density, n(s,Z) is the density of the ions of atomic species s and charge state Z, E_c is the kinetic energy of the electron, $d\sigma_{ff}$ is the free-

free differential cross section and $f(E_c)$ is the electron energy distribution function. If we assume a Maxwellian distribution function for the electrons, the radiated power per unit volume is:

$$\frac{dW_{ff}}{dh\nu} = \frac{6.4 \times 10^{-40}}{T_e^{1/2}} n_e \sum_s \sum_Z Z^2\, n(s,Z)\, \bar{g}_{ff}(\nu, Z, T_e)\, e^{-h\nu/T_e} \qquad (3.10)$$

units (erg $cm^{-3}\, s^{-1}$, eV, cm^{-3}) where $\bar{g}_{ff}$ is the free - free Gaunt factor. By integrating over frequency we have :

$$W_{ff} = 1.53 \times 10^{-25}\, T_e^{1/2}\, n_e^2\, Z_{eff}\, g_{ff}(T_e) \qquad (3.11)$$

where: W_{ff} has units of (ergs $cm^{-3}\, s^{-1}$), T_e is in eV, n_e is in cm^{-3}, g_{ff} is the frequency integrated Gaunt factor and :

$$Z_{eff} = \sum_s \sum_Z \frac{N(s,Z)\, Z^2}{n_e} \qquad (3.12)$$

Free - Bound Radiative Recombination

A discontinuous contribution to the emission spectrum is made whenever a free electron with kinetic energy E_c collides with an ion of charge state Z and is captured in an energy level n. A photon of energy $h\nu = E_c + \chi^n_{z-1}$ is emitted, where χ^n_{z-1} is the ionization potential at the quantum level n. The reason for the discontinuous spectrum is that only photons with energy greater than χ^n_{z-1} are emitted. The formula for the power emitted per unit frequency and volume from

radiative recombination of a particular ion (assuming a Maxwellian distribution of electrons) is [6-7]:

$$(3.13)\quad \frac{dW_{fb}}{dh\nu} = \frac{6.4 \times 10^{-40}}{T_e^{1/2}} n_e\, n(s,Z)\, Z^2 \sum_{n>n_{min}}^{\infty} \bar{g}_{fb}(h\nu, Z, n)\, e^{-h\nu/T_e} \times$$

$$\times \left(\frac{2}{n^3} \frac{Z^2 \chi_H}{T_e} e^{Z^2 \chi_H / n^2 T_e} \right)$$

units (ergs cm^{-3} Hz^{-1}) where : g_{fb} is the free bound Gaunt factor and χ_H is the ionization potential of hydrogen. One point to notice here is that the presence of impurity ions in the plasma produces an enhancement over the hydrogen Bremsstrahlung of [8]:

$$\zeta \approx \frac{f_z Z^4 \chi_{n,\infty}}{k\, T_e} \qquad (3.14)$$

where f_z is the fraction of impurity ions in the charge state Z.

Impurity line emission spectra

Emission spectra measured on many tokamaks[9] and RFP's[10] show that radiation in the soft x-ray region is mostly due to impurity spectral lines. Even a small abundance of impurities can produce a radiative flux that dominates the other mechanisms.

When an electron collides with an ion it may excite it to a higher energy level. A deexcitation to various lower energy states follows, that produces photons of energies equal to the energy difference between excited and final state. The power radiated during an instantaneous radiative decay of an ion in a charge state Z to all

N possible levels is [11]:

$$P_{line} = n_e\, n_{ion} f_z \sum_{n=0}^{N} Q_n\, \Delta E_n \qquad (3.15)$$

where : f_z is the fraction of impurity ions in charge state z, ΔE_n are all the possible transitions and Q_n are the excitation rate coefficients.

Among some of the impurities that have been identified in MST are oxygen, carbon, and aluminum. The diagnostic used to measure these UV signals was a Minuteman 302-VM .2 meter vacuum ultraviolet monochrometer, while the OIII and CIII lines were measured using interference filters (fig. 3.2). For temperatures higher than about 300 eV, carbon is fully stripped of all its electrons while oxygen is ionized up to charged states OVII and OVIII as seen in figure 3.12.

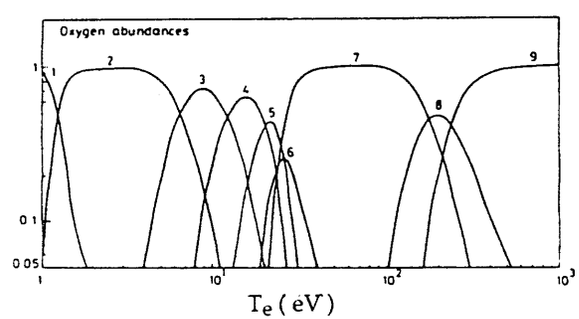

Figure 3.12. *Equilibrium ionisation state distribution for oxygen. [From P. G. Carolan and V. A. Piotrowicz [11].]*

Example

As an example we will estimate the power emitted through each of the above mentioned processes by a plasma that has the following parameters :

- plasma temperature = 300 eV
- plasma density = 1×10^{13} cm^{-3}
- $Z_{eff} = 2$
- fractional concentration of OVII = 2%

From equation (3.10) we have that the Bremsstrahlung radiation component is : $W_{ff} = 53 Watts/m^3$. The enhancement factor from eq (3.14) is about 200 which makes the free-bound contribution : $W_{fb} = 1 \times 10^4 Watts/m^3$. From time dependant Coronal Model calculations performed by P . G Carolan and V. A Piotrowicz[11] we can estimate the total power radiated from the impurity OVII for the plasma parameters mentioned above. From figure 3.13 : $P_{OVII} = 8.3 \times 10^3 Watts/m^3$, assuming τ=1 mec. Notice that the line radiation is comparable to the recombination radiation. Now we can estimate how this reflects on the contribution of the various emission processes to the soft x-ray signals measured with the 7.6 µm beryllium filtered SBD's. The emissivity expected to be measured by the SXR imaging system from recombination radiation for the plasma parameters listed above is :

$$Emissivity_{f\text{-}b} = enhancement_{f\text{-}b} \times 1.53 \times 10^{-25}\, T_e^{1/2}\, n_e^2\, Z_{eff} \times$$

$$\times \int_0^{\infty} R(E)\, e^{-E/T_e}\, d\frac{E}{T_e} \quad erg/cm^3$$

This formula gives an $Emissivity_{f\text{-}b} = 4 \times 10^2 Watts/m^3$. The emissivity expected to be measured by the SXR imaging system if only OVII line radiation were present is:

$$Emissivity_{OVII} \approx 8.25 \times 10^3\, R(E{=}574\ eV)\ Watts/m^3 = 1.6 \times 10^2\ Watts/m^3$$

where R(E=574 eV) is the transmition of the SBD filter system at 574 eV which corresponds to the energy of the 1s2p $^1P_1$ —> $1s^2\ ^1S_0$ OVII emission line.

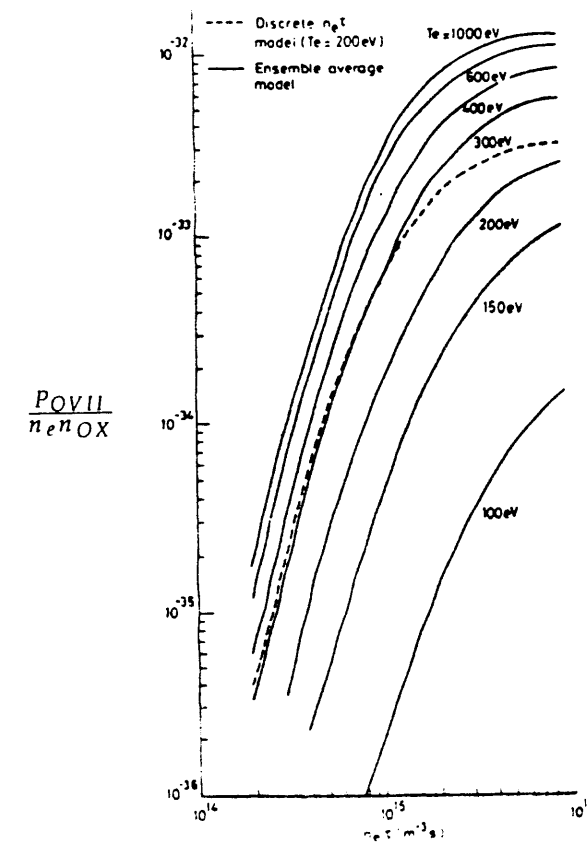

Figure 3.13. $\frac{P_{OVII}}{n_e n_{OX}}$ ($W m^3$) is calculated from a time dependent Coronal Model.

[From P. G. Carolan and V. A. Piotrowicz[11]]

It is clear from this example that the line radiation can be a very important radiation loss channel in plasmas and has a significant contribution to the soft x-ray signals measured by the SBD's. The spectrum obtained from running an impurity code (obtained from Ray Fonk) with input parameters : 300 eV plasma temperature, 2% oxygen , 1% aluminum concentration and .3 mil beryllium filter shows that the oxygen and aluminum impurity line dominate the SBD signal (figure 3.14).

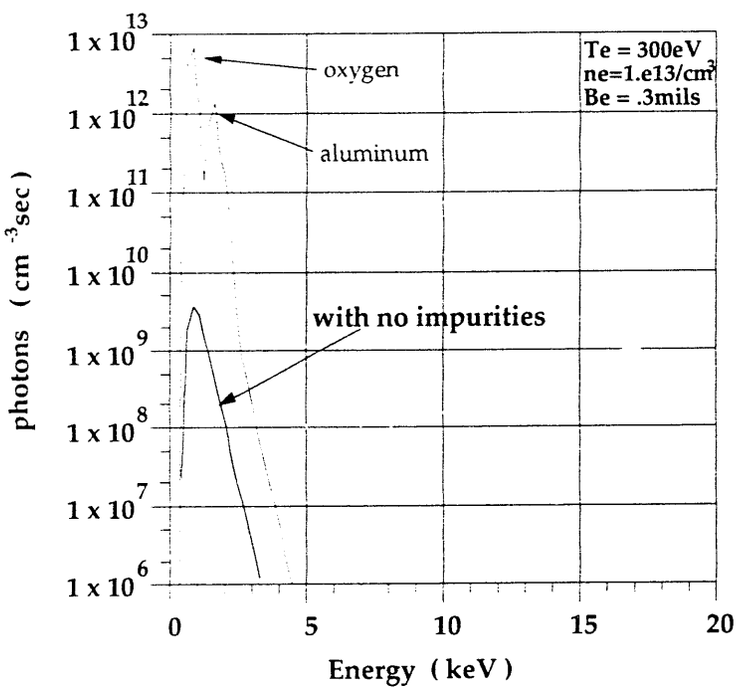

Figure 3.14. *Soft x-ray radiation rate of a plasma with the following impurity concentrations: carbon = 3%, oxygen = 2%, aluminum = 1%.*

2.6 Plasma Emissivity

Let S(r,θ,E) represent the energy emitted by the plasma at the location (r,θ) per unit time, volume and solid angle. The signal measured by a surface barrier detector "viewing " a portion of the plasma can be expressed as:

$$I_p = \int_{\substack{over\\viewing\\volume}} \int_0^\infty R(E)\, S(r,\theta,E)\, dE\, dV \qquad (3.16)$$

where R(E) is the transmission function of the SBD - filter system and I_p is the energy per unit time received by the detector. If ω(r,θ) is the solid angle sub-tended by the active area of the SBD viewed through the collimator from the location (r,θ) then expression (3.16) can be written as :

$$I_p = \int_{V_{plasma}} \int_0^\infty R(E)\, S(r,\theta,E)\, \omega(r,\theta)\, dE\, dV = \int_{V_{plasma}} \varepsilon(r,\theta)\, \omega(r,\theta)\, dV$$

$$where: \qquad \varepsilon(r,\theta) = \int_0^\infty R(E)\, S(r,\theta,E)\, dE \qquad (3.17)$$

The quantity ε(r,θ) is referred to as the emissivity of the plasma . The goal of a reconstruction technique is to determine the emissivity ε(r,θ) from a given set of measurements (projection values). We notice from equation (3.17) that ε(r,θ) does not represent the total power emitted per unit volume but only a small fraction that is determined by the transmission function of the detector-filter system. Ideally one would want to have a detector with a good energy resolution. If that were the case

one could make the approximation $R(E) = \delta(E - E_0)$, where E_0 is the desired energy of observing the plasma. (Experimentally this can be achieved by the use of a Bragg crystal or a multilayer.) From equation (3.17) we obtain:

$$\varepsilon(r,\theta) = S(E_0, r, \theta)$$

This implies that the use of detectors with good *energy resolution* for soft x-ray tomography can provide information on the total power emitted at the selected energy E_0 for any location (r,θ).

A large variety of reconstruction algorithms are used in many fields of science. The first application of image reconstructions was made in radio astronomy around 1950 in order to obtain better angular resolution of the radio emission from various celestial objects. Today image reconstruction and restoration techniques are commonly used in X-ray astronomy, for medical application, on electron images and in plasma physics. In magnetically confined plasma devices the number of projection values can be small due to the limited access around the torus. A technique that has proven to have advantages under such circumstances is the Maximum Entropy Method first developed by B. Roy Frieden[12].

3.7 The Maximum Entropy Method

Given a set of projection values there can exist many feasible images that are consistent with the measurements. In other words there is not a unique solution for the emissivity that satisfies the constraints set by the detected signals. This occurs because experimentally there is a limited amount of information provided by the SXR detectors . Out of all the possible solutions the reconstruction algorithm must

choose the image that is noncommittal to any unmeasured data and satisfy the constraints posed by the projection values. For most of the reconstructions, unless otherwise mentioned the maximum entropy method (MEM) is employed to select a single image out of the feasible set. A description of the method similar to the one adopted by A. Holland and G.A Navratil[1] follows .

The emission volume that is sampled by the SBD's is divided into N cells. Their size is determined from the number , spacing and collimation of the available SXR detectors. The cell-averaged emissivity will be denoted as E_c. The configuration entropy of the system is :

$$Q = -\sum_{c=1}^{nc} E_c \ln E_c - \left(\frac{\bar{\sigma}_d}{\bar{S}}\right) \sum_{d=1}^{nd} N_d \ln N_d \qquad (3.18)$$

where : nc is the total number of cells

nd is the total number of detectors

$\bar{\sigma}_d$ is the average standard deviation of detector d

$$\bar{S} = \frac{1}{nc + nd} \sum_{c=1}^{nc} \sum_{d=1}^{nd} W_{dc}$$

W_{dc} are the weighting functions as defined by equation (3.2).

The second sum in eq. (3.18) includes the entropy due to the noise in the system. (see eq. (3.23)) . Some authors argue that the expression for the entropy depends on the method of detection used. The expression adopted here is most commonly used for photon counting experiments. An axiomatic derivation of the maximum entropy method is given by J . E Shore and R. W. Johnson[13]. The same formula can be derived from a statistical mechanics viewpoint[1].

One interesting and useful aspect of the MEM is its ability to accept prior information of the image to be reconstructed. For instance MHD equilibrium codes indicate that the plasma flux surfaces are shifted outward by an amount specified by the Grad-Shafranov equation. Also the plasma emissivity is expected in most cases to be peaked close to the magnetic axis. Additional information on the structure of the flux surfaces can also be obtained from magnetic coils at the wall, and many more possibilities exist. To include additional information the formula for the entropy is slightly modified to:

$$Q = -\sum_{c=1}^{nc} E_c \ln \frac{E_c}{G_c} - \left(\frac{\overline{\sigma_d}}{\overline{S}} \right) \sum_{d=1}^{nd} N_d \ln N_d \qquad (3.19)$$

where G_c is the zero order approximation for the emissivity profile obtained from other sources. For the present calculations the zero order approximation is a parabolic emissivity profile peaked and shifted slightly outwards. Clearly when using the expression (3.18) without considering prior information the default is just a flat profile . It turns out that even a rough estimate of G_c produces a large improvement in the reconstructed image[14].

The maximization of the entropy under the constraints posed by the measurements is performed by using Lagranges Undetermined Multipliers. For our present configuration of detectors and cells the entropy is a function as seen from equation (3.18) of nc + nd variables , which, however, are not independent. The nc+nd variables are constrained by the following relations :

1. The first set of constraints state that the measured signals I_d are equal to the sum of the weighted emissivities of each cell. A noise factor n_d defined in eq. (3.23) is

included since the measured signals are expected to contain noise from various sources such as SBD and pre-amp noise.

$$\sum_{c=1}^{nc} E_c W_{dc} - I_d + n_d = 0 \ , \quad \Phi_i = 0 \ \ with \ i = 1 \ , nd \qquad (3.20)$$

2. The total emissivity is the sum of the emissivities from each cell :

$$\sum_{c=1}^{nc} E_c - I_0 = 0 \ , \ \Phi_0 = 0 \qquad (3.21)$$

3. The departure of the expected projection values (derived from the reconstructed image) from the measured projection values is characterized by the quantity χ^2. To place a bound on χ^2 we use χ^2 statistics to impose the constraint:

$$\chi^2 = nd, \text{where } \chi^2 = \sum_{d=1}^{nd} \left(\frac{I_d - \sum_{c=1}^{nc} E_c W_{dc}}{\sigma_d} \right)^2 = \sum_{d=1}^{nd} \frac{n_d^2}{\sigma_d^2}, \Phi_{nd+1} = 0 \qquad (3.22)$$

We can express the noise in dimensionless units by setting :

$$n_d = \overline{\sigma_d} \, (N_d - D_d) \qquad (3.23)$$

This way N_d is always positive and dimensionless with D_d taking care of the

negative contributions to the noise.

The critical points of eq. (3.18) are the values of E_c and N_d for which **dQ** = 0 . Now by introducing a set of nd+2 Lagrange Multipliers $\lambda_0 \ldots \lambda_{nd+1}$ we can obtain (see appendix A1) expressions for E_c and N_d:

$$E_c = exp\left(-1 + \lambda_0 + \sum_{d=1}^{nd} \lambda_d W_{dc}\right) \tag{3.24}$$

$$N_d = exp\left[-1 + \lambda_d \overline{S} - \frac{2\,\overline{S}\,\lambda_{nd+1}^2}{nd\,\sigma_d^2\,\overline{\sigma}_d}(N_d - D_d)\right] \tag{3.25}$$

The Lagrange Multipliers are calculated by substituting eq (3.24) and (3.25) into the constraint equations $\Phi_i = 0$, i = 0 , nd+1.

We can solve the nonlinear system of nd+2 equations by utilizing a Newton-Raphsons Method. An outline of the method follows .The set of nonlinear equations to be solved are :

$$\Phi_i = \left(\lambda_0, \lambda_1, \ldots, \lambda_{nd+1}\right) = 0 \quad i = 0\,,\, nd+1$$

We begin with an initial guess for the roots $\lambda_0, \lambda_1, \ldots, \lambda_{nd+1} = \Lambda$ and make a Taylor expansion in the neighborhood of Λ :

$$\Phi_i(\Lambda + d\Lambda) = \Phi_i(\Lambda) + \sum_{j=0}^{nd+1} \frac{\partial \Phi_i}{\partial \lambda_i} d\lambda_i + O\left(\delta\Lambda^2\right)$$

Since we want $\delta\Lambda$ to move Φ_i closer to zero we obtain:

$$\sum_{j=0}^{nd+1} \frac{\partial \Phi_i}{\partial \lambda_i} d\lambda_j = -\,\Phi_i \quad with \quad i = 0\,,\, nd+1$$

This is a matrix equation, and the corrections $\delta\lambda_i$ can be found by LU decomposition. Usually it takes 10 to 15 iterations for the algorithm to converge (ie the corrections $\delta\lambda_i$ and the values of Φ_i become very small). Once the values of the Lagrange Multipliers our found the emissivity is obtained from equation (3.24).

The accuracy with which the present SXR imaging system reconstructs various emissivity profiles can be tested by making phantom sources. After performing many reconstructions of phantom sources one can obtain some understanding of what can and cannot be considered a reliable unfolded emissivity profile.

References for chapter 3.

1. A . Holland and G . A .Navratil , " *Tomographic analysis of the evolution of plasma cross sections.* " Rev . Sci. Instrum. 57 (8) ,August (1986).

2. Y. Nagayama, J. Appl. Phys. 62, 2701 (1987).

3. S . T. Stephenson , " *The continuous x-ray spectrum* " in Handbuch der Physik Vol XXX (1957) 337 .

4. H. W. Koch , J. W. Motz , Rev. Mod. Phys. 31 (1959) 920.

5. P. J. Brussaard , H. C. Van De Hulst , Rev. Mod. Phys. 34 (1962) 507

4. L. Jr. Spitzer , " *Physics of fully ionized gases* " Interscience publishers , New-York (1962)

7. De Michelis and Mattioli , Nuclear Fusion , Vol 21 , No. 26 (1981) *"Soft x-ray spectroscopic diagnostics of laboratory plasmas "*

8. R . W . P McWhirter and H . P . Summers " Applied Atomic Collision Physics Vol 2 Plasmas " Academic Press Inc (1984).

9. N. J. Peacock, M. H. Hughes, H. P. Summers, M. Hobby, M. W. D. Mansfield, and S. J. Fielings (1979). Plasma Phys. Controlled Nucl. Fusion Res. proc. Int. Conf. , 7th Innsbruck , (1978).

10. G . A. Wurden *"Soft x-ray array results on the ZT-40M reversed field pinch."* Phys. Fluids 27 (3) , March (1984) .

11. P . G. Carolan and V . A . Piotro vicz *"The behaviour of impurities out of Coronal Equilibrium "* Plasma Physics Vol 25 pp 1065 to 1086 (1983) .

12. B . R. Frieden *"Restoring with maximum likelihood and maximum entropy* , J . Opt . Soc . Amer . 62 , (1972) , pp 511-518

13. J . E. Shore and R . W. Johnson , *"Axiomatic Derivation of maximum entropy and the principle of minimum cross entropy "* IEEE Trans. Inf Theory IT - 26 , 26 (1980).

14. J . G. Sanderson , *"Reconstruction of fuel bundles by a maximum entropy method "* IEEE Trans Nucl. Sci. Ns - 26, 2685 (1979).

Chapter 4

The Soft X -Ray Target Probe.

Introduction

Experiments performed on various RFP's show that a large fraction of the radial power flux is carried by superthermal electrons, thus creating an undesirable loss channel. Results from hot electron measuremants in ZT -40M[1], MST[2], TPE - 1RM15[3] and STP - 3M[4] all confirm the existence of a unidirectional flow of energetic electrons along **B**. However some of their properties appear to vary from one device to the other. Edge electron measurements on MST show that hot electrons do carry away a substantial amount of the total ohmic input power. The peaking of the measured target soft x-ray signals along **J** cannot be accounted for by any reasonable electron drift velocity. The contribution of the hot electrons to the dynamo effect in RFP's will be studied by correlating soft x-ray target signals with the magnetic field at the wall. The presence of this nonthermal tail contributes to the observed spectral emission in the soft x-ray region. A rapid ionization of edge impurities is also noticed during the MHD relaxation phase. A carbon SXR target probe and an electrostatic energy analyzer were used for the hot electron experiments on MST. Most of the results presented in chapter VII will focus on the soft x-ray target probe although some differences in results obtained from these two diagnostics will be mentioned. In this chapter, I will describe the main features of the SXR target probe and show how the temperature, density, power flux and current density of the hot electrons is obtained.

4.1 Description of the SXR target probe.

The basic features of the target probe are shown in figure 4.1 . Electrons that enter the collimator and strike the carbon target produce x-rays that are viewed by three differently filtered SBD's. The advantage of having the target and detectors mounted on the same probe is that the distance between them remains the same. In addition the radiation seen by the detectors is only due to electrons hiting the target and does not include plasma x-rays. An important feature of the diagnostic is a filter wheel that is attached in front of the SBD's which enables a relative calibration of the entire system including collimation, SBD sensitivity, differences in filter thicknesses and any differences in pre amp gains. The thickness of the filters were chosen such that the energy cutoff was well above the carbon K_α emission line at .277 keV . The effect of the probe on the plasma was monitored by looking at the plasma current and various impurity signals , especially that of CIII at 4647 A .

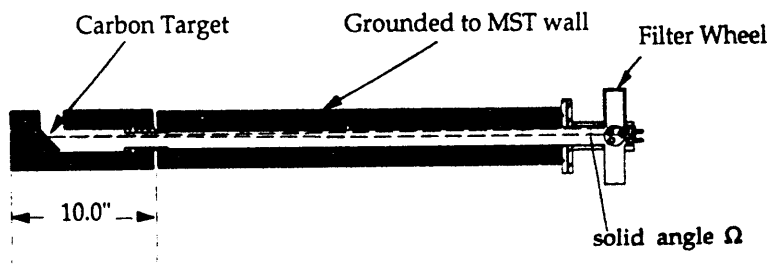

Figure 4.1. *Soft x-ray target probe. Features a carbon collimated target, a filter wheel for relative calibration and 3 SBD's with Beryllium filters of thickness .3 mils , .6 mils and .9 mils.*

4.2 Analysis of soft x-ray target data

The temperature of the electrons striking the target can be calculated from the ratio of the soft x-ray signals of differently filtered SBD's. Similar techniques have been applied for measuring hot electron temperatures on ZT - 40M[6], the turbulent heating experiment in Texas[6], the Phaedrus mirror device[7] and the Constance II mirror experiment at MIT[8].

The power spectrum S(E) of the photons emitted from a target due to an incident distribution f(v) is approximately [9]:

$$S(E) = \int_0^\infty dv^3\, \hat{n} \bullet \bar{v} f(v)\, C\, Z \left(\frac{1}{2} m\, v^2 - E\right) \qquad (4.1)$$

where: Z is the atomic number of the target, C = 100 $erg^{-1} sr^{-1}$ and n is the unit vector perpendicular to the target face.

We assume that the distribution function of the incident electrons is a shifted Maxwellian of the form :

$$f(v) = \left(\frac{m_e}{2\pi T_{e\perp,h}}\right)\left(\frac{m_e}{2\pi T_{e\parallel,h}}\right)^{1/2} e^{-m(v_{\parallel,h}-v_d)^2/2T_{e\parallel,h}}\; e^{-mv^2_{\perp,h}/2T_{e\perp,h}} \qquad (4.2)$$

We integrate equation (4.1) with the constraints that :

$$\frac{1}{2} m\, v^2 > E$$

$$v_{\parallel hot} \cos\theta > 0$$

$$v_\perp \cos\varphi \sin\theta > 0$$

where θ is the angle between **n** and **v**, (see figure 4.2), and φ is the gyrophase angle.

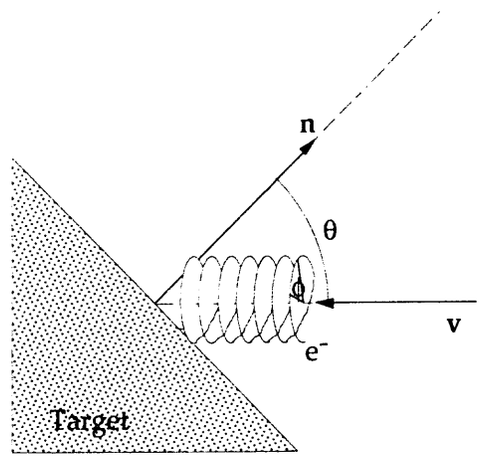

Figure 4.2. *Angles θ and φ.*

For the case where θ is 0° (target facing the hot electrons) and $T_{\perp h} = T_{\parallel h}$ we obtain :

$$S(E) = 2\, C\, Z\, n_e \left(\frac{m_e}{2\pi T_{e,h}}\right)^{3/2} \pi \frac{T_{e,h}}{m_e} \left[\Xi_1(E) + \Xi_2(E)\right] \qquad (4.3)$$

where $\Xi_1(E)$ and $\Xi_2(E)$ are :

$$\Xi_1(E) = \left(\frac{2T^2_{e,h}}{m_e}\right) e^{-E/T_{e,h}} \frac{e^{-\zeta_D^2}}{4\zeta_D^2}\left[1 - \left(2\zeta_D\sqrt{E/T_{e,h}} + 1\right) e^{-2\zeta_D\sqrt{E/T_{e,h}}}\right]$$

$$\Xi_2(E) = \left(\frac{2T^2_{e,h}}{m_e}\right) \frac{\sqrt{\pi}}{2} erfc\left(\sqrt{\frac{E}{T_{e,h}}} + \zeta_D\right)\left[\left(\frac{E}{T_{e,h}} - \frac{5}{2}\right)\zeta_D - \zeta_D^3\right] +$$

$$+ \left(\frac{T^2_{e,h}}{m_e}\right)\left(2 + \zeta_D^2 - \zeta_D\sqrt{\frac{E}{T_{e,h}}}\right) e^{-\left(\sqrt{\frac{E}{T_{e,h}}} + \zeta_D\right)^2}$$

In the limit that the streaming the streaming parameter $\frac{V_{Drift}}{V_{Thermal}} = \zeta_D \rightarrow 0$, we obtain the power spectrum :

$$S(E) = 2\,C\,Z\,n_e \left(\frac{m_e}{2\,\pi\,T_{e,h}} \right)^{3/2} \pi \frac{T_{e,h}^3}{m_e^2} \left(2 + \frac{E}{T_{e,h}} \right) e^{-E/T_{e,h}} \qquad (4.4)$$

$T_{e,hot}$ Measurement.

Experimentally we measure a current I_{SBD} collected in a SBD . This is related to the power absorbed in its depletion layer by P_{dep} (Watts) = 3.6 x I_{SBD} (A).

From previous discussion we have that the power absorbed in the depletion layer per cm^2 of the target area per steradian is :

$$P_{abs} = 4.5\times10^{15}\, Z_{tg}\, n_{e,h}\, T_{e,h}^{5/2} \int_0^\infty \left(2 + \frac{E}{T_{e,h}} \right) R(E)\, e^{-E/T_{e,h}}\, d\frac{E}{T_{e,h}} \qquad (4.5)$$

units (watts cm^{-2} $steradians^{-1}$, ergs , cm^{-3}), where Z_{tg} is the atomic number of the target, T_{hot} is the hot electron temperature and R(E) is the response function of the system filter-S.B.D.

A useful aspect of eq. (4.5) is that the ratio of the signals from two differently filtered SBD's viewing soft x-rays emitted by a target will be a function of the hot electron temperature alone :

$$\frac{P_{abs1}}{P_{abs2}} = \frac{\int_0^\infty \left(2 + \frac{E}{T_{e,h}} \right) R_1(E)\, e^{-E/T_{e,h}}\, d\frac{E}{T_{e,h}}}{\int_0^\infty \left(2 + \frac{E}{T_{e,h}} \right) R_2(E)\, e^{-E/T_{e,h}}\, d\frac{E}{T_{e,h}}} = \Phi(T_{e,h}) \qquad (4.6)$$

This ratio of SBD signal vs hot electron temperature is plotted in figure 4.3. The assumptions that enter into the hot electron measurement with this technique are :

a) The hot electrons are assumed to have a half Maxwellian distribution

b) The filters (.3 mil Be) - SBD system has a response of 2 % at 600 eV , so the calculated temperatures are strongly influenced by a non - Maxwellian tail in the electron distribution, if it exists. One advantage of this technique is real time $T_{e,hot}$ measurements with fast time response. This makes the temperature data suitable for determining fluctuation power spectra over a large frequency domain.

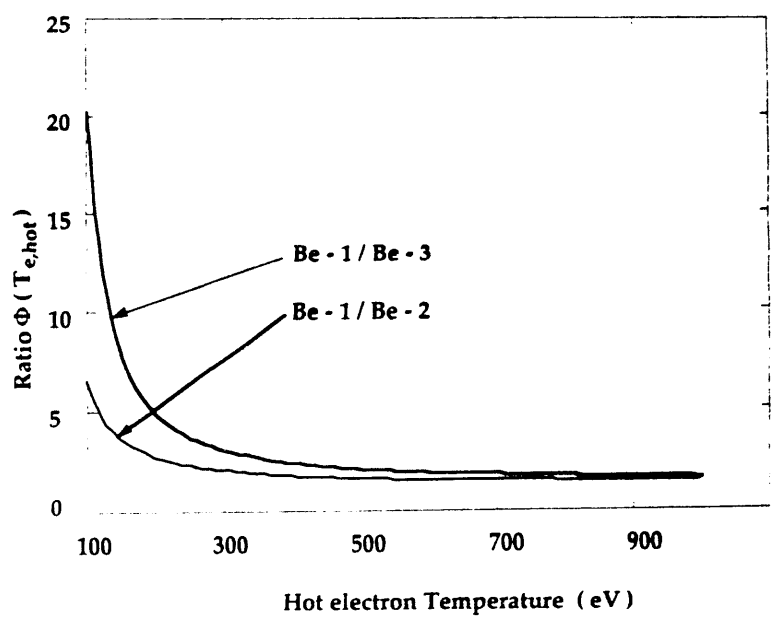

Figure 4.3. *These ratios are used to calculate the hot electron temperatures. Each curve corresponds to the ratio of two differently filtered SBD's. The filter thicknesses used are : Be-1 = .3 mils, Be-2 = .6 mils, Be-3 = .9 mils.*

References for chapter 4

1. J. C. Ingraham, R. F. Ellis, J. N. Downing, C. P. Munson, P. G. Weber and G. A. Wurden. "*Energetic electron measurements in the edge of a reversed field pinch.*" Phys. Fluids B **2** (1) January (1990).

2. G. Chartas, S. A. Hokin, M. Stoneking, F. Venneri. "*Edge electron measurements in the MST reversed field pinch.*" Presented at the APS meeting, Division of Plasma Physics, (1990).

3. "*Soft x-ray measurements in TPE - 1RM15 reversed field pinch*". Presented at the U.S./ Japan RFP workshop March 12 -15 (1990), Madison, U.S.A.

4. Shoichi Shiina, Katunori Saito, Hideki Arimoto, Akio Matsuoka, Syuichi Yamada, Saduo Masamune, Akiyoshi Nagata and Koichi Sato. "*The measurement of soft x - rays from the STP - 3 (M) reversed field pinch plasma.*" Journal of the Physical Society of Japan. Vol 56 No 4 April (1987) pp. 1282 - 1285.

5. G. A. Wurden et al." *RFP experiments : Results from ZT - 40M and ZT - P.* " Presented by G. A. Wurden at the Proc. Int. School of Plasma Physics and Physics of mirrors, RFP's and compact Tori . (Varenna) Vol I (1987).

6. Roger D. Bengtson, K. W. Gentle, J. Jancarik, S. S. Medley, P. Nelson and P. Phillips. " *Observations of plasma heating in a turbulent torus.*" The Physics of Fluids, Vol, 18 No. 6 June (1975).

7. D. C. Sing, N. Hershkowitz, J. E. Scharer. " *Shift in plasma column position produced by azimuthally asymmetric electron heating in a tandem mirror.* " Phys. Fluids 29 (12) December (1986).

8. M. E. Mauel (1982) Ph.D dissertation, Dept. of Electrical Engineering MIT reprinted as MIT Plasma Fusion Center report PFC/RR - 82 - 29.

9. S. T. Stephenson, "*The continuous x - ray spectrum*" in Handbuch der Physik Vol XXX (1957) 337.

$n_{e,hot}$ Measurement.

The derivation of the hot electron density from SXR-target probe measurements involves larger error bars introduced by the effective target area , the roughness of the target surface and the strong dependence on $T_{e,hot}$. Having this in mind we obtain from equation (4.5) :

$$n_{e,h} = \frac{P_{abs}}{1.078 \times 10^{-19} \times T_{e,h}^{5/2} \times Int(T_{e,h}) \times \Omega} \qquad (4.7)$$

units (cm^{-3} , Watts, eV) ,where : $\Omega = S / R^2$, see figure (4.1).

$$Int(T_{e,h}) = \int_0^\infty \left(2 + \frac{E}{T_{e,h}} \right) R(E)\, e^{-E/T_{e,h}}\, d\frac{E}{T_{e,h}}$$

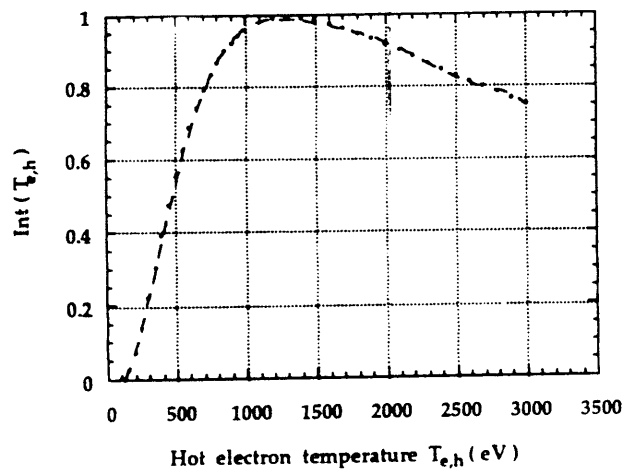

Figure 4.4. *Integral of the tranmission function of the SBD - system, times the power spectrum of the target photons given by equation (4.4).*

Measuring the power caried by the hot electrons.

The power deposited by the hot electrons per unit area of target is :

$$\frac{P_{e,h}}{A} = n_{e,h} \int_0^\infty v \left(\frac{1}{2} m\ v^2\right) f(v)\ dv = n_{e,h} (2\ \pi\ m_e)^{-1/2}\ T_{e,h}^{3/2} \qquad (4.8)$$

Measuring the current density of the hot electrons

One may also compare the total plasma current density with that carried by the hot electrons :

$$J_{e,h} = n_{e,h}\ e \int_0^\infty v\ f(v)\, dv = n_{e,h}\ e\ (2\ \pi\ m_e)^{-1/2}\ T_{e,h}^{1/2} \qquad (4.9)$$

Equations (4.6) to (4.9) were implemented for analyzing the sxr target probe data taken on MST. The results will be presented in chapter 7.

Chapter 5

Review of RFP Dynamo Theory.

Introduction

Much of the existing theory related to the dynamo was originally developed in order to explain the observed sustainment and generation of magnetic fields in stars, pulsars, the interstellar medium (ISM) and black holes. The concept of converting hydrodynamic motions of a plasma into magnetic energy was first proposed by Larmor[1] in 1919. His theory was able to explain the existence of the Earth's magnetic field and the Sun's 11 year magnetic cycle. The conditions under which a dynamo may exist were first examined by Cowling[2]. He showed that an axisymmetric magnetic field cannot be maintained by fluid flows alone. An important contribution to the dynamo theory was made by Steenbeck, Krause and Radler[3] who introduced a method that could predict the mean magnetic field structure given an original seed field. The key physical quantity in their theory of mean - field electrodynamics is the mean helicity of the turbulence. Concurrent research in dynamo theory is focused on calculating the back - reaction of the magnetic field on the fluid motion.

The question that arises now is; to what extent can we apply these theories to laboratory plasmas? From the definition of the magnetic Reynolds number $R_m = \frac{L\,v}{\nu_m}$, where L is a characteristic length v is a characteristic velocity of the hydrodynamic motion and ν_m is the magnetic viscosity , we notice that the main difference between a laboratory and astrophysical plasma lies in the characteristic scale length. For astronomical objects L can be of the order of parsecs while in a laboratory plasma L

is of the order of a meter. So in general we expect laboratory plasmas to have smaller magnetic Reynolds numbers. Another important question is whether the observed flux generated in RFP's is a turbulently driven or a coherent process. By coherent we mean that only a few modes reconnect and are responsible for the dynamo. The reason why one may expect the dynamo to be a coherent process is that resistive tearing modes have been experimentally observed in RFP's, and usually only a few are dominant. For example, in MST the dominant tearing modes have toroidal mode numbers of 5, 6, 7. Also, numerical MHD simulations can produce sustainment from the nonlinear interaction of a small number of modes. Since the existence of the tearing modes appears to be crucial for the RFP dynamo we will continue with a brief description of their properties.

5.1 Resistive Tearing Modes

For a perfectly conducting plasma the concept of frozen field lines has been used in many cases to explain various plasma behavior. The evolution of the magnetic field in a plasma of resistivity η can be deduced using Ohm's law and Maxwell's equations.

$$\vec{E} + \vec{v} \times \vec{B} = \eta \vec{j}$$

$$\frac{\partial \vec{B}}{\partial t} = -\vec{\nabla} \times \vec{E}$$

$$\vec{\nabla} \times \vec{B} = \mu_0 \vec{j}$$

From the above equations we obtain:

$$\frac{\partial \vec{B}}{\partial t} = \vec{\nabla} \times \vec{v} \times \vec{B} + \frac{\eta}{\mu_0} \nabla^2 \vec{B} \qquad (5.1)$$

The first term on the right hand side of equation (5.1) represents the coupling of the plasma to the magnetic field , while the second term represents the slipping of the magnetic field lines when resistivity is introduced. Equation (5.1) also provides the magnetic field diffusion time constant $\tau_R = \frac{\mu_0 L^2}{\eta}$,where L is the characteristic scale length. The difficulty in determining τ_R arises from the uncertainty of knowing the characteristic length L. If we were to take L to be the order of the MST minor radius, τ_R would be a few msecs while τ_A (Alfven time) would be of the order of a few microseconds. At first it appears that if $\tau_R >> \tau_A$ were true , resistivity would not be important; however, we will show that in certain narrow layers of the plasma resistivity plays a dominant role.

We assume that the magnetic field and fluid velocity can be written as the sum of an equilibrium and perturbed part :

$$\vec{B} = \vec{B}_0 + \vec{B}_1$$

$$\vec{v} = \vec{v}_0 + \vec{v}_1$$

Keeping only first order quantities of eq. (5.1) we obtain:

$$\frac{\partial \vec{B}_1}{\partial t} = \vec{\nabla} \times \left(\vec{v}_1 \times \vec{B}_0\right) - \frac{\eta}{\mu_0} \nabla^2 \vec{B}_1 \qquad (5.2)$$

In order to simplify the problem we assume the magnetic field has components only in the x, z plane and is only a function of the y coordinate, ie. $\vec{B} = B_x(y)\,\hat{x} + B_z(y)\,\hat{z}$. The introduction of a perturbation $\vec{k} = k_x\,\hat{x} + k_z\,\hat{z}$ will cause other plasma quantities to vary according to :

$$A_1(x, y, z, t) = A(y)\, e^{i k_x x + i k_y y + \gamma t} \qquad (5.3)$$

where γ is the growth rate. If we take the y component of eq. (5.1) we obtain :

$$\gamma \vec{B}_y = i\left(\vec{k} \cdot \vec{B}\right) \vec{v}_y + \frac{\eta}{\mu_0}\left[\frac{d^2 \vec{B}_y}{d y^2} - \vec{B}_y k^2\right] \qquad (5.4)$$

It is apparent from equation (5.4) that wherever in the plasma $\vec{k} \cdot \vec{B} = 0$ the second right hand term of eq. (5.4) will dominate. So to answer the question presented above concerning the importance of the resistivity we now can conclude that resistivity is important in narrow resistive layers where $\vec{k} \cdot \vec{B} = 0$. These layers correspond to the rational surfaces that satisfy $q = \frac{m}{n}$ since :

$$\vec{k} \cdot \vec{B} = 0 \Leftrightarrow \left(\frac{m}{r}\hat{\theta} + \frac{n}{R}\hat{\varphi}\right) \cdot \left(B_\theta \hat{\theta} + B_\varphi \hat{\varphi}\right) = 0 \Leftrightarrow q = \frac{m}{n}$$

where r, R are the minor and major radius respectively. Formal analysis of the MHD equations[4] can provide an estimate of the width ε of the resistive layer and the growth rate γ :

$$\varepsilon = \left(\frac{\gamma \rho \eta}{k^2 \left(\frac{d B}{d y}\right)^2}\right)^{1/4}$$

$$\gamma = \tau_R^{-3/5}\, \tau_A^{-2/5}$$

5.2 The MHD dynamo

It has been shown that for a homogeneous isotropic velocity field which is non mirror symmetric , a dynamo can exist described by the following equation:

$$\frac{\partial \vec{B}}{\partial t} = \vec{\nabla} \times \left\langle \vec{v} \times \vec{b} \right\rangle + \eta \nabla^2 \vec{B} \qquad (5.5)$$

where $\langle \vec{v} \times \vec{b} \rangle = \alpha \vec{B} - \beta \vec{\nabla} \times \vec{B}$, α and β are determined from the velocity field.

The first term on the right hand side of equation (5.5) is known as the generation term. A simple picture that decribes the α effect, presented by Moffat[5] is given in figure 5.1.

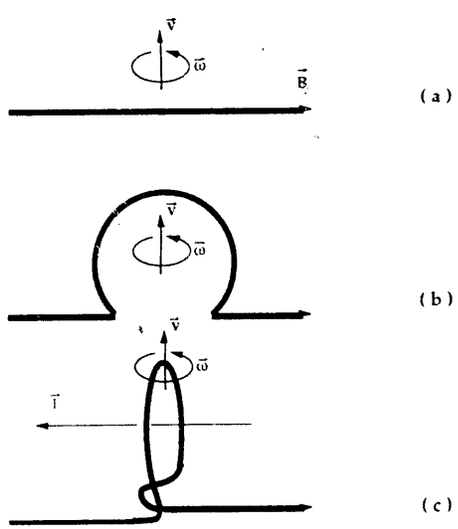

Figure 5.1 *The α - effect. Fluids possessing helicity can deform the magnetic field and produce a current parallel to the main field.*

In RFP's the electric field at the reversal surface can be expressed as :

$$\langle E(r_v) \rangle = \eta \langle J_\theta(r_v) \rangle + \sum_{m=0}^{M} \varepsilon_m \qquad (5.6)$$

The second term on the right hand side of eq (5.6) is the dynamo contribution.

$$\varepsilon_m = \sum_{n=0}^{N} \langle v_{m,n} \times b_{m,n} \rangle \qquad (5.7)$$

When the electric field at the reversal surface is positive $E(r_v) > 0$ (in the direction of the externally applied electric field) the flux inside the reversal surface decays while for $E(r_v) < 0$ the flux increases. Various MHD codes have been written that can calculate the contribution ε_m of the various modes to the MHD dynamo. However at the present time there is a disagreement in results from various 3D simulations as to the contribution of the m = 0 and m = 1 modes to the dynamo term. We will present a summary of various results obtained from numerical simulations of the magnetic reconnection in RFP's and point out the main disagreements from different codes.

5.3 Review of results obtained from numerical simulations of the magnetic reconnection in RFP's.

A study of nonlinear single helicity reconnection in a RFP was presented in a paper by Caramana et. al[6]. Essentially the full set of nonlinear MHD equations were used to follow the evolution of single helicity resistive tearing modes. Two different phases were distinguished. In the first reconnection phase, off axis current gradients drive the plasma unstable. The result is that the current on axis becomes overpeaked and the reversal surface is removed out of the plasma. Immediately following, the plasma goes through a second reconnection where the resonant surface is restored, the q on axis increases above its initial value and the plasma approaches the minimum energy state (Taylor state[7]). The first reconnection time is predicted to scale as $S^{1/2}$ and the second reconnection time as S. The cycle is repeated since diffusion will lead to the subsequent peaking of the current on axis. Transport was not included in the simulation, and magnetic Reynolds numbers of up to 10^3 were used. The effect of the nonlinear interaction of modes with *different* helicities was also not considered.

Simulation of the nonlinear MHD equations in three space dimensions by Schnack et. al.[8-9] show some differences from their previous work in which a one dimensional code was used. In this study they also consider the effect of nonlinear coupling between modes of different helicity. The evolution of the magnetic energy of the m = 1 modes is altered in the 3D case . This occurs because energy is drained away by the m = 0 , m = 2 modes that are produced through the nonlinear coupling of the m = 1 mode. The effect of adding more than one helicity is the appearance of stochastic regions due to the overlapping of neighboring m = 1 islands. For large values of $\Theta > 1.6$, they conjecture that the m = 0 island (resonant on the reversal

surface) may overlap with the m=1 islands and make the entire discharge stochastic. Calculations of the dynamo term $\varepsilon_m = \sum_{n=0}^{N} \langle v_{m,n} \times b_{m,n} \rangle$ show that a negative poloidal electric field is produced mainly by the m=1 modes. The m=0 contribution is calculated to be approximately an order of magnitude smaller. The coupling tree proposed for the m=1 driven dynamo is shown in figure 5.2. In a similar study by Holmes et. al.[10] the nonlinear interaction of tearing modes is compared in tokamaks and RFP's. In tokamaks the nonlinear coupling of tearing modes leads to a disruption of the discharge. This occurs because the resonant surfaces in tokamaks are far apart compared to RFP's and the magnetic islands can grow large before they overlap . This results in the generation of large current gradients. In RFP's, on the other hand, the resonant surfaces are closer together and magnetic islands do not grow large before they overlap. As a consequence the nonlinear interaction of tearing modes in RFP's has a stabilizing effect.

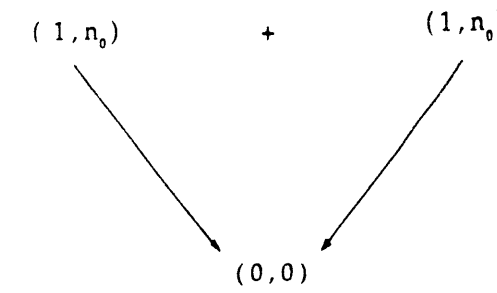

Figure 5.2 *The m = 1 coupling tree.*

Kusano and Sato[11] show that the contribution of different modes to the dynamo depends on the departure of the plasma energy from the Taylor minimum energy state. They define the relative excess energy as :

$$W^* = \frac{W_m - W_{BFM}}{W_{BFM}}$$

where W_m is the total magnetic energy of the initial state and W_{BFM} is the magnetic energy of the BFM state which has the same helicity as the initial state. The contribution of the m=0 and m=1 to the dynamo as a function of excess energy is shown in figure 5.3. For typical laboratory plasmas they claim that the excess

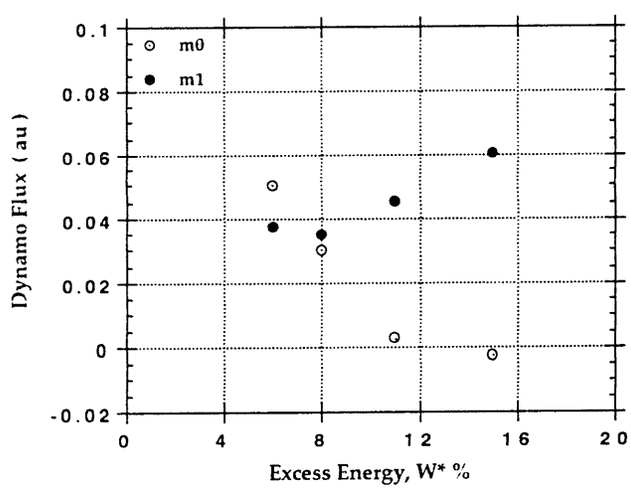

Figure 5.3 *Dynamo flux predicted from the m = 0 and m = 1 modal components as a function of the excess energy W*. [From K. Kusano, T. Sato, submitted to Nuclear Fusion.]*

energy is less than 8 % , making the nonlinear reconnection of the m=0 mode the dominant component of the dynamo. The coupling tree suggested for the m=0 dynamo is shown in figure 5.4.

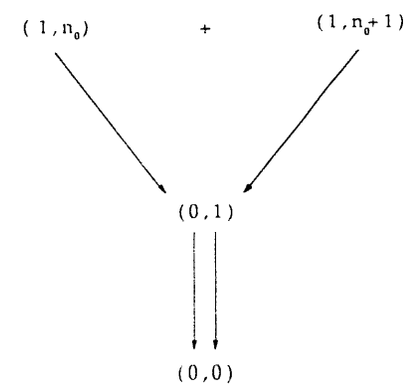

Figure 5.4 *The m = 0 coupling tree.*

5.4 The kinetic dynamo

As an alternative to the MHD dynamo Jacobson and Moses[12] have proposed a kinetic dynamo mechanism where electrons can transfer momentum across the mean field **B** due to stochasticity of the magnetic field lines. They show that a local Ohm's law is incorrect, and they provide a model based on a non-local conductivity that can explain the Woltjer - Taylor relaxation mechanism observed in RFP's. By approximating the Boltzmann equation for the long-collision-length regime they obtain an expression for the first order perturbation of the Maxwellian distribution function :

$$f^{(1)}(\vec{v}, x) = \frac{-E_{\parallel}(x)}{E_c}\left[\frac{v}{v_0}\right]^4 \cos\theta\, f^{(0)}(\vec{v}) + 2\lambda_0\left[\frac{v}{v_0}\right]^4 \left|\cos\theta\right| \frac{\partial}{\partial x}\left[D_F(x)\frac{\partial f^{(1)}(\vec{v}, x)}{\partial x}\right] \tag{5.8}$$

where E_c is the critical electric field, λ_0 is the 90° scattering length, D_F is the field line diffusivity and $v_0 \equiv \sqrt{2kT/m}$. By solving equation (5.8) they obtain quasilinear expressions for the parallel electric current density and the current density transport. Quasilinear theories consider fixed fields and assume that the particle distributions do not affect these fields.

In a self - consistent treatment (particle distribution effects on the fields is included through Ampere's law) by Terry and Diamond[13] it is found that radial transport of field aligned current is governed basically by electrostatic fluctuations.. They determine the ratio of the radial flux calculated self consistently to that calculated from a quasilinear transport theory to be :

$$\frac{\Gamma_{v_{\parallel}}}{\Gamma_{QL}} \approx \frac{m_e}{m_i\,\beta} \tag{5.9}$$

The dynamo electric field (contribution from the radial flux of field aligned current) is calculated from :

$$\eta J_{\parallel} - \frac{1}{r}\frac{\partial}{\partial r}\left(r\frac{m_e}{|e|}\Gamma_{v_{\parallel}}\right) = E_{v_{\parallel}} \tag{5.10}$$

Since β in RFP's is approximately 10 %, equation (5.9) implies that collisionless

transport of field aligned current probably is not large enough to sustain the reversed magnetic field in RFP's. As for the fast electrons observed in RFP's, Terry and Diamond claim that they are not resonant with intrinsic normal modes (their velocity is larger than the phase velocity of the mode) and therefore do not contribute to the magnetic field line stochasticity. MHD turbulence is thought to be the origin of the stochastic fields which allow the " test particles " to be transported radially outwards in an RFP.

References for chapter 5.

1. J. Larmor, " *How could a rotating body such as the sun become magnetic ?.* " Rep. Brit. Assoc. Adv. Sci. 159 - 160 (1919).

2. T. G. Cowling, " *Magnetic fields of sunspots* ", Mon. Not. R. Astron. Soc. 94, 39 -48 (1934).

3. M. Steenbeck, F. Krause, K. H. Radler, " *Berechnung der mittlerer Lorentz - Field Starke* $v \times B$ *fur ein elektrisch leitendes medium inturbulenter, durch Coriolis - Krafte beeinflusster Beweguung,*" Z. Naturforsch. 21, 369 - 376 (1966).

4. H. P. Furth, J. Killen and M. N. Rosenbluth, Phys. Fluids, **6** (4), 459-84. 193 (1963)

5. H. K. Moffat, " *Magnetic generation in electrically conducting fluids* ", Univ. Press, Cambridge (1978).

5. E. J. Caramana, R. A. Nebel and D. D. Schnack, " *Nonlinear single - helicity magnetic reconnection in the reversed field pinch* " , Phys. Fluids 26 (5), May 1983.

7. J. B. Taylor, " *Relaxation and magnetic reconnection in plasmas* ", Reviews of Modern Physics, Vol 58, No. 3 July 1986.

8. D. D. Schnack, E. J. Caramana and R. A. Nebel, " *Three dimensional magnetohydrodynamic studies of the reversed field pinch* ". Phys. Fluids 28 (1), January 1985.

9. R. A. Nebel, E. J. Caramana and D. D. Schnack, " *The role of the m = 0 modal components in the reversed field pinch dynamo effect in the single fluid magnetohydrodynamics model.* " Phys. Fluids B 1 (8), August 1989.

10. J. A. Holmes, B. A. Carreras, T. C. Hender, H. R. Hicks, V. E. Lynch, Z. G. An and P. H. Diamond, " *Nonlinear interaction of tearing modes : A comparison between the tokamak and the reversed field pinch configurations.* Phys. Fluids 28 (1), January 1985.

11. K. Kusano, T. Sato, submitted to Nuclear Fusion.

12. A. R. Jacobson and R. W. Moses, Physics Rev. Lett. 52, 2041 (1984).

13. P. W. Terry and P. H. Diamond, " *A self - consistent theory of field aligned current by microturbulence.* " Phys. Fluids B 2 1128 (1990).

Chapter 6

Manifestations of the MHD Dynamo through Soft X-Rays.

Introduction

The generation and sustainment of the reversed field for a length of time much longer than the resistive diffusion time has been observed in RFP's[1-2]. The primary goal of this chapter is to give some insight into the underlying mechanism that produces the dynamo. The main indicators for flux generation were the toroidal field at the wall measured with fixed magnetic coils and the B_t leg Rogowski loop,and the toroidal flux measured with a loop surrounding the plasma. Soft x-ray reconstructions obtained during the sustainment phase were used to locate the position of the reconnection of the magnetic flux surfaces, thus indicating the poloidal mode number of the mode responsible. The toroidal mode numbers were obtained from a set of toroidally separated SBD's.

Some of the measurements presented here appear to be in disagreement with other experiments and theoretical predictions. An effort was made to question some of these results by occasionally pursuing a counterinductive approach. There has been a variety of proposed mechanisms for driving the dynamo. In some cases we were able to vary or even eliminate in an experiment the proposed cause of the dynamo and notice only a small variation in the reversed field produced. This method will be demonstrated for the case of plasma rotation and the fast electron (see chapter 7) contributions to the dynamo. The diversity of some results obtained from various RFP's can be attributed to the differences in aspect ratios, external circuits, plasma wall interactions and magnetic field errors. Also in some instances disagreement can be due to different techniques of analyzing the data and the

intrinsic details of the diagnostic used for the measurement. A relevant example of the latter was presented by esearchers from the tokamak de Varennes[3]. They noticed that the reliability of reconstructions of the emissivity (they implemented a Cormack inversion algorithm) relied on the total number and spacing of the SBD's. When operating with only two arrays of detectors (they have a total of five arrays) many artifacts in the reconstructed images were observed. Having this in mind , results from recent RFP experiments in ZT - 40M, Repute-1, STP - 3M and TPE - 1RM15 will be accompanied with information of the key machine and diagnostic features.

ZT - 40M

The first observation of an internal m=1 oscillation on a RFP was made in ZT - 40M[4-5]. The m=1 nature of the mode was inferred from measuring the relative phases of soft x-ray oscillations from a 1 chord array of 8 SBD detectors. An estimate of the toroidal n number was obtained by measuring the relative phase of 2 toroidally separated SBD's. The data was consistent with a mode having an n of 6, 10, 14 and 18. MHD simulations predict that the dominant n is approximately equal to twice the aspect ratio. Since R/a is 5.7 for ZT-40M the expected toroidal n numbers are 10, 11 and 12. The m=1 was suggested as a possible candidate for the RFP dynamo since it was observed over all operational θ values while the amplitude of the m=0 was measured to decrease for low θ.

In 1987 measurements of asymmetric magnetic flux generation in high θ ($\theta > 1.6$) discharges were reported on ZT-40M[6]. Measurements of the magnetic flux at four different toroidal azimuths revealed that flux was initially produced at one location and subsequently spread out around the torus. The idea proposed by

Nebel was that an m = 0 island, while rotating around the torus, reconnects on itself when its leading edge catches up with its trailing edge. The main conclusion was that the magnetic reconnection of the rotating m=0 island contributes significantly to the RFP dynamo. The m=0 island was thought to originate from the interaction of overlapping m=1 modes and possibly in high β plasmas from resistive interchange instabilities.

Motivated by Jacobson's and Moses's theory[7] of radial transport of current by electrons wandering on stochastic field lines, a set of experiments was initiated on ZT-40M that revealed the existence of a unidirectional flow of electrons along B which carried a large fraction of the plasma current. These electrons find themselves moving in a direction opposite to the externally applied electric field as they cross the reversal surface. It was conjectured that the hot electrons play an important role in generating the reversed toroidal flux. The topic of the contribution of hot electrons to the RFP dynamo is delt with in chapter VII.

Repute-1

Soft x-ray measurements on Repute-1[8] revealed periodic profile peaking of the emissivity during the sustainment phase. They measured the crash time to be "always about" 30 μsec, which corresponds (for their plasma parameters) to about $100\tau_A$, where τ_A is the characteristic Alfven time. The Repute-1 SXR imaging system has 2 chord arrays with 11 and 7 SBD's respectively. The Cormack method was used for reconstructing the emissivity profiles. The evolution of the reconstructed emissivity showed rotation of the plasma core before the crash and an m = 1 distortion during the crash that occasionally was followed by a hollow emissivity profile.

TPE - 1RM15

Coherent sawtooth oscillations in the SXR emission is observed on TPE-1RM15[9] with an m = 0, n = 0 nature over a wide range of the pinch parameter θ and especially at low values of θ ($\theta < 1.55$). This is in contrast to the ZT-40M measurements where large SXR oscillations were observed only at large values of θ.

From the introduction we see that the underlying mechanisms that drive the RFP dynamo have yet to be determined accurately from experiments. Numerical simulations based on the 3D MHD codes performed by various researchers are also in conflict. The role of the m = 0 and m = 1 tearing modes in producing the reversed flux is still an open question. The investigation of the dynamo process through soft x - ray measurements has been until now very limited. ZT -40 had only one array of 8 detectors while Repute's imaging system includes only two arrays with a total of 18 SBD's. One must be careful when interpreting reconstructed emissivity profiles from systems with limited spatial resolution. A comparison[10] between reconstructions made using a maximum entropy method and a Fourier Bessel technique revealed that the hollow profiles occasionally seen with the FB method did not appear on reconstructions produced with the MEM method.

The SXR imaging system on MST includes a 4 chord array of 32 SBD's and offers better resolution than existing imaging systems on other RFP's. Both the MEM and Fourier Bessel methods are employed for unfolding the emissivity profiles. The effect of electrons striking the walls and producing detectable x-rays must be seriously taken into account. Occasionally signals from detectors thought to be viewing "hot spots" on the wall would be omitted from reconstructions. Since the plasma is shifted outwards most of the plasma - wall interactions occur in the outer region, and the affected detectors are usually located on the inner side or MST. SBD

signals thought to contain a contribution from wall x-rays show large spikes superimposed on the bulk plasma SXR component. The failure to exclude these signals leads to reconstructions that may show various artifacts. Good spatial resolution permitted the determination of the radial extent of the m=1 helix , the radial location of a propagating disturbance and the identification of an inversion radius.

The important physics issues that will be addressed in this chapter will now be outlined:

1. Measurements of the toroidal mode number n and the phase velocity of propagation of these modes in the toroidal direction have been performed. Emissivity reconstructions during the diffusion phase will be presented that clearly display the rotation of a helix as it passes by the SXR imaging system.

2. Mode analysis of the reconstructed emissivity indicates the existence of a localized disturbance at about 0.5α,where α is the minor radius, propagating in the ion diamagnetic drift direction. This phenomenon is also observed on the magnetic signals and is thought to be due to the phase locking of tearing modes of different helicities. The contribution of this propagating disturbance to the dynamo will be discussed.

3. Generation of reversed magnetic field is observed to occur during the diffusion and MHD relaxation phase. Two distinct rates of flux generation are observed. Reconnection of emissivity surfaces as seen in reconstructions occur near the predicted resonant surfaces of the n = - 5, - 6, - 7 tearing modes.

4. The frequency of toroidal rotation of the excited modes usually increases throughout the discharge. Occasionally, however, an interesting phenomenon occurs where a sudden locking of the modes takes place . This is observed on the SXR reconstructions and the magnetic signals. The cause is still uncertain, and possible candidates are magnetic field errors and plasma wall interaction. SXR mode analysis is presented during a transition from a rotating to a locked plasma. The contribution of plasma rotation to magnetic flux generation will be discussed.

5. A set of experiments was performed in order to test some of the predictions obtained from 3D MHD simulations . By varying the plasma density we were able to scale the diffusion and MHD relaxation times with the magnetic Reynolds number. The results are compared to theory.

6.1 Measurement of the poloidal m and toroidal n numbers of tearing modes on MST.

Mode number measurements have been performed on MST using both insertable magnetic sensors and SXR detectors. A set of four toroidally separated central chord SBD's located at 300°, 320°, 330° and 345°and with a poloidal angle of 15° , were used to determine the n number (see figure 6.1). The m=1 modes manifest themselves on the soft x-rays as small oscillations of frequencies ranging between 10 kHz to 40 kHz. These are occasionally referred to as precursors since they occur before a sawtooth crash. In figure 6.2 I show the the phase shift between soft x-ray precursors measured from SBD's located at different toroidal angles. By cross correlating detectors at 300° and 330° I obtain a 2π phase shift. At first one might conclude that the toroidal mode number is 360°/30° = 12. However due to the double

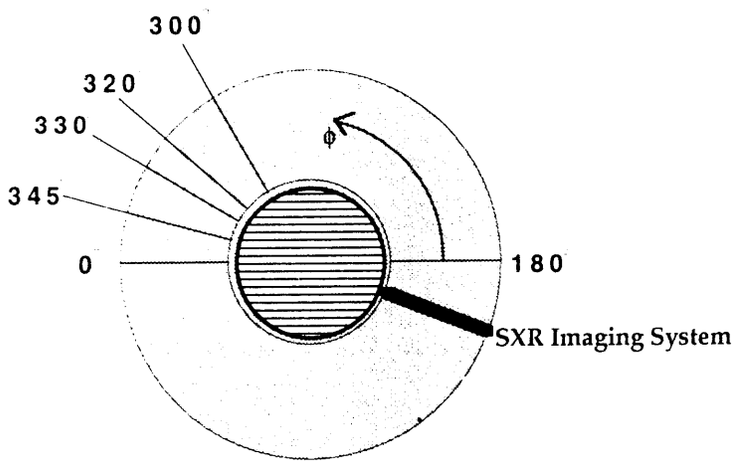

Figure 6.1. *Four toroidally seperated SBD's were used to measure the internal mode number n.*

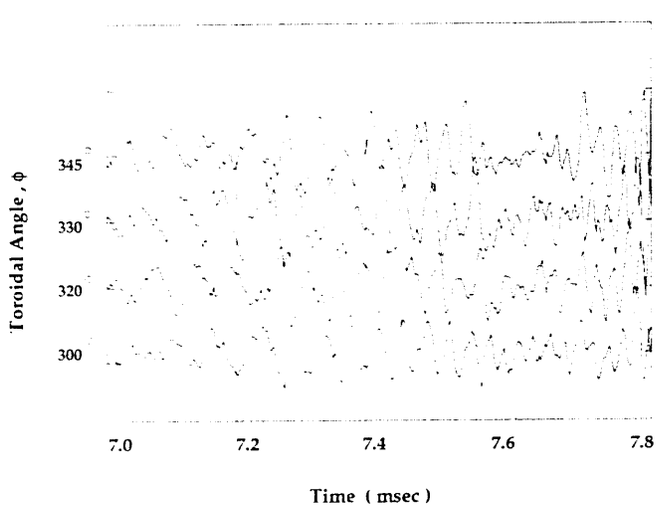

Figure 6.2. *Oscillations superimposed on the SXR signals due to the m=1 tearing modes (precursors), exhibit a phase shift when viewed from toroidally separated SBD's.*

frequency of the m=1 oscillations observed on chords of small impact parameter it turns out that n=6. The reason for the frequency doubling is made clear in figure 6.3. The double frequency effect can be seen in figure 6.4 where we notice that detector sxr-8 which has a impact parameter of 5.5 cm exhibits precursors of frequency twice that of detector sxr-10 which has an impact parameter of 15.7 cm. These observations provide a determination of the radial extent of the m=1 helix to an accuracy of 5 cm. The phase velocity of the m=1 mode is $v = \omega/k$, where $\bar{k} = \frac{m}{r}\hat{\theta} + \frac{n}{R}\hat{\varphi}$, m, n are the poloidal and toroidal mode numbers, r is the minor radius and R the major radius. For the range of measured precursor frequencies,10 kHz to 40 kHz, the phase velocity of the m=1 modes lies between 1.5×10^6 cm/sec and $6.\times10^6$ cm/sec. This is comparable to the diamagnetic drift velocity $v_d \approx \frac{T\ (eV)}{B\ (Tesla)}\frac{1}{\Lambda}$, where Λ the density scale length. In figure 6.5 the rotation of the m=1 helical mode is observed through SXR reconstructions. The center of the helix is slightly shifted outwards as expected from the Grad-Shafranov equation.

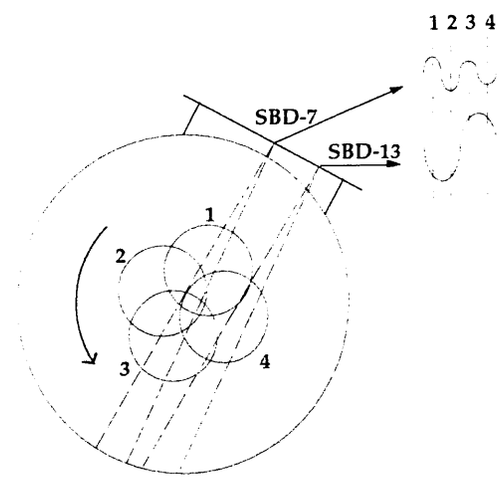

Figure 6.3 *Precursor oscillations on central chord SBD's have twice the frequency of those on edge chord SBD's.*

The measured toroidal n number of 6 is in agreement with that predicted by Martin and Taylor[11]. They show that the mixed solution of the equation $\bar{\nabla} \times \bar{B} = \lambda\ \bar{B}$

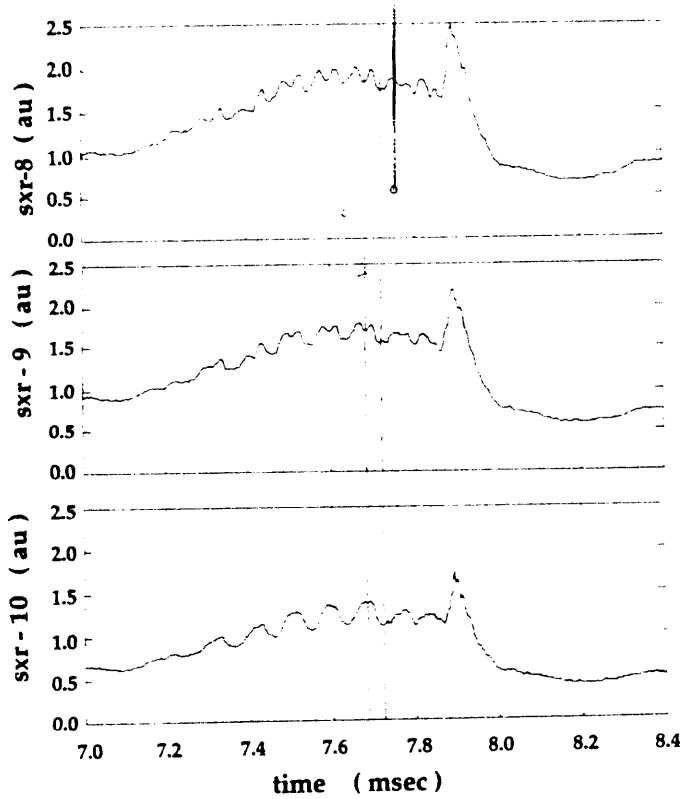

Figure 6.4. *The "double frequency" effect on m=1 precursors .*

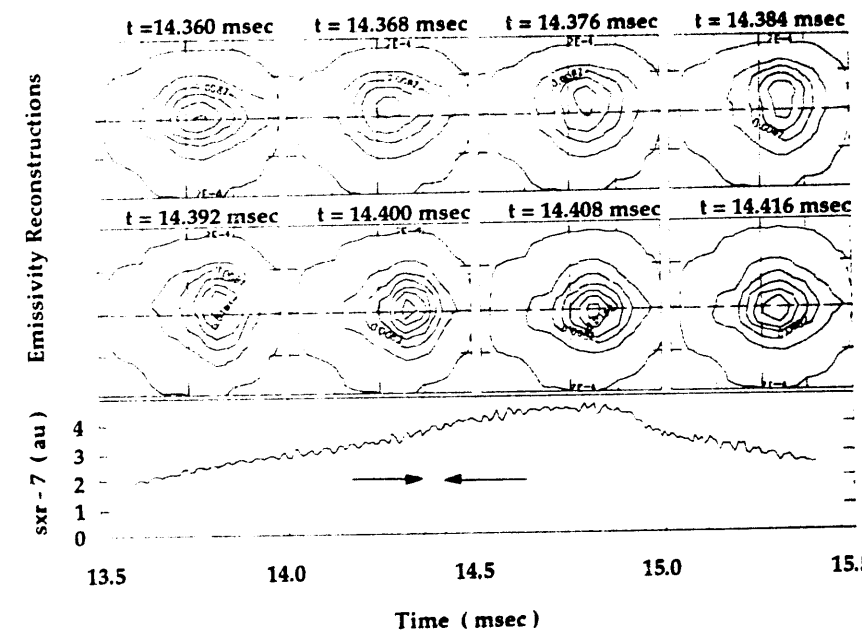

Figure 6.5. *Soft x-ray emissivity reconstructions show the rotation of the m=1 modes.*

requires the condition ka ≈ 1.25 .

6.2 Mode Analysis of Soft X-Ray Emissivity.

It is often useful to study the contribution and evolution of distinct modes of the soft x-ray emissivity profiles obtained from tomographic reconstruction techniques. One reason for performing a mode decomposition of the emissivity profile is that it makes it simpler to distinguish the contribution from modes of low amplitude. The method used for mode analysis is a combination of a maximum entropy method and a Fourier-Bessel expansion technique. We begin by unfolding the measured projections from the 32 soft x-ray chord array using the maximum entropy method.This provides the emissivity in various cells over a plasma cross section The number, size and shape of the cells are chosen after considering the spatial arrangement and collimation of the soft x-ray detectors. The next step is to create a 2D spline function Emis(ρ,θ,t) in polar coordinates. The emissivity Emis(ρ,θ,t) is then expanded in Fourier Bessel functions:

$$E_{mis}(\rho,\theta)=\sum_{m=0}^{\infty}\sum_{n=1}^{\infty} J_m(a_{mn}\frac{\rho}{a})\times(a_{mn}\sin m\,\theta + b_{mn}\cos m\,\theta)$$

$$where:\ \begin{matrix} a_{mn} \\ b_{mn} \end{matrix} = 2.\times[\pi\, a^2\, J_{m+1}^2(a_{mn})]^{-1}$$

$$\times\int_0^{2\pi}\int_0^{a} E_{mn}(\rho,\theta)J_m(a_{mn}\frac{\rho}{a})\begin{Bmatrix}\sin m\,\theta \\ \cos m\,\theta\end{Bmatrix}\rho\, d\rho\, d\theta$$

The amplitute of the mode is :

$$c_m(\rho)=\sqrt{a_m^2(\rho)+b_m^2(\rho)}=\sum_n c_{nm}J_n\left(\frac{\rho\, a_{nm}}{a}\right)$$

The mode amplitude is normalized to the average emissivity :

$$\langle E_{mis}(\rho,\theta)\rangle = \frac{\int_0^{2\pi}\int_0^{R} E_{mis}(\rho,\theta)\rho\, d\rho\, d\theta}{\int_0^{2p}\int_0^{R}\rho\, d\rho\, d\theta} = \frac{2.\times\sum_n\int_0^{R} J_0\left(a_{0,n}\frac{\rho}{R}\right)c_{0,n}\rho\, d\rho}{R^2}$$

Application : A study of the phase locking between resistive tearing modes.

An interesting phenomenon can be observed by looking at the soft x-ray signals of different impact parameters , (figure 6.6).An inversion of the emissivity is clearly seen on the signal SXR-1, placing the inversion radius around r=.6a where a is the minor radius . A modulation of the SXR signal is clearly identified on detector SXR-2 which has an impact parameter of 25 cm. This wave modulation is localized and less present as we move away from SXR-2. The same phenomenon is observed on the other SXR boxports with a slight phase shift .The modulation , as measured from different boxports, occurs at a slightly different radius. This can be explained due to the observed outward shift of the plasma column. The presence of the "SXR beating" is not easily distinguished in the reconstructed emissivity profiles since it is a localized disturbance of small amplitude compared to the central emissivity. We apply the mode analysis technique described above to a time window of the discharge where the slinky was observed in both SXR and edge magnetic signals (see fig. 6.7). Mode analysis of edge magnetic signals[16] have identified the phase locking of resistive tearing modes. I will refer to the" SXR beating" from now on as phase locking since it is the same phenomenon as seen on the magnetics. We calculate the

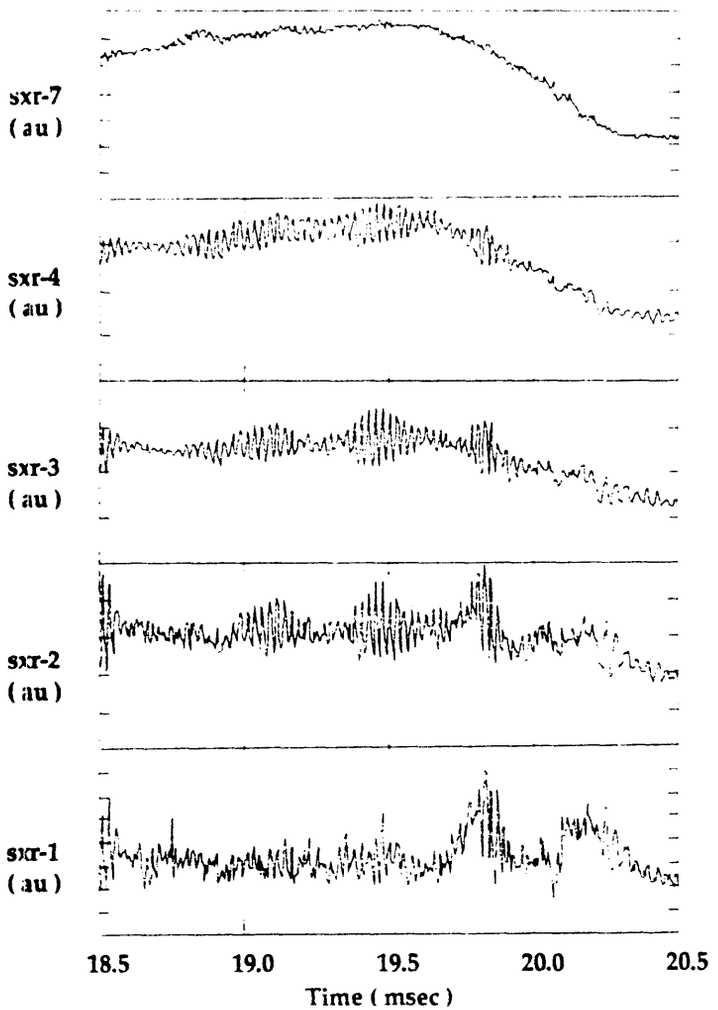

Figure 6.6 *The effect of " SXR beating " is noticeable on the soft x-ray signals. The modulation of the m=1 oscillations during the diffusion and relaxation phase is localized at a radius that corresponds to the impact parameter of detector sxr-2, which is 25 cm from the geometric center.*

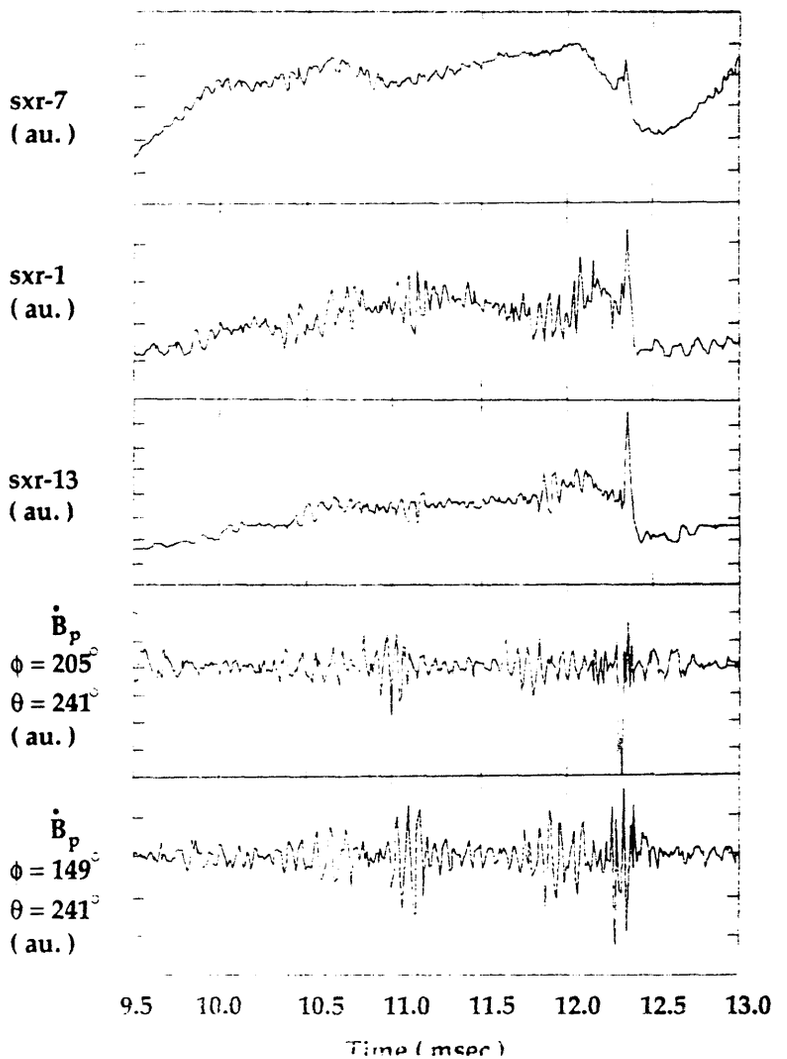

Figure 6.7 *Evidence that the SXR beating is due to the phase locking of resistive tearing modes as determined from analysis of magnetic signals of different toroidal location.*

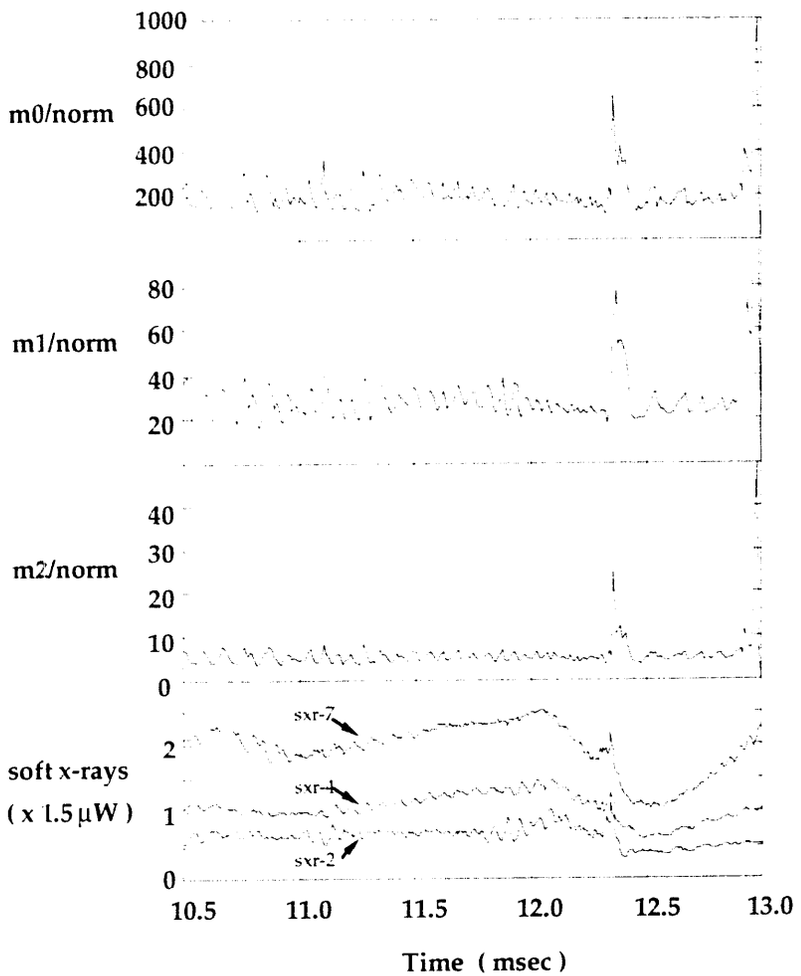

Figure 6.8. *Normalized amplitudes of the m'th component of the emissivity at a radius r=.1a (a is the minor radius). No evidence of phase locking at this radius but soft x-ray signals of different impact parameter show a modulation of the m=1 oscillations at about r=.5a .*

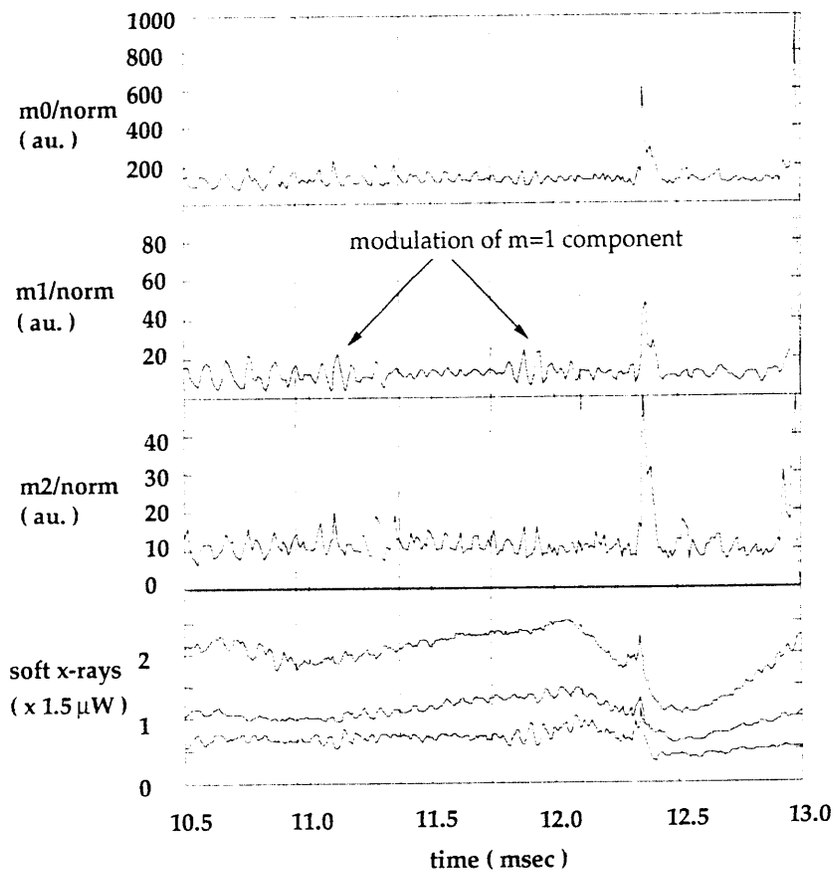

Figure 6.9. *Normalized amplitudes of the m 'th componnent of the emissivity at a radius .5a (a is the minor radius). The m=1 component of the emissivity shows evidence of phase locking of the m=1 resistive tearing modes at approximately the same radius as the raw soft x-ray signals.*

normalized amplitude of the m=1 component of the emissivity at two different radii. At a radius of 10cm from the geometric center we notice, fig. 6.8, oscillations which are due to the plasma rotation and the plasma shift. A large increase during the relaxation phase is also obvious. However there is no evidence of a slinky. In fig. 6.9 we now plot the same quantity at a radius of 30 cm. The presence of the slinky is clear and corresponds approximately to the same radius as seen by the edge SXR detectors. The slinky is thought to be caused by the phase locking of various modes that are pitch resonant in the plasma interior. The narrower the slinky the more modes of different helicity contribute to the phase locking. The properties of the slinky observed in MST appear to be different than those of a toroidally localized disturbance discovered in the thin resistive shell OHTE[12] device. The appearance of the slinky mode in OHTE coincided with the "turning-off" of the internal resonant m=-1 modes. This was thought to be due to the flattening of the $\mu = \vec{J} \cdot \vec{B} / \vec{B} \cdot \vec{B}$ profile caused by the magnetic field line mixing introduced by the slinky. In MST the internal modes n=-5,-6,-7 are not turned off with the appearance of the "slinky mode" which appears from soft x-ray and magnetic signals to be always present in rotating discharges.

6.3 Generation of reversed magnetic flux during the diffusion and relaxation phase.

The production of reversed magnetic flux is seen to occur during the diffusion and relaxation phase. This is shown in figure 6.10 where B_t (a) exhibits a slow increase during the rise of the sawtooth and a more sudden increase during the crash. One can picture a competition between resistive decay and flux generation. Early in the sustainment phase , flux generation is evident during the diffusion

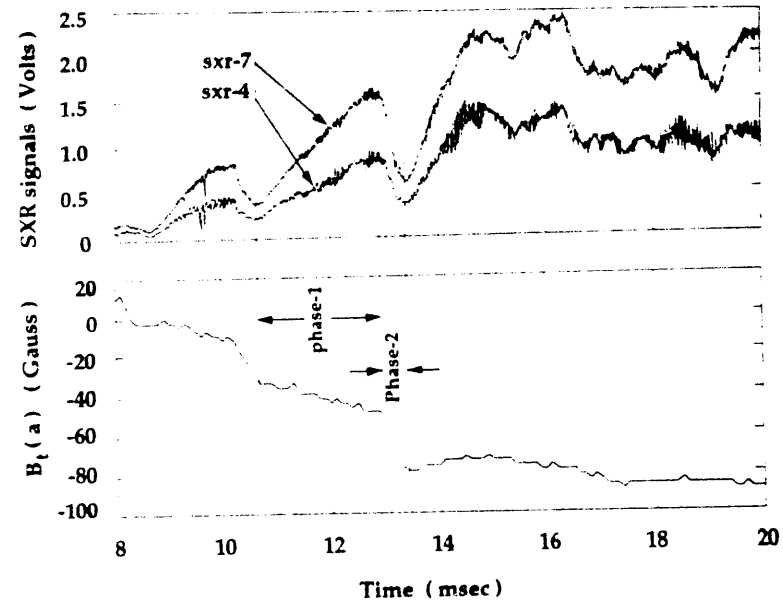

Figure 6.10. *Toroidal flux generation is observed during the MHD relaxation phase (phase-2) and the diffusion phase (phase-1).*

phase while during peak current, diffusion dominates and B_t (a) decays after a large sawtooth crash. Tearing modes with m = 1, n = 5, 6, 7 manifest themselves as 10 - 40 kHz oscillations in the soft x - rays during the diffusion phase. The amplitude of these oscillations is much larger on chords whose impact parameters lie close to the resonant surfaces of the resistive tearing modes. In chapter 7 we show that the hot electron contribution to the dynamo in this phase must be small. Since the magnetic plasma energy is departing from the minimum energy during diffusion the plasma excess energy is growing, and according to Kusano's 3D MHD simulations[13] the m = 1 contribution to the dynamo should dominate. Simulations by Nebel et. al.[14] on

the other hand show that the dynamo is always dominantly m = 1 driven. It appears that at least for the diffusion phase both experiment and theory agree to a dynamo driven by the m = 1 tearing modes. The slow rate of magnetic flux generation during the diffusion phase can be explained as follows. The m=1 modes are still small in amplitude, and magnetic reconnection of the helix is basically due to the diffusion of the magnetic field lines. The amount of flux generated throughout the diffusion phase is small since the fluctuations $\tilde{B}$ are at a low level, see figure 6.11. In figure 6.12 we show the evolution of the amplitude corresponding to the m = 0 and m = 1 Fourier Bessel component of the emissivity during the diffusion phase. All mode calculations are made with the origin of the coordinate system located at the geometric center of MST. The oscillations of the m = 1 amplitude is due to the rotation of the plasma around a point that does not lie on the geometric axis. The DC component of the m = 1 amplitude is observed to grow slightly before the sawtooth crash. The radial profile of the m=1 Fourier -Bessel component of the emissivity during a precursor oscillation is shown in figure 6.13. The maximum of each curve in fig. 6.13 does not peak at the same radius since the axis of the helix is slightly shifted off the geometric axis.

When the amplitudes of the m=1 tearing modes reach a certain threshold, nonlinear reconnection is initiated and a sudden increase in generated magnetic flux is expected due to the forced reconnection. The nonlinear coupling of magnetic signals, measured from the edge fixed array, is identified with the use of bispectral analysis[15]. The results imply nonlinear coupling of the m=1 and dominantly n=5,6,7 modes during the MHD relaxation phase. In figure 6.14 notice that the SXR emissivity surfaces appear to become very distorted during the MHD relaxation phase near the predicted resonant surfaces of the m=1, n=5,6,7 resistive tearing

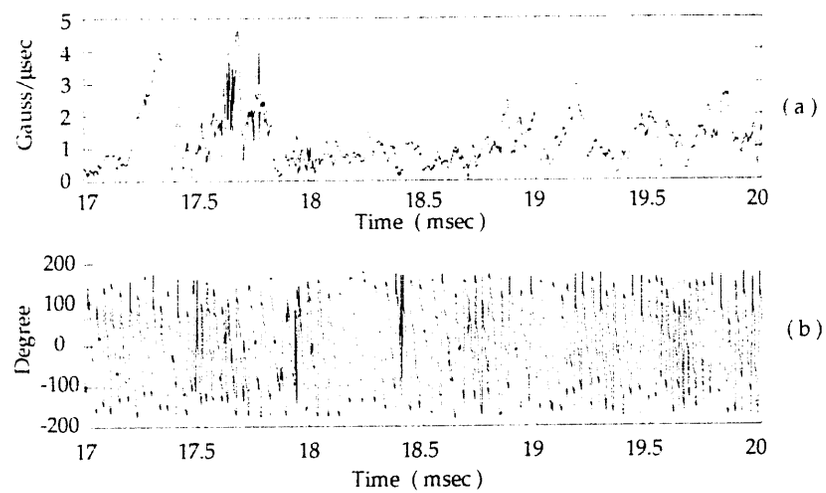

Figure 6.11. a) *The amplitude of the m=1 component of* $\dot{\mathbf{B}}_p$ *increases gradually during the diffusion phase : 17.8 to 19.8 msec. b) The almost constant phase velocity allows us to consider* $\mathbf{B}_p \approx \frac{\dot{\mathbf{B}}_p}{\omega}$ *. (The data were provided by Assadi*[15] *).*

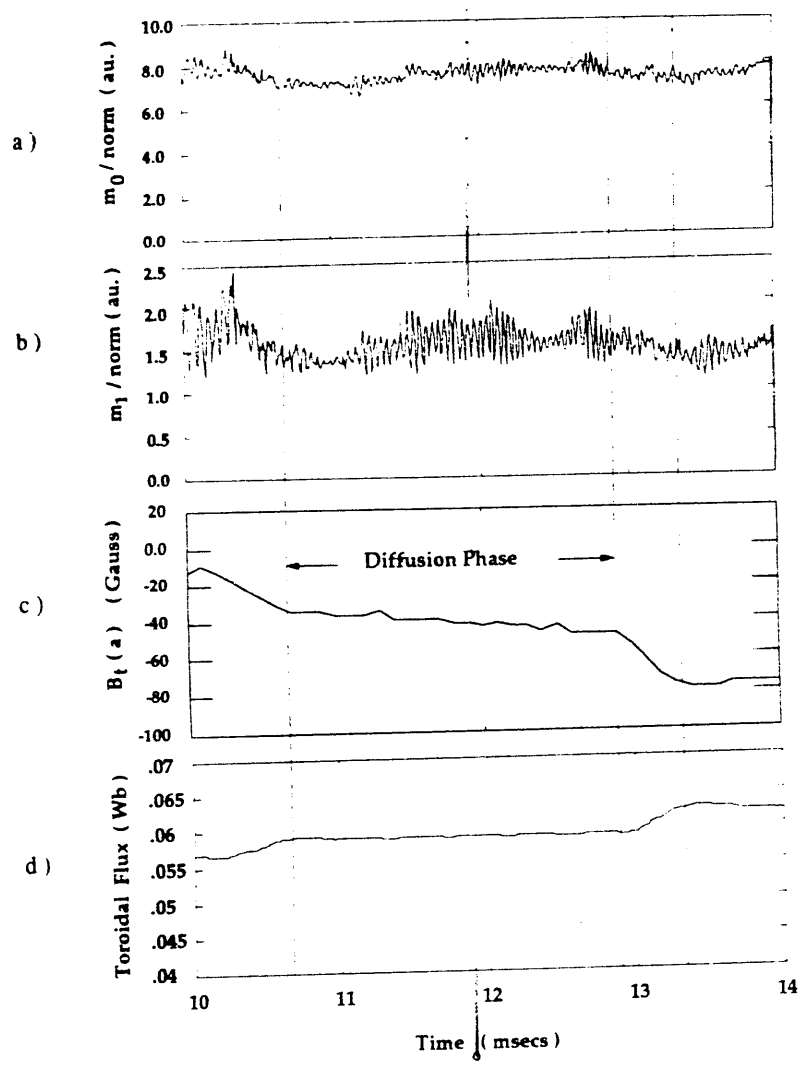

Figure 6.12 *a).b) The m=0 and m=1 Fourier Bessel components of the SXR emissivity . c). d) The steady increase of the toroidal field at the wall and the non decaying toroidal flux indicate that a dynamo process is also present during the diffusion phase.*

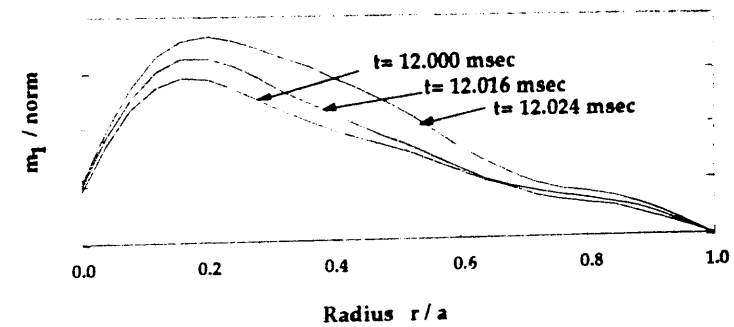

Figure 6.13. *The radial profile of the m=1 component of the SXR emissivity during a precursor oscillation.*

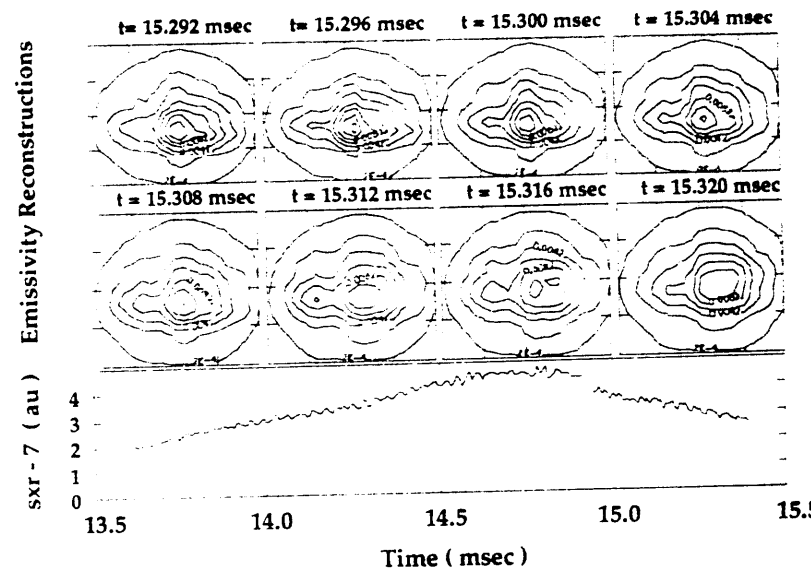

Figure 6.14. *SXR reconstructions show the formation of an m=1 island during a sawtooth crash.*

modes.

6.4 Emissivity mode analysis of locked plasmas.

Often discharges of shorter duration are observed on MST (fig. 6.15) . Magnetic mode analysis[16] of these discharges reveals a growing m=1 component of the radial field at the poloidal gap coincident with the locking of the m=1 tearing modes. SXR emissivity reconstructions also show the non rotation of the m=1 helix for locked plasmas. It is still unclear from the magnetics whether the m=0 modes are

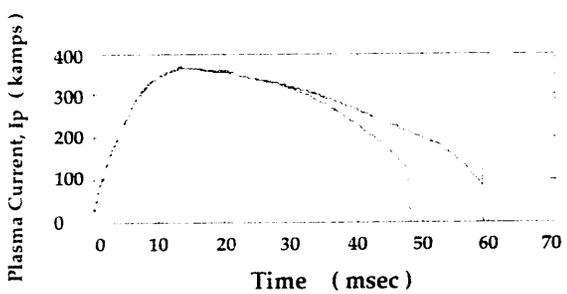

Figure 6.15. *Plasma current for a locked (short) and non-locked (long) discharge.* also locked.

Mode analysis of emissivity reconstructions during the transition between a rotating and a non rotating plasma often reveals a decrease in the m=1 emissivity amplitude, figure 6.16 . This is also observed on the edge magnetic coils. At first one is lead to believe that this occurs due to an inward shift of the plasma core towards the geometric center of the MST. However the emissivity reconstructions do not show any shift but rather a flatter emissivity profile (figure 6.17). During the "locked mode", reversed field generation is still present, and emissivity reconstruc-

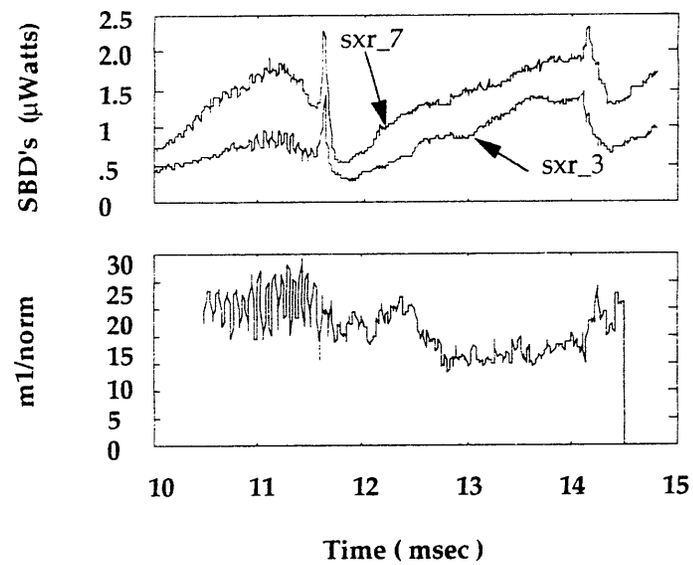

Figure 6.16 *The normalized m=1 amplitude of the SXR emissivity decreases during a non-locked to locked transition.*

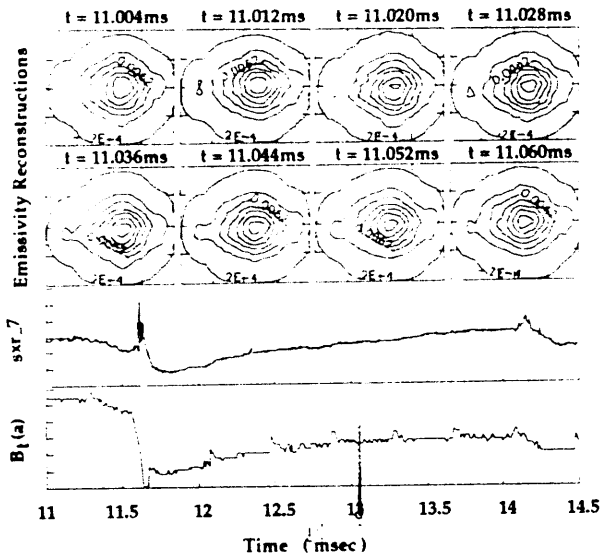

Figure 6.17a *SXR emissivity reconstructions for a non-locked discharge.*

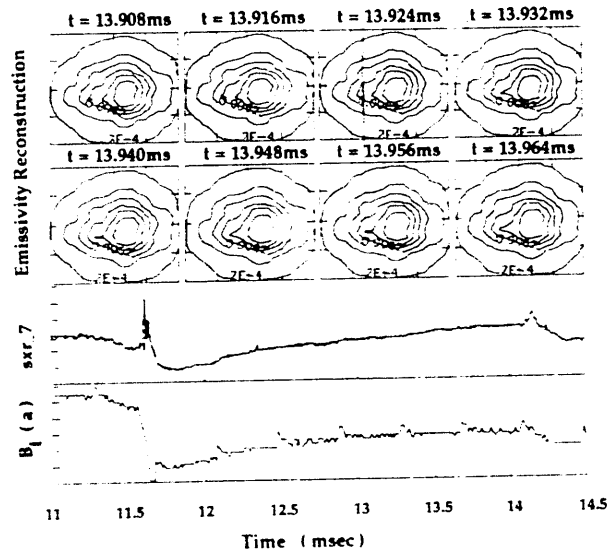

Figure 6.17b. *SXR emissivity reconstructions for a locked discharge.*

tions still show reconnection of emissivity surfaces , indicating that the rotation of the m=1 modes does not play a crucial role in producing reversed magnetic field. The mechanism that produces the locking of the plasma is still unknown. The ratio of the number of locked to non-locked discharges however has been affected by magnetic field error corrections, impurity doping and gas puff levels.

Another interesting feature of non-rotating plasmas is that they appear to have less excess energy. This is shown in figure 6.18 where the non rotating shots reside closer to the BFM curve. According to Kusano's recent numerical simula-

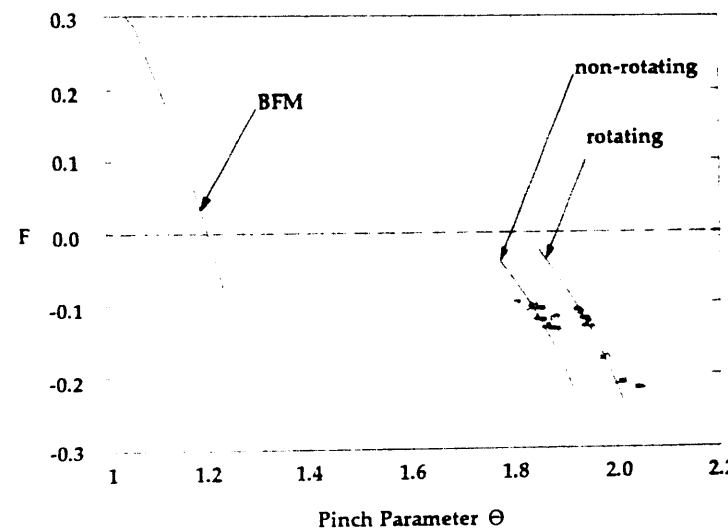

Figure 6.18 *F - θ trajectories for locked and non - locked plasmas during the time interval 25 to 26 msecs into the discharge.*

tions[12] the contribution of tearing modes of different poloidal m number to the dynamo electric field depends on how far the plasma energy is from the minimum energy state. He predicts that for excess energies below 8% the dynamo produced by the reconnection of the m=0 modes is larger than that of the m=1 modes. One would expect then to measure a larger m=0 contribution for nonrotating plasmas. I have not been able to observe this difference from comparing emissivity reconstructions from both nonrotating and rotating plasmas. However it is possible that the excess energy difference between the two cases is not large enough to be detected with the present spatial resolution of the SXR imaging system.

6.5 Scaling of the magnetic Reynolds number with the MHD relaxation and diffusion time of a sawtooth event.

A large number of 3D nonlinear MHD simulations have recently been performed in order to explain the observed magnetic reconnection in RFP's. Some of these codes have been able to simulate the sawtoothing event and produce reversal from the nonlinear coupling between tearing modes of different helicity. The magnetic Reynolds numbers S used in most of these codes lies between 10^3 and 10^4 while in RFP's S is usually in the range of 10^5 to 10^6. Also most of the simulations do not include transport. Having this in mind we will present a comparison between simulation and experiment of the measured scaling of the diffusion and MHD relaxation time with the magnetic Reynolds number during a sawtooth event.

In order to understand the importance of the Reynolds number in characterizing a flow we will derive S for a fluid and then for a magnetofluid. In fluid dynamics the turbulent Reynolds number is defined as the ratio of the inertial term

to the damping term of the Navier-Stokes equation.

$$\rho \frac{d\vec{v}}{dt} - \mu \nabla^2 \vec{v} + \vec{\nabla} p = \vec{F} \qquad (6.1)$$

where ρ is the mass density and μ is the coeficient of shear viscosity. The type of flow depends on the ratio :

$$R = \frac{\rho \frac{d\vec{v}}{dt}}{\mu \nabla^2 \vec{v}} \approx \frac{\rho}{\mu} v_c a_c$$

where a_c is a characteristic length of the flow and v_c is a typical velocity. For $R < 10^3$ the flow is laminar while for $R > 10^4$ the flow is turbulent.

In magnetohydrodynamics we can obtain a similar relation from the induction equation 5.1 .

$$S = \frac{\frac{\vec{B}}{\rho} \cdot \vec{\nabla} \vec{v}}{\left| \nabla^2 B / \mu_0 \sigma \right|} \approx \frac{\mu_0 v_c a_c}{\eta} \qquad (6.2)$$

where η is the resistivity. For the characteristic scale length a_c I used the minor radius of MST. Some authors prefer using the distance between the wall and the reversal surface. The characteristic velocity is the Alfven velocity v_A defined as:

$$v_A = \frac{B}{(\mu_0 \rho)^{1/2}} \qquad (6.3)$$

Two forms of the resistivity were considered in calculating the magnetic Reynolds number S :

a) First I chose to calculate S from the Ohmic resistivity. In this case the resistivity is thought to contain an anomalous component in addition to the Spitzer (classical) part :

$$\eta_{Ohmic} = \eta_{Spitzer} + \eta_{anomalous}$$

The equations used for determining S_{ohmic} from measured quantities are :

$$S_{Ohmic} = \frac{\tau_R}{\tau_A} \qquad (6.4)$$

$$\tau_R = \frac{\mu_0 a^2}{\eta_{Ohmic}} \qquad (6.5)$$

$$\tau_A = a\,(\mu_0 \rho)^{1/2} B^{-1} \approx .14\, a\, n_{e,19}^{1/2} B^{-1}\ (\mu sec) \qquad (6.6)$$

$$\eta_{Ohmic} = \frac{V_{loop}\, a^2}{I_p\, 2R \times 10^3} \frac{\left[5\times\left(10+\theta^2\right)\right]}{\left[11\times\left(5+6\theta^2\right)\right]} \qquad (6.7)$$

where $\frac{\left[5\times\left(10+\theta^2\right)\right]}{\left[11\times\left(5+6\theta^2\right)\right]}$ is the "screw-up" factor calculated from the PFM model[17]. In figure 6.19 I show the evolution of S_{Ohmic} during a typical discharge. The magnetic Reynolds number decreases during the relaxation phase but it has an overall increasing trend up to approximately 25 msec into the discharge.

$$Z^* = \frac{\eta_{OHMIC}}{\eta_{Spitzer}(Z_{eff}=2)}$$

$$S_{OHMIC} = \frac{\mu_0 a^2}{\eta_{OHMIC}\,\tau_A}$$

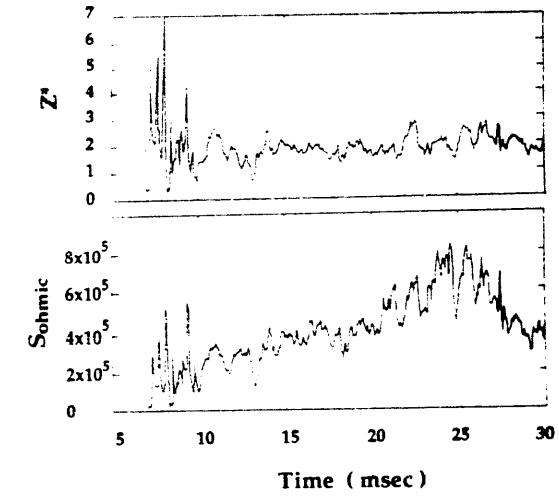

Figure 6.19 *Z* and the magnetic Reynolds number S_{OHMIC}. The normalized hot electron temperature was used in determining $\eta_{Spitzer}$.*

Most of the data for the scaling of the crash time vs S are representative of only a portion of the discharge,approximately between 10 and 25 msec, since this is the interval where large "jumps" in the toroidal field occur. After the current ramp-up phase, the occurence of a sawtooth is less probable even though the reversed field is still maintained. The MHD relaxation time for the scaling was taken from the measured toroidal magnetic field at the wall . In figure 6.20 I show the variation of the sawtooth crash time normalized to the Alfven time as a function of the magnetic Reynolds number S_{Ohmic}. The scatter in the data can partially be attributed to the fact that some diagnostics do not have a fast enough time response to provide an accurate measurement during the rapid transition phase of the sawtooth crash. The

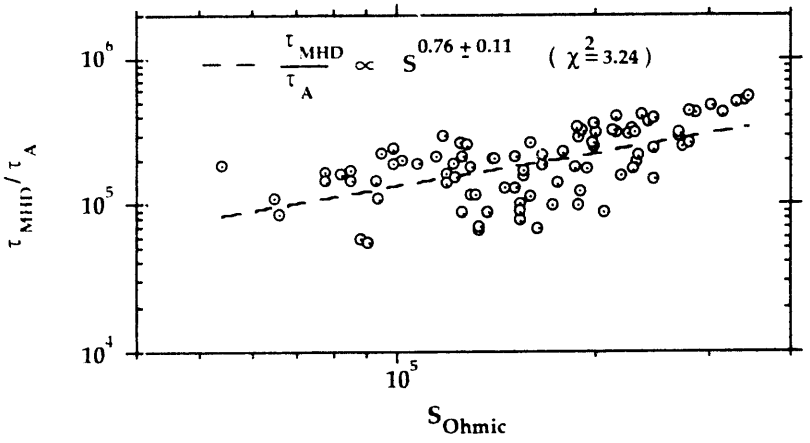

Figure 6.20. *The normalized MHD relaxation time versus* S_{OHMIC}.

error in the plasma density is due to the sensitivity of the CO_2 interferometer to external vibrations. Fortunately the effect of the vibrations becomes significant only after 25 msec into the discharge.

The data of figure 6.20 indicate that the MHD relaxation time scales as $S_{Ohmic}^{0.76 \pm 0.11}$. A similar analysis as described above leads to a scaling of the diffusion time versus the magnetic Reynolds number of $\frac{\tau_{Dif}}{\tau_A} \approx S_{Ohmic}^{0.9 \pm 0.1}$ (figure 6.21). This stronger dependence of the diffusion time on resistivity implies that the reconnection process observed in this phase is strongly related to the diffusion of the magnetic field lines. This would also explain the slow rate of flux produced as seen in figure 6.10. On the other hand the MHD relaxation time depends less on the resistivity, implying a forced reconnection process originating from the nonlinear interaction of the dominant resistive tearing modes.

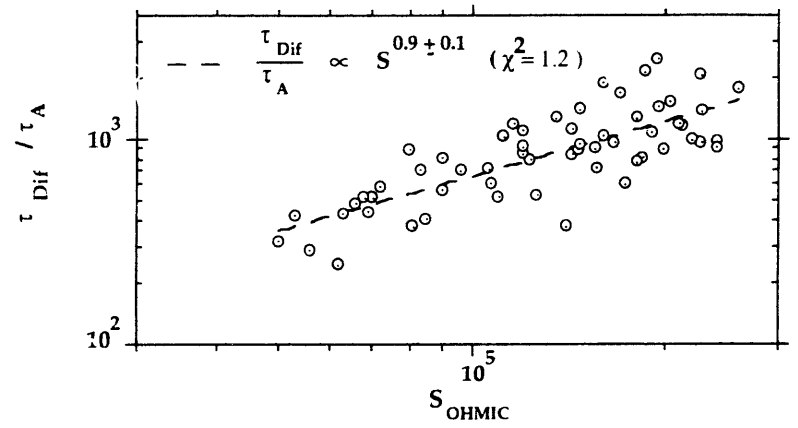

Figure 6.21. *The diffusion time of a sawtooth event versus the magnetic Reynolds number* S_{OHMIC}.

We will now proceed in determining S from the Spitzer resistivity since this is the standard form adopted in 3D resistive MHD simulations. The departure of the Omhic resistivity from Spitzer resistivity can be explained from equation 5.5. The existance of a mean helicity ($\nabla \times \vec{v}$ and $\vec{v}$ are correlated) leads to an Ohm's law of the form :

$$\vec{E} = \eta_{Spitzer}\vec{J} + \left\langle \vec{v} \times \vec{b} \right\rangle = \eta_{Spitzer}\vec{J} + \alpha\vec{B} - \beta\nabla\times\vec{B}$$

or

$$\left(\eta_{Spitzer} - \beta\mu_0 \right)\vec{J} = \vec{E} - \alpha\vec{B}$$

The above equation implies that the anomalous contribution to the resistivity is given by the mean quantity $\beta\mu_0$ which may be determined from the turbulent velocity field. Since the anomalous term may depend on the boundary conditions,

field errors and other machine dependent quantities, which are difficult to determine, the use of a Spitzer resistivity is more appropriate.

b) The Spitzer resistivity including Z_{eff} contributions is given by the equation:

$$\eta_{Spitzer} = 5.2 \times 10^{-5} \frac{Z_{eff} \ln \Lambda}{T_e^{3/2} (eV)} \; ohm\text{-}m \qquad (6.8)$$

The Thomson scattering diagnostic can only provide the central electron temperature at one time point in the disharge, whereas the present calculation requires the average temperature over the MHD relaxation phase. The first approximation made was to use the hot electron temperature $T_{e,h}$ measured from the SXR target probe. $T_{e,h}$ was normalized to take into account the variation of the ratio $T_{e,h}/T_e(0)$ vs plasma density :

$$\frac{T_{e,h}}{T_e(0)} = 2.627 - 1.51 \times 10^{-13} \bar{n}_e \; (cm^{-3})$$

The above equation was determined empirically using SXR target and Thomson scattering $T_e(0)$ data during a density scan described in chapter VII.

The second approximation is that Z_{eff} was taken to be constant. Having made these assumptions I present in figure 6.21 the scaling of the MHD crash time versus $S_{SPITZER}$. The main conclusion is that there appears to be no dependence of the crash time with classical resistivity , ie. $\frac{\tau_{MHD}}{\tau_A} \approx S_{Spitzer}^{0.0 \pm 0.2}$ .This result is in agreement with some theoretical models[16] that predict a *forced reconnection process* during the crash, which would therefore lead to a resistivity-independent scaling. In figure 6.22

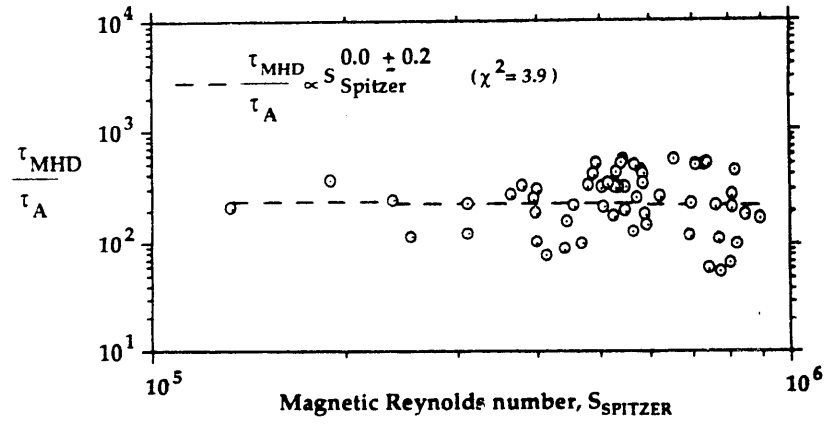

Figure 6.21. *The MHD relaxation time versus the magnetic Reynolds number* $S_{Spitzer}$.

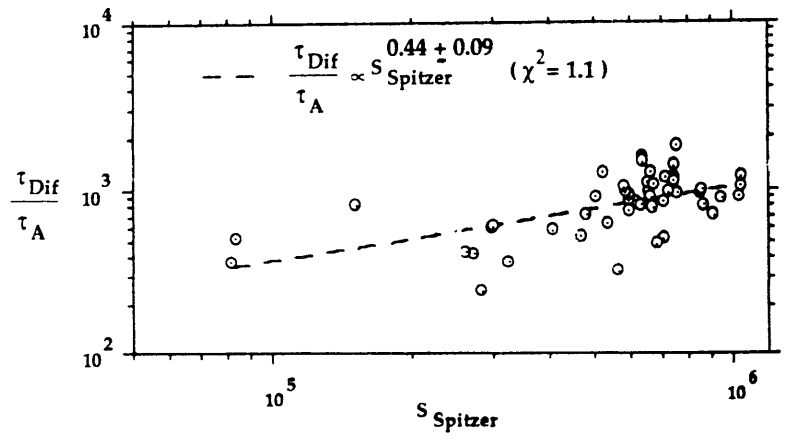

Figure 6.22. *The Diffusion time versus the magnetic Reynolds number* $S_{Spitzer}$.

I present the scaling of the diffusion time versus $S_{SPITZER}$. In this case we obtain : $\frac{\tau_{Dif}}{\tau_A} = S_{Spitzer}^{0.44 \pm .09}$. The data presented in fig. 6.21 and fig. 6.22 suggest that there are two distinct dynamo mechanisms during the RFP sawtooth cycle. The diffusion phase can be described with a classical resistivity dependent dynamo model, such as that presented by Nebel et al.[19-20], while the MHD phase shows no dependence on the classical resistivity, implying that a nonlinear model as presented by Holmes et al.[21] is applicable in this phase.

References for Chapter 6.

1. D. A. Baker, M. D. Bausman, C. J. Buchenauer, L. C. Burkhardt, G. Chandler, J. N. DiMarco, J. N. Downing, P. R. Forman, R. F. Gribble, A. Haberstich, R. B. Howell, J. C. Ingraham, A. R. Jacobson, F. C. Jahoda, K. A. Klare, E. M. Little, L. W. Mann, R. S. Massey, J. Melton, G. Miller, R. Moses, J. A. Phillips, A. E. Schofield, K. F. Schoenberg, K. S. Thomas, R. G. Watt, P. G. Weber, and R. Wilkins, 9th International Conference on Plasma Physics and Controlled Nuclear Fusion Research, IAEA - CN41 Paper H2, Baltimore, Maryland (1982).

2. The ETA - Beta II Team, 9th International Conference on Plasma Physics and Controlled Nuclear Fusion Research, IAEA-CN41 Paper H4,Baltimore, Maryland (1982).

3. C. Janicki, R. Decoste, and C. Simm, " *High-Resolution Soft-X-Ray Tomography of Sawtooth Oscillations on the Tokamak de Varennes.*" , Phys. Rev. Lett. **62**, 3038 (1989).

4. G. A. Wurden, *"Soft x-ray array results on the ZT-40M reversed-field pinch.*", Phys. Fluids **27** (3), March (1984).

5. R. G. Watt and R. A. Nebel, " *Sawteeth, magnetic disturances, and magnetic flux generation in the reversed-field pinch.*", Phys. Fluids **26** (5), May (1983).

6. R. B. Howell, J. C. Ingraham, G. A. Wurden, P. G. Weber, and C. J. Buchenauer, " *Asymmetric magnetic flux generation. m=1 activity, and edge phenomena on a reversed-field pinch.*", Phys. Fluids **30** (6), June (1987).

7. A. R. Jacobson and R. W. Moses, Physics Rev. Lett. 52, 2041 (1984)

8. N. Asakura, Y. Nacayama, S. Shinohara, H. Toyama, K. Miyamoto. " *Soft X-Ray Measurements on the Repute-1 Reversed-Field Pinch.*", Nuclear Fusion, Vol. 29,

No.6 (1989).

9. S. Shiina, " *Soft X-ray Measurements in TPE-1RM15 Reversed-Field Pinch* " , Presented at the US/Japan Workshop on Fluctuations in RFP and ULQ Plasmas, March 12 - 15, (1990) Madison, Wisconsin.

10. L. M. Blush and G. A. Navratil," *Maximum Entropy Tomographic Reconstructions of JET Soft X-ray Emission* " Presented at the APS meeting ,Division of Plasma Physics, Anaheim, CA, Nov. (1989).

11. T. J. Martin and J. B. Taylor, (1974), " *Helically Deformed States in Toroidal Pinches,*" Culham Laboratory report (unpublished).

12. R. J. La Haye, P. S. Lee, M. J. Schaffer, T. Tamano, P. L. Taylor (General Atomics, San Diego, California, USA), " *Magnetic Fluctuation Measurements in the Resistive Shell OHTE Device Operated as a Reversed Field Pinch.*" Nuclear Fusion, Vol. 28, No. 5 (1988).

13. K. Kusano, " *MHD Relaxation, Dynamo, Self Sustainment and Phase Locking in RFP's*" (unpublished).

14. R. A. Nebel, E. J. Caramana and D. D. Schnack, "*The role of the m=0 modal components in the reversed-field-pinch dynamo effect in the single fluid magnetohydrodynamics model*" Phys. Fluids B 1 (8), August (1989).

15. S. Assadi, " Private communication".

16. A. Alamagri, Ph.D. thesis, University of Wisconsin-Madison (1990).

17. J. C. Sprott, Phys. Fluids 31, 2266 (1988).

18. Y. L. Ho and G. G. Graddock, " *Nonlinear Dynamics of the Dynamo and Quasiperiodic Relaxation in RFP's.* " Presented at the US/Japan Workshop on Fluctuations in RFP and ULQ Plasmas, March 12 - 15, (1990) Madison, Wisconsin.

19. E. J. Caramana, R. A. Nebel and D. D. Schnack, " *Nonlinear single - helicity magnetic reconnection in the reversed field pinch* " , Phys. Fluids 26 (5), May 1983.

20. D. D. Schnack, E. J. Caramana and R. A. Nebel, " *Three dimensional magnetohydrodynamic studies of the reversed field pinch* ". Phys. Fluids 28 (1) , January 1985.

21. J. A. Holmes, B. A. Carreras, T. C. Hender, H. R. Hicks, V. E. Lynch, Z. G. An and P. H. Diamond, " *Nonlinear interaction of tearing modes : A comparison between the tokamak and the reversed field pinch configurations.* Phys. Fluids 28 (1), January, (1985).

Chapter 7

Manifestations of the Kinetic Dynamo through Soft X-Ray Measurements

Introduction

The discovery of hot electrons in RFP's has brought forward a new theory to explain the sustainment of the toroidal magnetic field for a period of time much longer than that anticipated from resistive diffusion alone. Originally proposed by Jacobson and Moses[1-2] the theory requires that hot electrons be transported across the magnetic field lines and accelerated by the electric field component parallel to **B**. Many experiments on RFP's have confirmed the existence of energetic electrons at the plasma edge[3-7]. However, since the measured properties vary from one device to the other, we will briefly describe the results obtained from other RFP's and then present in more detail the hot electron measurements on the MST.

ZT-40M

Measurements on ZT-40M using an electrostatic energy analyzer, a calorimeter probe and a double swept Langmuir probe reveal the existence at the plasma edge of a unidirectional flow of electrons along **B** having temperatures lying between 2 and 3 times the central electron temperature. The hot electrons appear to carry a significant fraction of the current density in the direction of **B**. Energetic electron transport modeling[8] based on the drift kinetic equation (DKE) predicts the value of $T_{e,hot}(r)$, $n_{e,hot}(r)$ and $J_{e,hot}(r)$. As seen in experiment, the hot electron temperature is predicted to be a weak function of minor radius. Further measurements performed to determine whether hot electrons would be an important factor in

larger RFP's show that the ratio $\frac{T_{ehot}}{T_e(0)}$ decreases with $\frac{E_0}{E_c}$, where E_c is the critical runaway field, $E_c = \frac{kT_e}{2\,e\,\lambda_0}$ and λ_0 is the mean free path for 90° scattering of a thermal electron. This is encouraging since devices like RFX are expected to have an order of magnitude lower E_0/E_c than ZT-40M.

TPE - 1RM15

After the discovery of the hot electron component in ZT - 40M experiments were performed in the TPE - 1RM15 to see if they could detect hot electrons with similar properties. The main diagnostics used were a Si(Li) detector "looking at" x-rays emitted by various metals inserted at the edge and an infrared camera monitoring the temperature of the graphite movable limiters. Their measurements confirm the preferential heating along **B** of various materials (facing the electron current) inserted near the plasma edge. The temperature obtained from the Si(Li) detector indicate that T_{ehot} is 10 to 20 times higher than the central electron temperature. The reason for such very high electron temperatures is not clear yet, but factors that may contribute would be poor magnetic confinement and large E_0/E_c in the TPE - 1RM15 RFP .

STP - 3M

In STP - 3M, by measuring the soft x-ray spectrum emitted from electrons colliding with the wall, they estimate the hot electron temperature to range between 2 - 8 keV . They speculate that the reason for the observed energetic electrons is the high toroidal electric field in STP - 3M.

7.1 Properties of the edge electrons in MST

In agreement with measurements in ZT - 40M,TPE - 1RM15 and STP - 3M a unidirectional flow of hot electrons was observed with the SXR target probe. Figure 7.1 shows the angular distribution of the SXR target signal as the probe was rotated about its axis.

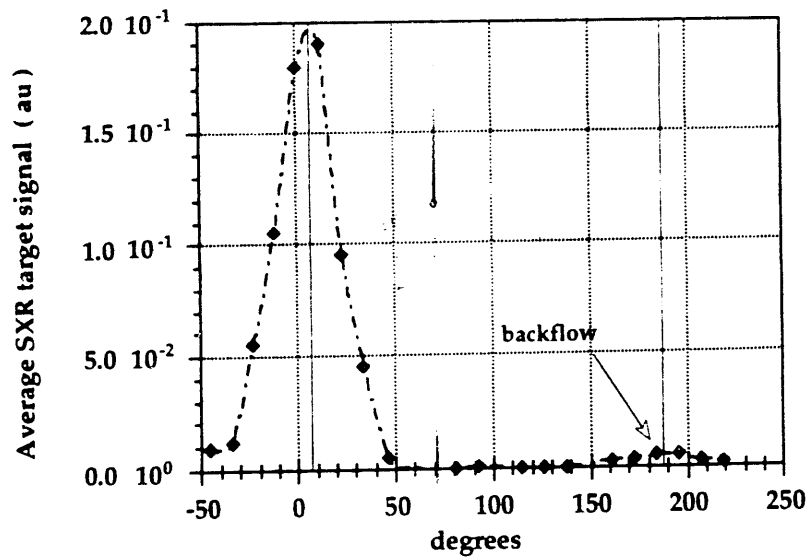

Figure 7.1. *The angular distribution of the SXR target probe signal indicates that the hot electrons are moving unidirectionaly along the magnetic field lines. (0° corresponds to the normal to the target surface being in the poloidal plane.)*

We will show that this peaking of the SXR target signal over a narrow angle cannot be accounted for by any reasonable electron drift velocity. From eq. (4.3) we can calculate the ratio of the SXR target signal for the target facing towards and away from the drift velocity direction for various values of the drift velocity and thermal

velocity of the electrons. In figure 7.2 we consider an edge thermal temperature of 30 eV and a hot electron component of 450 eV. We see that the ratio is much less than that measured experimentally.

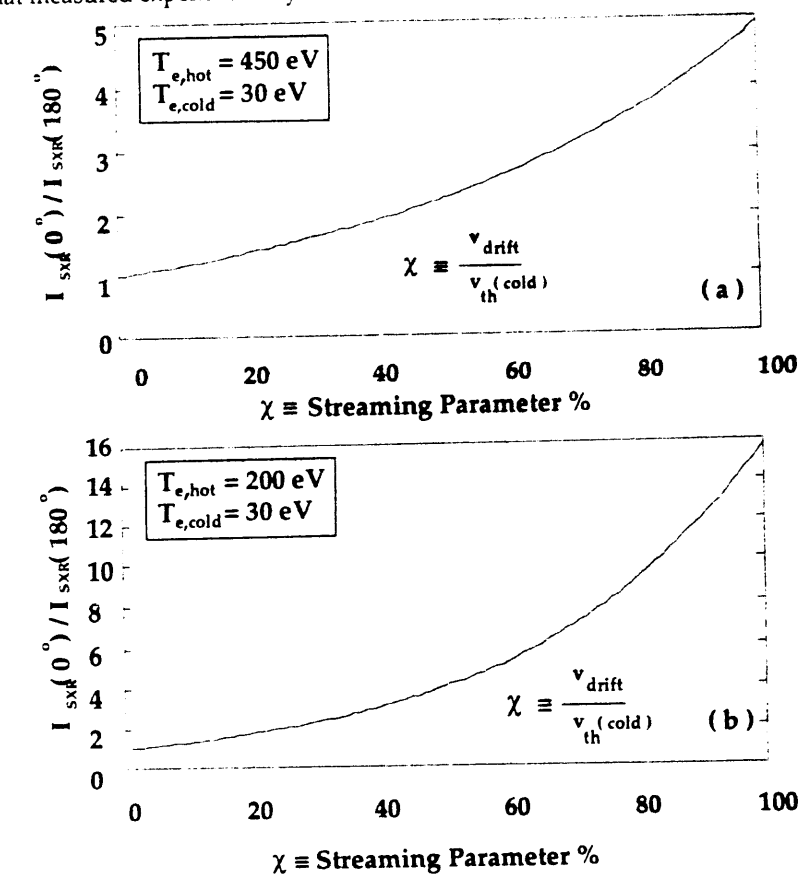

Figure 7.2. *Calculated values for the expected ratio of the SXR target probe signals for the target facing towards and away from the electron drift velocity direction. a) We consider the case of a 450 eV hot component and a 30 eV bulk component. b) For relatively low hot electron temperature the ratio can become large.*

The measured SXR target signals in the backflow direction are less than 1/30 the forward direction. These results indicate that the signal is mostly due to electrons moving preferentially parallel to **B**.

The expected ratio of the electron drift velocity to electron thermal velocity also referred to as the streaming parameter can be estimated at the edge for typical MST parameters :

The streaming parameter at the center is : $\chi(0) = \dfrac{v_{Drift}(0)}{v_{Thermal}(0)} = \dfrac{\dfrac{J(0)}{n_e(0)\,e}}{\left(\dfrac{3k\,T_e(0)}{m_e}\right)^{1/2}}$

For $T_e(0) = 400$ eV , $n_e(0) = 1.e\,13\ cm^{-3}$, $v_{Drift}(0) = .4 \times 10^6$ m/sec $\chi(0)$ is about 2.75%.

The streaming parameter at r = α is : $\chi(a) = \chi(0) \times \dfrac{J(a)}{J(0)} \times \dfrac{n_e(0)}{n_e(a)} \times \dfrac{T_e^{1/2}(a)}{T_e^{1/2}(0)}$

From measured and estimated values of the profiles of J , n_e and T_e we obtain an edge streaming parameter of approximately 30 % . Looking back at figure 7.2 we see that a 30 % streaming parameter combined with a hot electron component of 450 eV and a cold component of 30 eV would produce an enhancement $I_{SXR}(0°) / I_{SXR}(180°)$ of 1.5 (contribution only from electron drift), while the measured ratio is greater than 30. This implies that the measured ratio $I_{SXR}(0°) / I_{SXR}(180°)$ is not due to an electron drift but is mainly due to the unidirectional flow of electrons along **B**,for which the ratio can be arbitrarily large.

Temperature of the hot electrons in MST

An interesting observation of the edge electrons is their very high temperature compared to the edge bulk electron temperature. The hot electron temperature evolution as measured by the SXR target probe is shown in figure 7.3 . We notice

that early in time (usually around 5 to 10 msec) there is a large increase in the measured temperature. We speculate that this is due to a runaway electron compo-

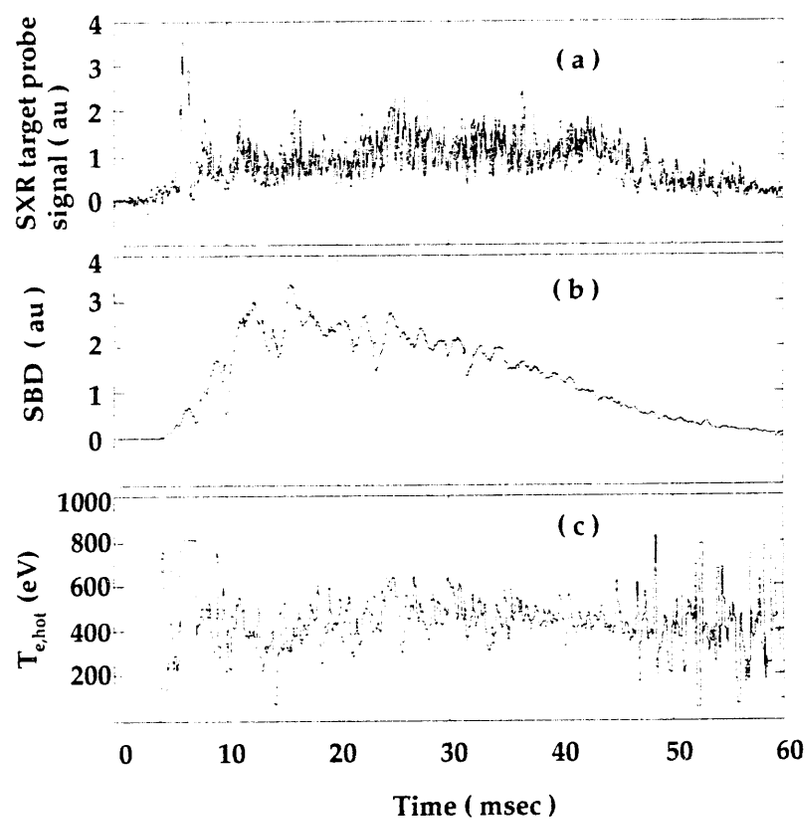

Figure 7.3. *a) A typical signal obtained with a SXR target probe. The level of fluctuations is very high. b) Plasma soft x-rays. c) The evolution of $T_{e,hot}$ shows a high edge electron temperature that appears to decrease during a sawtooth crash.*

nent since it only occurs for low density discharges. The oscillations of the SXR emissivity as observed with the SXR imaging system correlate fairly well with the evolution of $T_{e,hot}$. It appears that the hot electron temperature decreases during a sawtooth crash, indicating poor confinement during the MHD relaxation phase. This is supported by measurements of differently filtered SBD's " looking " at the bulk SXR signals which indicate a decrease in plasma temperature during the MHD relaxation phase. Poor confinement during the crash would also explain the large increase of hot electron current density and the flattening of the SXR emissivity profile measured.

The temperature of the hot electrons as measured with the target probe lies between 1 and 2 times the central electron temperature. This result is shown in figure 7.4. During the various plasma shots the plasma current was kept constant while the plasma density was varied by adjusting the amount of puffed hydrogen. The variation of the plasma density proved to have a significant effect on the ratio $T_{e,h} / T_e(0)$. This is demonstrated in figure 7.5. For densities above 1.1×10^{13} cm^{-3} the ratio becomes less than one, and if the ratio continued to fall off at the same rate we would expect the hot component to be negligible above $2.\times 10^{13}$ cm^{-3}. Most of the data points lie within a standard deviation of a linear least squares fit. The largest contribution to the scatter in the data is due to the uncertainty in the measured Thomson scattering temperature. We should mention here that the hot electron temperatures measured with an EEA are slightly lower than those measured with the SXR target probe and are approximately equal to the central electron temperature. A radial scan of the SXR target probe reveals that $T_{e,hot}$ is fairly constant to about 7 cm from the wall. Measurements beyond this point were extremely difficult due to the large incident power deposited on the probe.

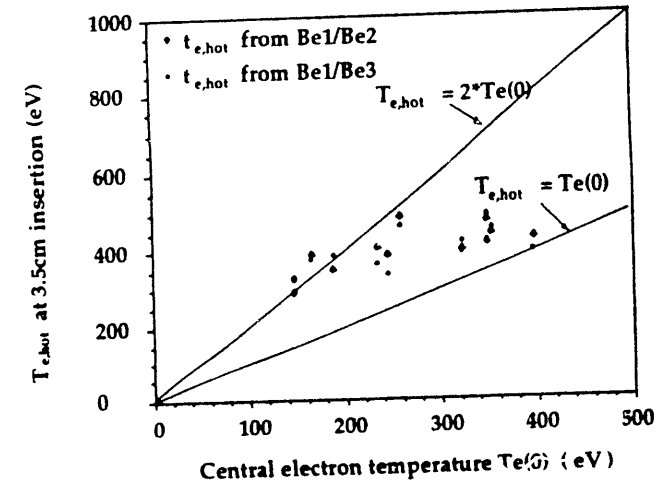

Figure 7.4. *The hot electron temperature ranges from 1 to 2 times the central electron temperature which was measured at 20 msec into the discharge. The fact that the two temperatures are of the same order suggests that the hot electrons are produced at the plasma center.*

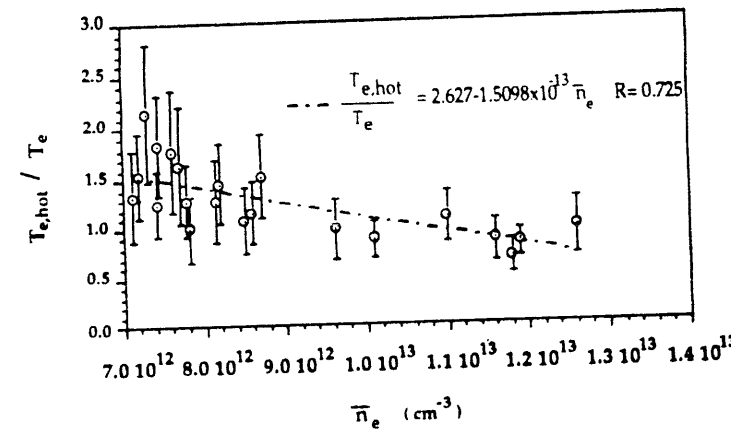

Figure 7.5. *The ratio of the hot electon component measured by the SXR target probe to the central Thomson Scattering temperature falls off with density.*

Density of the hot electrons

The density of the hot electrons is derived from eq. (4.7). The radial scan indicated an increase in density away from the wall ranging from .1 x 10^{11} cm^{-3} to 1. x 10^{11} cm^{-3} (figure 7.5) . The line-averaged density for these discharges was about 5. x 10^{12} cm^{-3} . Even though the hot electron density is only a few percent of the cold electron density the component of the radiated SXR power due to Bremsstrahlung is dominated by the hot electrons. This is seen in equation (3.10) where the free -free radiated power dependence on temperature is $e^{-h\nu / kT_{e,hot}}$.

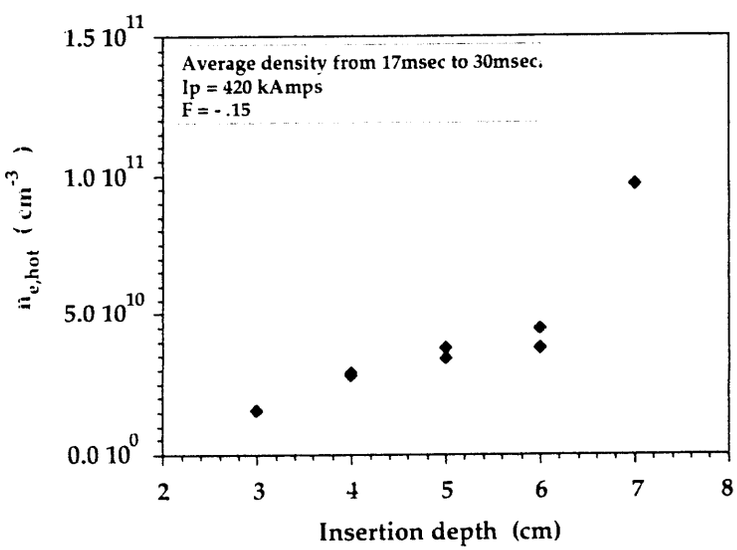

Figure 7.5. *A radial scan performed with the soft x-ray target probe reveals that the hot electron density increases from .1 x 10^{11} cm^{-3} to 1. x 10^{11} cm^{-3} for insertion depths ranging from 3 cm to 7 cm respectively. The reversal surface is located at around 7 cm.*

Power carried by the hot electrons

The power deposited on the target probe is calculated from equation (4.7) to be approximately 5 MWatts/m^2 . This power is much smaller than that measured on other RFP's. ZT-40M using a calorimeter probe measured the power to be 240 MWatts/m^2. We must mention that there is a significant error of a systematic

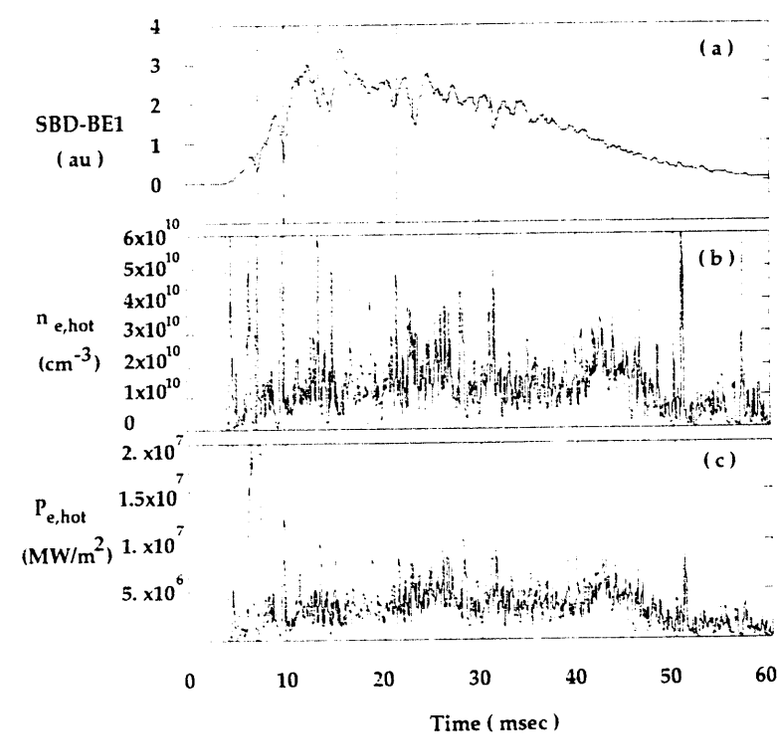

Figure 7.6. *a) The sudden drop in emissivity observed on the SBD's during a sawtooth crash coincides with a sudden rise in the density and power of the hot electrons (b), (c).*

nature in the measurement of the power deposited on the SXR target. The condition of the target surface may affect the spectrum of x-rays emitted from the target surfaces, and the exact target area that is hit by the fast electrons cannot be measured accurately. We do have however some indication of the active target area from examination of the carbon surface after it has been exposed to the hot electrons.

Current density of the hot electrons

The current density as measured with the target probe has a strong hot electron temperature dependence. This was seen in eq. (4.9). The current density appears to be greatly enhanced during the MHD relaxation phase as shown in figure 7.7 . A possible explanation for this event is the expected (from 3D MHD simulations) increased stochasticity of the magnetic field lines which results from the overlapping of neighbouring resistive MHD modes during a sawtooth crash.

7.2 Manifestations of the kinetic dynamo through soft x-ray measurements

During the current ramp-up phase of an RFP, large oscillations of the soft x-ray flux are measured. By correlating these SXR signals with the toroidal field at the wall one notices a sudden increase in $\mathbf{B_t}$ during the sawtooth crash as seen in chapter VI. This observed phenomenon is occasionally referred to as the "discrete" dynamo[9]. The measured hot electron temperature decreases during a crash while the density, power and current density show a sudden increase. During the rest of the discharge these large oscillations of the plasma energy away from the minimum Taylor state become rare while $\mathbf{B_t}$ at the wall remains reversed for a period much longer than expected from resistive diffusion alone. This implies that a "continuous"

dynamo mechanism must also be present, and it is very likely that it is also present during the current ramp-up phase of the discharge.

The contribution of the hot electrons to the dynamo effect has not yet been determined experimentally. Researchers from TPE - 1RM15 and STP - 3M claim that the existence of the hot electrons carrying a large fraction of the total ohmic input power supports the kinetic dynamo theory and in ZT - 40M the measured hot electron properties agree with those predicted by energetic electron transport modeling. From an experimental viewpoint these measurements do not prove that the hot electrons are responsible for the dynamo. The contribution of the fast electrons to the dynamo requires a measurement of $J_{e,hot}$,where $J_{e,hot}$ is the hot electron current density. Also the measurement of $J_{e,hot}$ must be made at different locations simultaneously since the generation of a *mean magnetic field* requires the spatial average $\langle J_{e,hot} \rangle$ be non-zero. From a theoretical viewpoint there are some doubts of the self consistency of the kinetic dynamo theory[10]. It is suggested that the hot electrons observed are test particles not resonant with any intrinsic normal modes ($v_{test} > \omega^* / k$).

Since the measurements performed with the SXR target probe have been local, we cannot make any direct estimates on the average magnetic field produced by the hot electrons. However the study of the correlations of the $J_{e,hot}$ signals with the toroidal field $\mathbf{B_t}$ at the wall and other measured quantities can provide some insight into the contribution of the hot electrons to the generation of reversed magnetic flux. We begin by comparing the evolution of $J_{e,hot}$ with $\mathbf{B_t}$ (a) in figure 7.7. We notice that the sudden current density increase during the crash phase coincides with the rapid increase of the toroidal field at the wall. This is also observed with the EEA which provides a more direct measurement of the hot electron density.

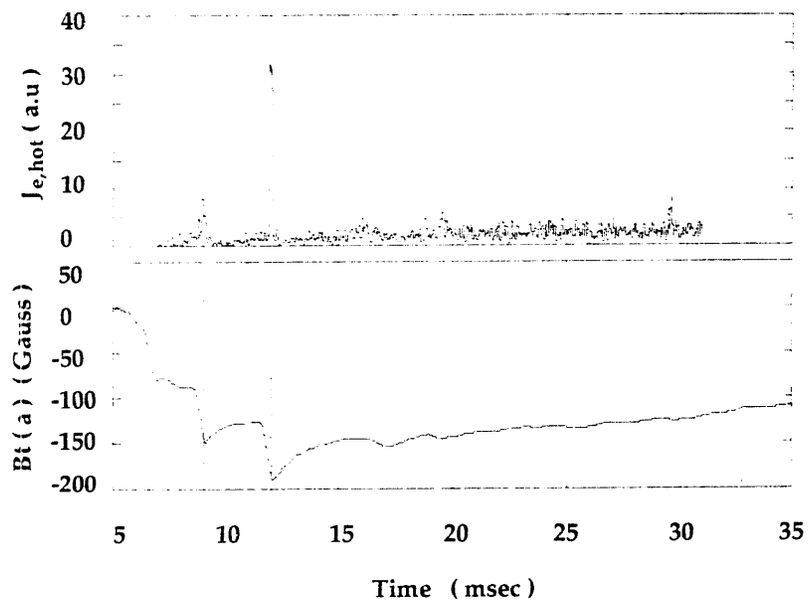

Figure 7.7. *The sudden generation of reversed toroidal magnetic field coincides with a sudden increase in the hot electron current density.*

At first one might speculate that this is evidence for the dynamo being driven by the hot electrons. However it is also possible that the hot electrons are the result of enhanced transport due to the large stochastisity produced by the overlapping of the various m = 1 n= -5,- 6,- 7... tearing modes during the MHD relaxation phase.

An interesting feature observed in most of the volume SXR signals is a sudden (of the order of a tenth of a millisecond) enhancement during a sawtooth crash. This phenomenon is usually seen at low density plasmas (fig. 7.8). This "spike" is possibly caused by the rapid ionization of impurities by the hot electrons during the crash. Energetic electrons striking the wall (aluminum and graphite)

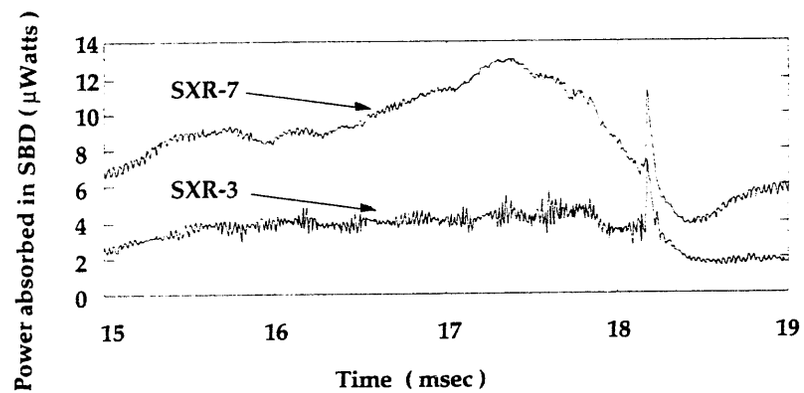

Figure 7.8. *For low density discharges a large and sudden enhancement of the sxr signals occurs during the sawtooth crash. This "spike" is perhaps due to the rapid ionization of impurities by the hot electrons.*

produce target x-rays with a spectrum containing the .277 keV K_α carbon and the 1.49 keV K_α aluminum line superimposed on a continuous spectrum. From SXR target probe data we know that the ratio of SXR-Be1 (7.62 μm Be filter) and SXR-Be2 (15.24 μm Be filter) for a typical 500 kamp discharge lies around 1.5 for a carbon target and slightly lower for a tungsten target. On the other hand the ratio of SXR-Be1 and SXR-Be2 for bulk plasma x-rays during the "spike", lies between 5 and 10 as would be consistent with a SXR spectrum dominated by an OVII K line. The duration of the spike is estimated from known electron impact ionization cross sections. For a 400 eV hot electron component of density $1.x\ 10^{12}\ cm^{13}$ we obtain an ionization time of $\tau \approx .1$ msec which is in agreement with the observed duration of the spike.

Finally in figure 7.9 I show the reversed magnetic field at the wall vs the hot electron current density. The above quantities are averaged over a segment of the discharge which does not include any flux jumps. The reversed magnetic field produced by the dynamo does not vary appreciably while the hot electron current density varied by a factor of 4. This result implies that the hot electron contribution to the *continuous* dynamo is small.

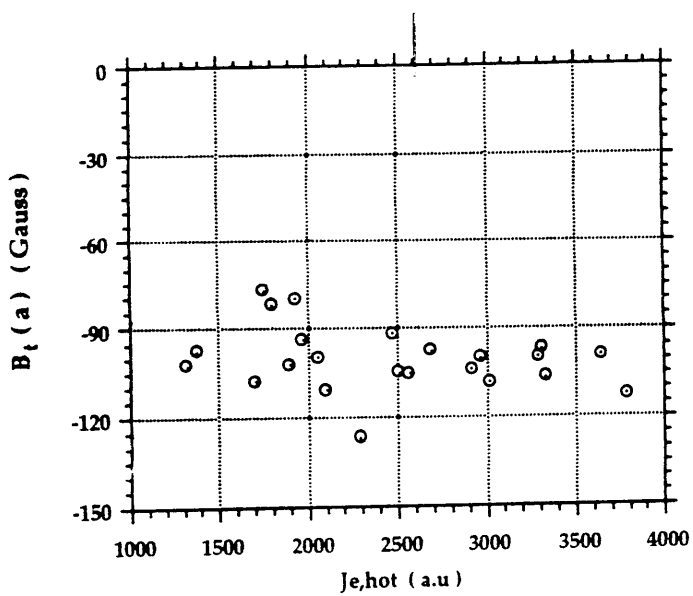

Figure 7.9. *The reversed toroidal magnetic field at the wall is ploted vs the hot electron current density during a density scan. Both quantities are averaged between 15 msec to 20 msec into the discharge.*

7.3 Measuring fluctuations of the hot electron properties with a soft x-ray target probe.

We will first examine the feasibility of the target probe being used as a fluctuation diagnostic. This will require an estimate of the frequency response of the system's components. The relevant features of the system that contribute to its frequency response are the carbon target, the SBD's and the amplification stage.

Target response

An electron striking the carbon target will produce x-rays over a period Δt which is approximately the time it takes for the electron to lose most of its energy and subsequently become captured by some atom. For hot electron energies in the keV range the main loss of energy is due to collisions. As an example an electron with kinetic energy 10 keV interacting with a carbon target has a stopping power due to collisions of 20.14 MeV-cm^2/gm, a stopping power due to radiation of .34x10^{-2} MeV-cm^2/gm and a range of .26X10^{-3} cm. The time Δt turns out to be negligible. One may ask about the transition time for the excited K_α carbon line at 277 eV, however it turns out that since the filter response is about 7.2x10^{-15} at 277 eV these photons will not be detected.

SBD response

The SBD's have a time response of a few nanoseconds which can be varied by adjusting their bias voltage.

Linear amplifiers

We conclude that the response of the system is determined mostly by the amplifiers. The amplifiers used in the experiments have a measured roll-off close to 200 kHz.

Having convinced ourselves that the SXR target probe has a frequency response basically determined by the amplification stage we proceed in presenting initial results from fluctuations in the hot electron properties.

The measured power in the fluctuations (see fig. 7.10) of the SXR target signal are large compared to the power in the mean signal. The fluctuation level in the

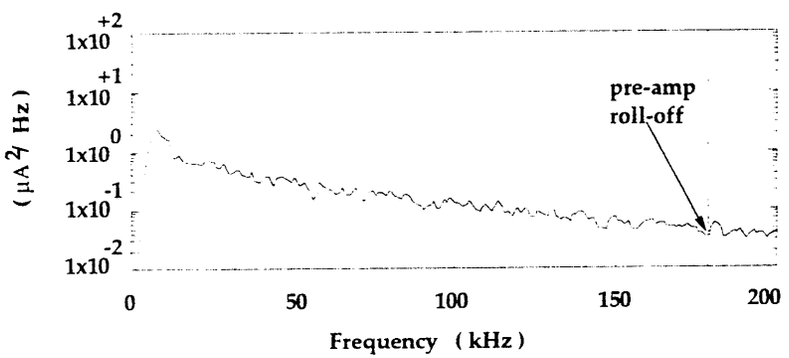

Figure 7.10. *The spectrum* $\langle FFT(\tilde{I}_{SXR}) FFT^*(\tilde{I}_{SXR})\rangle$ *of the SXR target signal.*

derived hot electron temperatures is less than that of the SXR target signals but large compared to the fluctuation level observed in the bulk plasma SXR signals. We assume that the temperature is the sum of a mean component and a fluctuating part.

$$T_{ehot} = \langle T_{ehot} \rangle + \tilde{T}_{ehot}$$

The measured spectra are representative of an ensemble of shots that have similar plasma parameters. For each shot, a time window was chosen from 17 msec to 25.192 msec in which the fluctuation analysis was performed. Each time window contains

4096 data points. The fast Fourier transform of the fluctuating quantities were calculated over subwindows containing 512 points.

For the calculation of the spectrum of the fluctuating hot electron temperature $\tilde{T}_{e,hot}$, we used the following expression :

$$\tilde{T}_{e}hot = \sqrt{\frac{\sum_{freq}\left[\sum_{i=1}^{N_1} \frac{FFT(T_e hot)\, FFT^*(T_e hot)}{N_1}\right]}{256}}$$

where , N_1 is the total number of subwindows. The ratio $\frac{\tilde{T}_{ehot}}{\langle T_{ehot}\rangle}$ is measured to be approximately 60 % which is high compared to the ratio that corresponds to the thermal component of about 30 %. This implies that the hot electrons may play a significant role in magnetic- fluctuation - induced energy transport in RFP's.

References for chapter 7

1. A. R. Jacobson and R. W. Moses, Physics Rev. Lett. 52, 2041 (1984).

2. R. W. Moses, K. F. Schoenberg and D. A. Baker, Phys. Fluids 31, 3152.

3. J. C. Ingraham, R. F. Ellis, J. N. Downing, C. P. Munson, P. G. Weber and G. A. Wurden *" Energetic electron measurements in the edge of a reversed-field pinch. "* Phys. Fluids B 2 (1), January 1990.

4. R. F. Ellis, J. C. Ingraham, P. G. Noonan and H.Y.W. Tsui, Bull Am, Phys. Soc. 33 1999 (1988)

5. Shoichi Shina, Katunori Saito, Hideki Arimoto, Akio Matsuoka, Squichi Yamada, Saduo Masamune, Akiyoshi Nagata and Koichi Sato. *" The measurement of Soft X-Rays from the STP-3 (M) Reversed-Field Pinch Plasma."* Journal of the Physical Society of Japan, Vol. 56, No. 4, April, 1987, pp. 1282-1285.

6. "Soft x-ray measurements in TPE - 1RM15 reversed field pinch". Presented at the US./Japan RFP workshop, March 12 - 15 1990, Madison, USA.

7. G. A. Wurden et al. *" RFP experiments : Results from ZT - 40M and ZT - P "*. Presented by G. A. Wurden at the Proc. Int. School of Plasma Physics and Physics of Mirrors, RFP's and Compact Tori. (Varenna) Vol I (1987).

8. K. F. Schoenberg and R. W. Moses, *"Magnetic turbulent electron transport in the reversed-field pinch"* Phys. Fluids B 3 (6), June 1991.

Chapter 8

Conclusions and Discussion of the Experimental Results.

The experiments presented in this thesis were motivated by the necessity to obtain a better understanding of the RFP dynamo. A SXR imaging system and a SXR target probe were the main diagnostics employed in measurements of the contributions to the RFP dynamo that can arise from kinetic and MHD mechanisms. Many previously obtained results on other RFP devices were reproduced on MST. However, in some instances the experimental data obtained on MST would differ from previous results indicating the importance of the intricate characteristics of each machine in influencing many of the observed RFP phenomena. In this chapter I will summarize the results of the experiments and discuss how they compare with experimental results made on other RFP devices and 3D simulations of the MHD equations.

1. The dominant *internal* unstable modes present in the MST were measured to have toroidal mode numbers in the range -5,-6,-7. These modes phase lock to each other producing a "slinky mode"and rotate in the ion diamagnetic drift direction with velocities ranging from $1.x10^6$ cm/sec to $6.x10^6$ cm/sec. The modulation of the precursor amplitude was measured with the SXR imaging system. and was found largest at a radius of .5a, which is the predicted location of the n=6 resonant surface,while simultaneous measurements of the toroidal n number of these precursors gave a toroidal n of -6.

2. 3D MHD codes (that include the nonlinear interaction between modes)[1] also predict the generation of regions of stochastic magnetic field lines throughout most of the plasma due to the overlap of neighboring islands. This is not generally observed on MST since SXR emissivity reconstructions clearly show the existence of good flux surfaces extending up to the geometric axis. We should mention however that during the sawtooth crash there is some indication of emissivity surfaces being distorted probably due to the overlapping of the m=1 islands.

3. Experiments in the thin resistive OHTE[2] device had suggested that a rotating slinky mode could play an important role in the reversed field generation process. Phase locking of the m=1 modes has been identified on MST. However the properties of the slinky in MST differ from those in OHTE. In MST the slinky is always present and does not appear to contribute to the dynamo process. The reversed field is produced at different rates during the discharge while the amplitude of the slinky does not correlate with the reversed magnetic flux generation. Also it was observed in OHTE that the m=1 resistive mode amplitudes would disappear when the slinky was present due to the mixing of the modes. This phenomenon is not seen in MST discharges.

4. The exact cause of the occasional locking of the plasma to the wall is still unknown. When the locking occurs the m=1 modes cease to rotate as measured with magnetic pick up coils and toroidally separated SBD's. SXR emission mode analysis shows a decrease in the m=1 Fourier Bessel component of the emissivity during the transition from a rotating to a locked plasma.This is due to the flattening of the emissivity profile as seen in the SXR reconstructions. This might also explain why

locked discharges reside closer to the BFM F-θ curve. A flattening of the emissivity profile also occurs during the MHD relaxation phase which on an F-θ diagram corresponds to the plasma state (determined by F and θ) approaching the BFM curve of minimum magnetic energy.

5. In ZT-40M[3] a *localized* structure of m=1 and high n components was observed to rotate around the torus , disperse and eventually reconnect on itself leading to the generation of reversed toroidal flux. Such a localized rotating structure is not present during locked shots in MST even though the dynamo process continues to be present for these shots.

6. Two distinct rates of generation of reversed magnetic field are observed. A slow increase of $B_t(a)$ during the diffusion phase is followed by a sudden generation of reversed magnetic field (also referred to as the discrete dynamo)[4] during the sawtooth crash. Experimental scaling of the diffusion and MHD relaxation time with the magnetic Reynolds number S_{OHMIC} gave :

$$\frac{\tau_{Dif}}{\tau_A} \approx S_{Ohmic}^{0.9 \pm 0.1}$$

$$\frac{\tau_{MHD}}{\tau_A} \approx S_{Ohmic}^{0.76 \pm 0.11}$$

Although not a direct proof of the m=1 driven dynamo model, the SXR emissivity reconstructions do show large distortions during the crash near the expected resonant surface of the m=1, n=-6 tearing mode. Early 1D, 1 helicity simulations[5] introduced a reconnection model consisting of two phases , namely the first

reconnection, where τ_1, scaled as $S_{Spitzer}^{1/2}$ and the second reconnection, where τ_2, scaled as $S_{Spitzer}$. This model predicted that during the first reconnection reversed magnetic flux is generated but that the process would be followed with a peaking of the plasma current. This mode does not appear to be applicable during the MHD relaxation phase since the observed flattening of the emissivity profiles occur during the sudden generation of reversed magnetic flux in the MHD relaxation phase. However, it is possible that this quasilinear model in which resistivity is important may be applicable to the diffusion phase where the m=1 modes have not grown large enough to interact nonlinearly.

7. Many existing 3D MHD simulations use a magnetic Reynolds number derived from the Spitzer resistivity (anomalous contribution is not included). In order to compare the experimental results with the numerical results, measurements of τ_{MHD} versus $S_{Spitzer}$ were also made. Though the errors in the measurements were larger due to the difficulty of measuring T_e accurately during the sawtooth crash, the results do imply that the MHD relaxation time does not have a strong dependence on the Spitzer resistivity whereas the diffusion time does depend on the classical resistivity. The experimental scaling :

$$\frac{\tau_{Dif}}{\tau_A} \approx S_{Spitzer}^{0.44 \pm .09}$$

$$\frac{\tau_{MHD}}{\tau_A} \approx S_{Spitzer}^{0.0 \pm 0.2}$$

suggests a quasilinear dynamo mechanism operating during the diffusion phase

similar to the one described by Nebel et al. [5], and a nonlinear mechanism during the MHD relaxation phase as presented by Holmes et al[6]. A unifying model that includes both the quasilinear and nonlinear dynamo mechanisms has been introduced by Ho and Craddock.[7]

8. With the employment of a SXR target probe the ratio $\frac{T_{e,hot}}{T_e(0)}$ was measured to be a function of the plasma density and range between 2 for $n_e = 5.x10^{12} cm^{-3}$ and 0.8 at $n_e = 1.2.x10^{13} cm^{-3}$ (see figure 7.5). With no hot electrons present one would expect the ratio of the central Thomson scattering temperature to the edge "cold" electron temperature to be approximately 10. One of the difficulties encountered with the SXR target probe, was the limited range of density over which the diagnostic had an acceptable signal-to-noise ratio. A future improvement of the system (thinner filters, shorter target to detector distance) would show if the measured relation between $\frac{T_{e,hot}}{T_e(0)}$ and n_e still holds at higher plasma densities.

9. An initial feasibility investigation of using the SXR target probe for studying fluctuations showed that the system's time response is basically limited by the preamp frequency roll-off point. The ratio $\frac{\tilde{T}_{e,h}}{\langle T_{e,hot} \rangle}$ was measured to be approximately 60 % , much larger that the corresponding 30 % measured for the cold component. This result implies that the fast electrons may contribute considerably to the magnetic fluctuation induced transport in RFP's and should be included in transport modeling of RFP's.

10. The properties of the hot electrons can be varied considerably with

density. Variations of the hot electron density by a factor of 4 had little effect on the amplitude of the reversed magnetic field at the wall. This result suggests that a dynamo process can exist in an RFP without the presence of fast electrons.

The diversity of results reported in recent experiments in RFP's regarding mechanisms that drive the RFP dynamo is probably due to specific machine features and suggests that the planned perturbation experiments in MST could lead to some interesting results. The development of a pellet injector, a vertical field , a feedback stabilization scheme and DC helicity injection will provide a new set of accessible plasma states. The effectiveness of the vertical field in centering the plasma will easily be determined from SXR emissivity reconstructions. The stabilization of resistive modes through feedback control can also be studied through SXR emissivity mode analysis. The response of the hot electrons to these perturbations can also be measured with the SXR target probe. In the opening chapter I mentioned that the role of microturbulence in the RFP dynamo could not be investigated since a diagnostic with very high spatial resolution is required. Recently developed diagnostics such as XUV monochrometers[8] using mirrors with layers of synthetic microstructure coatings and far-infrared interferometers[9] will hopefully be included in the next generation of diagnostics employed in RFP's to study fluctuations with high imaging resolution.

References for chapter 8.

1. D. D. Schnack, E. J. Caramana and D. A. Nebel, *"Three dimensional magnetohydrodynamic studies of the reversed field pinch."* Phys. Fluids **28** (1), January (1985).

2. R. J. La Haye, P. S. Lee, M. J. Schaffer, T. Tamano, P. L. Taylor (General Atomics, San Diego, California, USA), *"Magnetic Fluctuation Measurements in the Resistive Shell OHTE Device Operated as a Reversed Field Pinch."* Nuclear Fusion, Vol. 28, No. 5 (1988).

3. R. B. Howell, J. C. Ingraham, G. A. Wurden, P. G. Weber, and C. J. Bachenauer, *" Asymmetric flux generation, m=1 activity, and edge phenomena on a reversed-field pinch"*, Phys. Fluids **30** (6), June (1987).

4. S. Hokin, A. Alamagri, S. Assadi, J. Beckstead, G. Chartas, N. Crocker, M. Cudzinovic, D. Den Hartog, R. Dexter, D. Holly, S. Prager, T. Rempel, J. Sarff, E. Scime, W. Shen, C. Spragins, C. Sprott, G. Starr, M. Stoneking, C. Watts, R. Nebel, " Global Confinement and Discrete Dynamo Activity in the MST Reversed Field Pinch " , Phys. Fluids B 3 (8), August (1991).

5. E. J. Caramana, R. A. Nebel, and D. D. Schnack, Phys. Fluids **26**, 1305 (1983).

6. J. A. Holmes, B. A. Carreras, T. C. Hender, H. R. Hicks, V. E. Lynch, Z. G. An, and P. H. Diamond. *" Nonlinear interactions of tearing modes : A comparison between the tokamak and the reversed field pinch configurations"* , Phys. Fluids **28** (1), January (1985).

7. Y. L. Ho and G. G. Craddock. *" Nonlinear Dynamics of Field Maintenance and Quasi-Periodic Relaxation in Reversed-Field Pinches."* Presented at the US/Japan Workshop on Fluctuations in RFP and ULQ Plasmas, March 12-15,1990 Madison, Wisconsin.

8. L. K. Huang, M. Finkenthal, S. Regan and H. W. Moos, *"Development of an XUV spectroscopic diagnostic for the electron density and temperature fluctations in tokamak*

plasma center." Presented at the APS meeting of the Division of Plasma Physics, Cincinnati, (1991).

9. G. A. Hallock, M. L. Gartman, K. Chiang, S. Shin, R. L. Castles, A. S. Rahman, " *The TEXT Upgrade Far-Infrared Interferometer System.*" Presented at the APS meeting of the Division of Plasma Physics, Cincinnati, (1991).

Appendix I

In order to maximize the configuration entropy under the constraint equations(3.20 ,3.22 ,3.23) we set dQ = 0 :

$$dQ = 0 \Rightarrow \left\{ \begin{array}{l} \sum_{c=1}^{nc} \left[\frac{\partial Q}{\partial E_c} dE_c + \frac{\partial \Phi_0}{\partial E_c} dE_c + \ldots + \frac{\partial \Phi_{nd+1}}{\partial E_c} dE_c \right] = 0 \\ \sum_{d=1}^{nd} \left[\frac{\partial Q}{\partial N_d} dN_d + \frac{\partial \Phi_0}{\partial N_d} dN_d + \ldots + \frac{\partial \Phi_{nd+1}}{\partial N_d} dN_d \right] = 0 \end{array} \right\}$$

Using Lagrange Multipliers we have:

$$\left\{ \begin{array}{ll} \left[\frac{\partial Q}{\partial E_c} + \lambda_0 \frac{\partial \Phi_0}{\partial E_c} + \ldots - \lambda^2_{nd+1} \frac{\partial \Phi_{nd+1}}{\partial E_c} \right] = 0 & nc \ equations \\ \left[\frac{\partial Q}{\partial N_d} + \lambda_0 \frac{\partial \Phi_0}{\partial N_d} + \ldots - \lambda^2_{nd+1} \frac{\partial \Phi_{nd+1}}{\partial N_d} \right] = 0 & nd \ equations \end{array} \right\}$$

Substituting the expressions for the constraints $\Phi_i = 0$, equation (3.18) and performing the differentiations we obtain:

$$E_c = \exp\left(-1 + \lambda_0 + \sum_{d=1}^{nd} \lambda_d W_{dc} \right)$$

$$N_d = \exp\left[-1 + \lambda_d \overline{S} - \frac{2 \overline{S} \lambda^2_{nd+1}}{nd \ \sigma^2_d \ \overline{\sigma}_d} (N_d - D_d) \right]$$

EXTERNAL DISTRIBUTION IN ADDITION TO UC-20

S.N. Rasband, Brigham Young University
J.B. Taylor, Institute for Fusion Studies, The University of Texas at Austin
M.A. Abdou, University of California, Los Angeles
R.W. Conn, University of California, Los Angeles
T. Dolan, INEL
R. Smith, University of Iowa
F.W. Perkins, PPPL
O. Ishihara, Texas Technical University
P.E. Vandenplas, Association Euratom-Etat Belge, Belgium
Centro Brasileiro de Pesquisas Firicas, Brazil
P. Sakanaka, Institute de Fisica-Unicamp, Brazil
Mme. Monique Bex, GANIL, France
J. Radet, CEN/CADARACHE, France
University of Ioannina , Greece
S. Ortolani, Istituto Gas Ionizzati, EURATON-ENEA-CNR Association, Italy
R. Andreani, Associazione EURATOM-ENEA sulla Fusione, Italy
Y. Kondoh, Gunma University, Kiryu, Gunma, Japan
FOM-Instituut voor Plasmafysica "Rijnhuizen", The Netherlands
Z. Ning, Academia Sinica, People's Republic of China
P. Yang, Shandong University, People's Republic of China
S. Zhu, University of Science & Technology of China, People's Republic of China
I.N. Bogatu, Institute of Atomic Physics, Romania
M.J. Alport, University of Natal, Durban, South Africa
R. Storer, The Flinders University of South Australia, South Australia
B. Lehnert, Royal Institute of Technology, Sweden
Librarian, CRPP, Ecole Polytechnique Federale de Lausanne, Switzerland
B. Alper, Culham Laboratory, UK
A. Newton, Culham Laboratory, UK

6 for Chicago Operations Office
4 for individuals in Washington Offices

INTERNAL DISTRIBUTION IN ADDITION TO UC-20
80 for local group and file

END

DATE FILMED

10 / 30 / 91